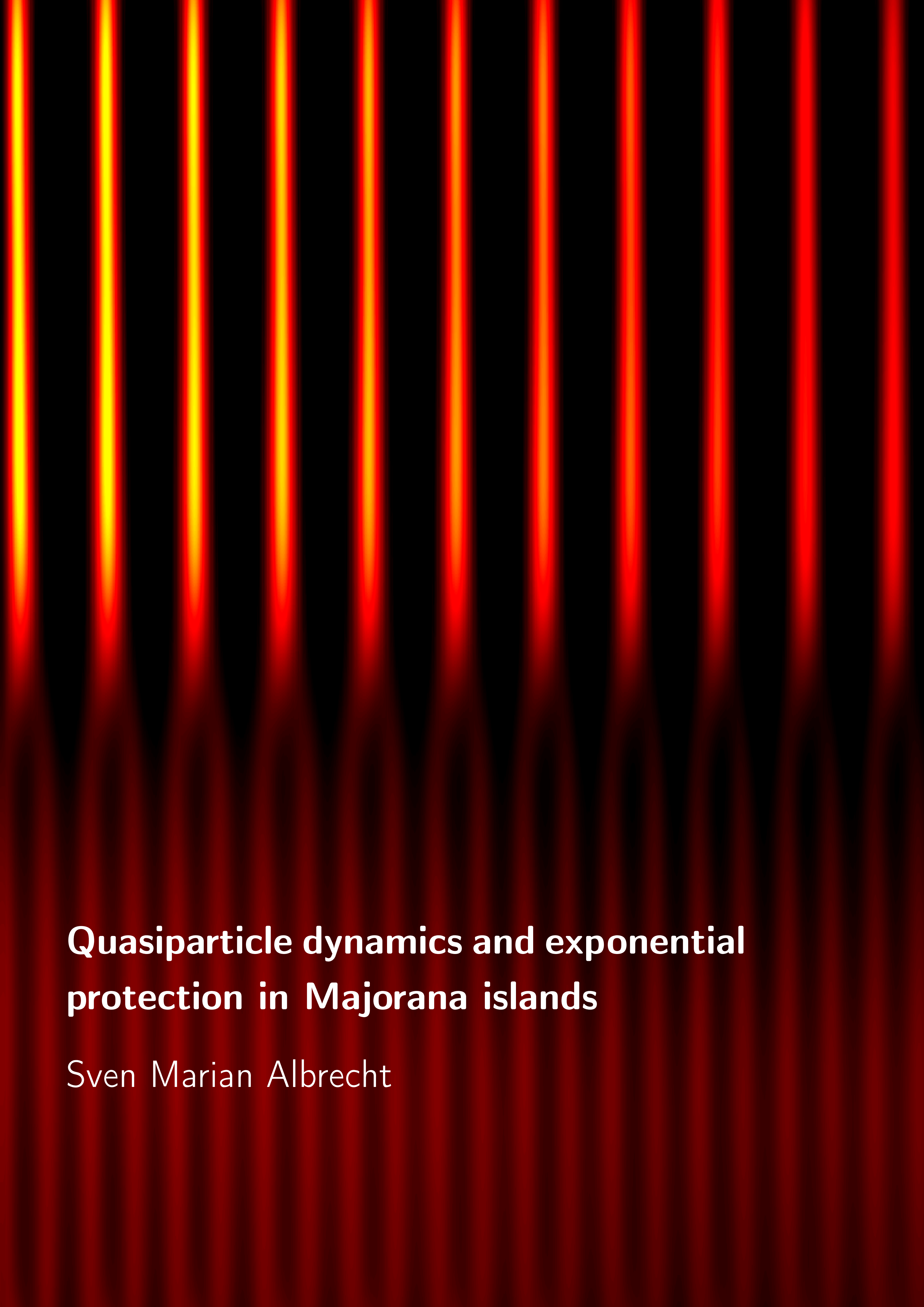

# Quasiparticle dynamics and exponential protection in Majorana islands

Sven Marian Albrecht

# QUASIPARTICLE DYNAMICS AND EXPONENTIAL PROTECTION IN MAJORANA ISLANDS

SVEN MARIAN ALBRECHT

Ph.D. Thesis
Center for Quantum Devices
Station Q Copenhagen
Niels Bohr Institute
University of Copenhagen

Academic advisor:
Prof. Charles Marcus

Assessment committee:
Prof. Leo Kouwenhoven
Prof. Felix von Oppen

*October 2016*

Cover:
Hybridized Majorana modes oscillate in a magnetic field.
Albrecht et al., *Nature* **531**, 206-209 (2016)

# ABSTRACT

This thesis presents measurements on Majorana islands: semiconductor-superconductor hybrid nanowire quantum dots in the trivial and the topological superconducting phase.

We fabricate Majorana island devices based on indium arsenide nanowires with an epitaxially matched aluminum half-shell. Measuring quasiparticle transport, we observe a gate voltage dependent even-odd Coulomb blockade pattern, associated with quasiparticle occupation of bound states, for which we demonstrate state parity lifetimes exceeding 10 milliseconds.

Using Coulomb-blockade spectroscopy and varying the magnetic field, we measure oscillating energy splittings of near-zero energy states, consistent with theoretical predictions for hybridized Majorana modes. We present a length study of Majorana islands and demonstrate the exponential suppression of energy splitting with increasing island length, as expected for Majorana modes, with a characteristic length of 260 nm. For long devices exceeding one micron, transport at high magnetic fields shows discrete zero-energy states, with an energy gap to a higher-energy continuum, and evenly spaced Coulomb-blockade conductance peaks, a signature of teleportation via Majorana modes. A preliminary analysis shows that Coulomb peaks also feature an alternating magnetic field dependent skew, the subject of future work.

We additionally observe novel transport signatures of quasiparticle poisoning in a Majorana island strongly coupled to normal metal leads. Numerical simulations show good agreement with measurements and allow us to extract a time for poisoning of the island's ground state from the leads of 3 microseconds.

# ACKNOWLEDGEMENTS

First, I would like to thank my advisor, Prof. Charles Marcus, for allowing me to do research in his lab, for providing me with a stimulating scientific environment, for teaching me what's important in science, and for pushing me to my limit and occasionally past that. Charlie sets out to take on the most ambitious experiments at the forefront of science and quantum engineering. He hires the smartest people, and allows them to focus on their research by providing them with the best equipment that money can buy, a great administrative team, and an extremely well run lab. Working at the pace of his group was new to me in the beginning, but I adapted to it quickly.

I also want to extend my gratitude to Prof. Leo Kouwenhoven, Prof. Felix von Oppen, and Prof. Jens Paaske, for taking time out of their very busy schedules and agreeing to be on my thesis assessment committee.

Next, I want to acknowledge the people in the lab that accompanied me during this project, many of which have become my close personal friends. Henri Suominen, who started with me and whose nicknames are too many to name at this point, was an understanding fellow traveler during the ups and downs of a PhD. I have greatly appreciated his stoic temperament, and his refusal to conform to a normal human sleep pattern. I am indebted to Willy Chang, now pursuing more worldly things in Singapore, for teaching me the basics of fabrication and lab life, and for taking me under his wing for the first half year of my PhD. Likewise, Andrew Higginbotham, my main collaborator and one of the sharpest minds of his generation, has been a source of inspiration and of raw physics knowledge to me. I would like to thank Morten Kjærgaard for always being there to talk, for pushing me in the right direction scientifically and personally, and for having a strong sense of right and wrong. Morten has tattoos, a motorcycle, and a wife, which gave him the air of a cool older lab-brother. I will miss Guen Prawiroatmodjo, and our many interesting discussions, but I already look forward to agreeing to disagree when I visit her in San Francisco. I have many good memories from the road trip through Texas with Thorvald Larsen, one of QDev's nicest and most relaxed members. I would also like to stay in touch with Fabrizio Nichele, who provided me with Italian wisdom and who became a close confidant during the time we worked together. Thomas Sand Jespersen has provided valuable guidance to my project, as well as food for thought in discussions about physics and life. The exponential protection paper wouldn't have been possible without him. Likewise, I owe a lot to Ferdinand Kuemmeth for his brain teasers, for teaching me how to be a low temperature physicist, and for insisting that I document properly. Karsten Flensberg and Jeroen Danon were always available to answer my questions about theory and have been great collaborators. Likewise, Martin Leijnse has been helpful in explaining the theoretical details of Majorana physics to me. I want to thank Shivendra Upadhyay for his guidance with fab and lab life during the beginning of my PhD. Peter Krogstrup, genius grower, has shown me that it's possible to be on top of your game in science and in the world outside of it. I want to thank Morten Madsen, Esben Bork Hansen, Davydas Razmadze, Charlotte Bøttcher, Deividas Sabonis, Mingtang Deng, Jeremy Yodh, Gediminas Kiršanskas, Jesper Nygård, and Jukka Pekola for the good collaboration, and Lucas Casparis and Karl Petersson for their good advice. I also appreciate the efforts of the administrative team, in particular those of Jess Martin, Katrin Hjorth, and Tina Nielsen.

I am grateful to my friends for being with me during the last three years and accepting my sometimes erratic work schedule. From the Copenhagen side, I want to mention Lucian Onea and Piotr Andrzej Żywień, who had my back when things fell apart and cheered with me when they came together. I appreciate the encouragement of Victor Yakimov, Marcho Markov, Traian Popa, Peter Forsberg, Serban Ghiuta, Raphaël Daveau, Miguel Carro Temboury, Ana Cristina Fernandes, Lena Ztuts, Christine Ritter, and Viktorija Daugvilaite. I am very grateful for the emotional support of Michelle Buckley and Andrea Dahlén, as well as for the motivation so kindly provided by Julia Vehar. I am extremely happy that Patrick Pinske, Jasmin Esser, and Jens Buchmann have stayed so close to me during times together and apart. The same is true for Christian Brennecke, with whom I can still share both my deepest and most shallow thoughts.

Lastly, I would not be handing in this PhD thesis without the good advice of my uncle Herbert Albrecht and the endless support of my family. As I grew older, I began to notice how a person's life is largely influenced by the values that they grew up with. In this regard, I want to thank my parents Imma Albrecht and Ulrich Albrecht for instilling me with an international mindset, and for laying the foundation from which I have pursued my interests.

# CONTENTS

1 INTRODUCTION 1

I THEORY AND FABRICATION 5

2 MAJORANA MODES 7
- 2.1 Historical background . . . 7
- 2.2 Mathematical description . . . 8
- 2.3 The Kitaev chain . . . 9
- 2.4 Nanowire in proximity to a superconductor . . . 11
- 2.5 Mode hybridization for finite systems . . . 14
- 2.6 State-continuum anti-crossing . . . 15
- 2.7 Wave function at the topological phase transition . . . 17
- 2.8 Conclusion . . . 19

3 QUANTUM DOTS AND TUNNELING SPECTROSCOPY 21
- 3.1 Transport through quantum dots . . . 21
- 3.2 Bias spectroscopy of N-S interfaces . . . 23
- 3.3 Density of states of a Majorana island . . . 25
- 3.4 Coulomb-blockade spectroscopy of Majorana islands . 28
- 3.5 Bias spectroscopy in Majorana islands . . . 32
- 3.6 Discussion . . . 32
- 3.7 Conclusion . . . 35

4 DEVICE FABRICATION 37
- 4.1 Chip blanks . . . 37
- 4.2 Nanowire growth . . . 39
- 4.3 Nanowire deposition . . . 39
- 4.4 Making Majorana islands . . . 44

II QUASIPARTICLE DYNAMICS I 51

5 PARITY LIFETIME OF BOUND STATES IN A PROXIMITIZED SEMICONDUCTOR NANOWIRE 53
- 5.1 Introduction . . . 54
- 5.2 Device geometry . . . 54
- 5.3 Parity effect . . . 55
- 5.4 Model . . . 56
- 5.5 Conclusion . . . 61
- 5.6 Methods . . . 62

III EXPONENTIAL PROTECTION 65
6 EXPONENTIAL PROTECTION OF ZERO MODES IN MAJORANA ISLANDS 67
6.1 Introduction . . . . . . . . . . . . . . . . . . . . . . . . 68
6.2 The Majorana island . . . . . . . . . . . . . . . . . . . . 68
6.3 Exponential protection . . . . . . . . . . . . . . . . . . . 72
6.4 Excitation spectrum and bias spectroscopy . . . . . . . 73
6.5 Signatures of electron teleportation . . . . . . . . . . . . 75
6.6 Conclusion . . . . . . . . . . . . . . . . . . . . . . . . . 76
6.7 Extended data . . . . . . . . . . . . . . . . . . . . . . . . 77
IV QUASIPARTICLE DYNAMICS II 91
7 TRANSPORT SIGNATURES OF QUASIPARTICLE POISONING IN A MAJORANA ISLAND 93
7.1 Abstract . . . . . . . . . . . . . . . . . . . . . . . . . . 94
7.2 Introduction . . . . . . . . . . . . . . . . . . . . . . . . 94
7.3 Energetics and transport . . . . . . . . . . . . . . . . . . 96
7.4 Measurements . . . . . . . . . . . . . . . . . . . . . . . . 98
7.5 Magnetic field dependence . . . . . . . . . . . . . . . . 100
7.6 Conclusion . . . . . . . . . . . . . . . . . . . . . . . . . 104
V PEAK SKEWS 105
8 ANALYSIS OF PEAK SKEWS IN A MAJORANA ISLAND 107
8.1 Definition . . . . . . . . . . . . . . . . . . . . . . . . . 107
8.2 Magnetic field dependence . . . . . . . . . . . . . . . . 108
8.3 Conclusion . . . . . . . . . . . . . . . . . . . . . . . . . 114
BIBLIOGRAPHY 116

# LIST OF FIGURES

Figure 2.1 Trivial and topological pairing in the Kitaev chain. 10
Figure 2.2 Nanowire in proximity to a superconductor. 11
Figure 2.3 Nanowire band structure. 13
Figure 2.4 Majorana mode hybridization. 16
Figure 2.5 Ground state wave functions. 18
Figure 3.1 Shell filling in a carbon nanotube. 23
Figure 3.2 Majorana island device. 25
Figure 3.3 Superconducting proximity effect. 26
Figure 3.4 Density of states. 28
Figure 3.5 Energy of a Majorana island. 29
Figure 3.6 Transport regimes of a Majorana island. 31
Figure 3.7 Gate voltage and induced charge. 33
Figure 3.8 Common mode peak motion. 34
Figure 3.9 Negative state energies. 35
Figure 4.1 Chip blanks and bonded sample. 38
Figure 4.2 Epitaxial interface between Al and InAs. 39
Figure 4.3 Nanowire forest on a growth substrate. 40
Figure 4.4 Wet and dry deposition. 40
Figure 4.5 CAD design of a Majorana island. 46
Figure 5.1 Nanowire-based hybrid quantum dot. 55
Figure 5.2 Subgap bias spectroscopy, experiment and model. 57
Figure 5.3 Even-odd Coulomb peak spacings. 58
Figure 5.4 Temperature and magnetic field dependence of the even-odd peak spacings. 59
Figure 6.1 Majorana island device. 69
Figure 6.2 Peak splitting in magnetic field. 71
Figure 6.3 Bias spectroscopy. 74
Figure 6.4 Length dependence of Coulomb peak heights. 76
Figure 6.5 Device Layouts. 78
Figure 6.6 Even-odd peak spacing summary. 79
Figure 6.7 Critical field measurement for 0.9 µm device. 81
Figure 6.8 Oscillating 1e-periodic peak spacings. 81
Figure 6.9 Angle dependence of state-continuum anti-crossing. 82

Figure 6.10 Gate positions. . . . . . . . . . . . . . . . . . . . 83
Figure 6.11 Comparison of peak spacings and bias spectroscopy. . . . . . . . . . . . . . . . . . . . . . . 84
Figure 6.12 Common-mode peak motion removal. . . . . . 85
Figure 6.13 Zero-energy state. . . . . . . . . . . . . . . . . . 87
Figure 6.14 Bias-spectroscopy at successive Coulomb peaks. 88
Figure 6.15 Measurement of the g-factor for three devices. 89
Figure 7.1 Device energetics and transport. . . . . . . . . 95
Figure 7.2 Even-odd effect and shadow-diamonds. . . . . 99
Figure 7.3 Coulomb blockade spectroscopy and shadow-peaks. . . . . . . . . . . . . . . . . . . . . . . . . 101
Figure 7.4 Comparison of magnetic field-directions. . . . 103
Figure 8.1 Calculation of peak skews. . . . . . . . . . . . . 108
Figure 8.2 Peak skews for $B_{||} = 140$ mT. . . . . . . . . . . 109
Figure 8.3 Peak shapes for $B_{||} = 140$ mT. . . . . . . . . . . 110
Figure 8.4 Peak skews for $B_{||} = 170$ mT. . . . . . . . . . . 110
Figure 8.5 Peak shapes for $B_{||} = 170$ mT. . . . . . . . . . . 111
Figure 8.6 Peak skews for $B_{||} = 235$ mT. . . . . . . . . . . 112
Figure 8.7 Peak shapes for $B_{||} = 235$ mT. . . . . . . . . . . 112
Figure 8.8 Peak skews in parallel magnetic field. . . . . . 113
Figure 8.9 Peak skews in transversal magnetic field. . . . 115

## LIST OF TABLES

---

Table 4.1 Different nanowire deposition methods. . . . 44
Table 4.2 Wafer specifications for the chip blanks. . . . 49
Table 4.3 Resist stack parameters of the UV-lithography step for making the chip blanks. . . . . . . . 49
Table 4.4 Resist parameters for making the etch windows. . . . . . . . . . . . . . . . . . . . . . . . . 49
Table 4.5 Parameters of the Al etch. . . . . . . . . . . . . 50
Table 4.6 Resist parameters for the electrostatic gates and Ohmic contacts. . . . . . . . . . . . . . . . 50
Table 4.7 Milling and evaporation parameters for the electrostatic gates and Ohmic contacts. . . . . 50

Table 6.1 Device length, $L$, charging energy, $E_\mathrm{C}$, lever arm, $\eta$, and characteristic amplitude, $A$, for the five measured devices. . . . . . . . . . . . . . . . 80
Table 6.2 All nonzero offset voltage values, $\delta V(B)$, for $L = 1.5$ µm device. . . . . . . . . . . . . . . . . . 86

# 1

# INTRODUCTION

The steady miniaturization of electronic components has led to an exponential increase in computing power, with transistor counts doubling every two years over the last four decades. As feature sizes approach their fundamental atomic limit, this exponential growth, described by Moore's law, is expected to slow, and new computing paradigms are needed to sustain increases in processing capacity. A means to this end is the rapidly growing field of quantum computing, in which classical logical elements like bits and gates are replaced by quantum analogues. The principles of quantum computing were introduced in the 1980s, when it was realized by Richard Feynman that an accurate simulation of physical systems, based on the underlying laws of quantum physics, cannot be done efficiently by a classical computer [1]. The proposed solution was to use engineered quantum systems to simulate other quantum systems, and to exploit the peculiarities of quantum physics, such as entanglement and quantum superpositions, for computational gain.

Theoretical research in the following decades led to the discovery of a multitude of quantum algorithms, some of which offer super-polynomial speed-up for problems like integer-factorization and discrete-logarithms [2], or polynomial speed-up for database search [3]. Integer-factorization and discrete-logarithms are perhaps the two applications driving the most investment in quantum computing research. They are intrinsically difficult for classical computers to solve, requiring unfeasibly long computation times for practically attainable key lengths (on the order of the age of the universe, or longer), and as such form the basis of most modern forms of cryptography. Their efficient execution on a sufficiently large scale fault-tolerant quantum computer could render most current forms of encryption vulnerable, which is the reason why military and intelligence agencies are among the major financial contributors to quantum computing research. The potential threat of a quantum computer for the secure transmission of information in civilian and military contexts has, conversely, led to the formation of the research field of post-quantum cryptography, secure against quantum computers, which is, ironically, also backed by military and intelligence agencies. Other, motivations for quantum computing research are the potential impact of quantum simulation, which could lead to breakthroughs in fields such as biology or medicine [4], or quantum annealing [5], which could offer speed-ups in optimization problems commonly found in the field of artificial intelligence [6,7].

The fundamental building block of a quantum computer, the qubit, is a two-level quantum system that can exist in a coherent superposition of states 0 and 1, described mathematically by a state vector $|\psi\rangle = \cos\frac{\theta}{2}|0\rangle + e^{i\phi}\sin\frac{\theta}{2}|1\rangle$. Implementations of qubits are real or approximate two-level systems made from physical components as diverse as atoms [8, 9], photons [10], nuclei [11], superconducting circuits [12–14], quantum dots [15], and non-abelian *anyons* [16, 17], among many others.

Quantum information stored in physical systems is intrinsically fragile and cannot be duplicated [18], making error correction difficult. Decades of experimental research have, as of 2016, increased coherence times and quantum gate fidelities so that that several hundred qubit operations can be performed before the quantum information is lost to decoherence [19]. This is of interest, because if single- and two-qubit gate operations become reliable enough, quantum error correction schemes [20] can come into play and extend coherence long enough to run fault-tolerant quantum computations. Quantum error correction, however, requires a large number of physical qubits to encode one logical qubit, with estimates of $10^3$ to $10^4$ physical qubits per logical qubit to achieve fault-tolerance for surface code architectures [21].

An alternative approach that attempts to build fault-tolerance right into the qubit hardware is to use non-abelian *anyons* [16]. Computations are performed by moving *anyons* around one another, which is known as braiding [16, 17]. A predicted realization of non-abelian *anyons* are Majorana modes in one-dimensional topological superconductors. As Majorana modes always come in pairs that form a single fermionic state with fixed quasiparticle parity $|0\rangle$ or $|1\rangle$, a logical qubit with fixed total parity can be created by combining two fermionic Majorana states such that $|\psi\rangle = \cos\frac{\theta}{2}|00\rangle + e^{i\phi}\sin\frac{\theta}{2}|11\rangle$ [17]. Due to the non-local nature of the fermionic state formed by two Majorana modes - they exist on opposite ends of the one-dimensional structure - this qubit would be protected from decoherence resulting from local perturbations [22]. The degree of non-locality and thus the protection of a Majorana qubit is given by the underlying wave function overlap of the constituent Majorana modes present on each side, which is expected to decrease exponentially with the length $L$ of the system according to $\propto e^{-L/\xi}$, with Majorana coherence length $\xi$ [22,23]. Despite these encouraging results, Majorana qubits are not protected from quasiparticle poisoning events that change the parity of individual Majorana states, which thus constitute a fundamental limit to their coherence [24]. If Majorana qubits are to be the means towards building a fault-tolerant quantum computer, exponential protection of Majorana modes needs to be demonstrated and quasiparticle poisoning rates need to be quantified.

The experimental work presented in this thesis is at the intersection between the mature research area of quantum dots [25] and the novel field of superconductor-semiconductor hybrids [26]. Chapters 2 and 3 introduce the physics of Majorana islands, semiconductor-superconductor nanowire hybrid quantum dots that can be brought into a topological superconducting phase at high magnetic fields, while Chapter 4 gives details on their fabrication. Based on measurements on Majorana islands, Chapter 6 reports the first observation of exponentially protected Majorana modes and extracts a coherence length $\xi = 260$ nm, implying that sufficient protection is possible at experimentally feasible device lengths in the micrometer range.

The main other source of decoherence in proposed Majorana qubits, quasiparticle poisoning, is explored for internal and external sources of quasiparticles. In this regard, Chapter 5 estimates a lower bound on the state parity lifetime of $\sim 10$ ms for poisoning from the proximitizing superconductor, potentially long enough to allow for many braiding operations. Poisoning from the Majorana island's normal metal leads is investigated in Chapter 7, with an extracted poisoning time of $\sim 3$ µs.

As no Majorana qubit has been demonstrated yet, it is unclear what its coherence will be, and whether the reality of topological quantum computation will live up to the expectations. While the complexity of the task is formidable, recent theoretical proposals for fusion rules [27], Majorana braiding [28], and topological quantum computation [29] schemes based on Majorana islands provide a clear roadmap for experimentalists to follow. On the way, they will characterize an exciting new class of quasiparticle, governed by non-Abelian statistics so far unobserved in nature. Their potential discovery carries a significance for physics on par with the impact of Majorana-based topological quantum computers. Hopefully it will be in a Majorana island.

# Part I

# THEORY AND FABRICATION

# 2

# MAJORANA MODES

This chapter will introduce Majorana modes and their emergence in quantum wires with proximity-induced superconductivity. It gives an overview of their fundamental properties, in particular those that are experimentally accessible by tunneling spectroscopy in Majorana island geometries. Much has been written about Majorana fermions, and for a more structured introduction into topological superconductivity, the reader is referred to the canonical review articles [30, 31].

## 2.1 HISTORICAL BACKGROUND

Majorana fermions were originally proposed by Italian physicist Ettore Majorana in 1937 as particles that are their own antiparticles [32]. They are one flavor of three kinds of fermions, the other being Weyl fermions [33] and the more commonly encountered Dirac fermions. Most of the fermions in the standard model of particle physics are Dirac fermions. This includes the six *quark* flavors *up*, *down*, *strange*, *charm*, *top* and *bottom* in addition to the three leptons *electron*, *muon* and *tauon*, and their respective antiparticles. The remaining three leptons, the *neutrinos*, are the *electron neutrino*, the *muon neutrino* and the *tauon neutrino*. It is currently not clear whether they belong to the Dirac fermion class, or whether they are Majorana fermions. As it has been hypothesized by Majorana himself that a neutrino and its antineutrino are actually the same particle, albeit with a flipped spin [34]. If neutrinos are indeed Majorana fermions, they would be the only elementary particle that have these properties.

Universally considered a genius, Majorana grew increasingly more reclusive and strange towards the end of his life [34]. He emptied his bank account and took the night boat from Naples to Palermo on March 23rd, 1938 [35]. In Palermo, he sent several dramatic letters to friends, hinting at a sudden disappearance and apologizing for his future actions. Two days later, on March 25th 1938, however, he took the night boat back to Naples, where he would never arrive. While there are anecdotal stories of him becoming a beggar in Naples or retreating into a monastery, the most widely held theory is that he committed suicide by jumping off the boat into the Mediterranean Sea.

In his 2009 review of Majorana physics [34], Frank Wilczek quotes Enrico Fermi as saying: "Majorana had greater gifts than anyone else in the world. Unfortunately he lacked one quality which other men generally have: plain common sense."

More than 50 years after Majorana's disappearance, it was realized that Majorana fermions can appear as excitations in topological superconductors [22, 23, 36], and are of interest for topological quantum computation due to their predicted non-Abelian exchange statistics [16, 17]. Subsequent theoretical proposals suggested semiconducting nanowires in proximity to a superconductor as a potential platform to realize a topological superconductor [37, 38]. This generated much experimental interest and led to a flurry of experiments reporting signatures of Majorana modes in nanowires [39–42], followed by the experimental discovery of Majorana physics in atomic chains [43].

## 2.2 MATHEMATICAL DESCRIPTION

Without much mathematical rigor, we will briefly introduce the mathematical description of Majorana fermions and demonstrate some of their properties [30]. We formally define the Majorana operators $\gamma_1$ and $\gamma_2$ by decomposing the fermionic annihilation and creation operators $c$ and $c^\dagger$ into their real and imaginary parts

$$c = \frac{1}{2}\left(\gamma_1 + i\gamma_2\right) \tag{2.1}$$

$$c^\dagger = \frac{1}{2}\left(\gamma_1 - i\gamma_2\right). \tag{2.2}$$

This definition implies that Majorana fermions can only come in pairs, with two Majorana fermions forming one fermionic state. This nomenclature is quite confusing, and we will do our best to distinguish whether we are referring to a single Majorana fermion or the fermionic Majorana state in the following discussion. Before we fill this with more physical meaning, it is instructive to see a few mathematical consequences resulting from the definition in Equations (2.1) and (2.2). By eliminating $\gamma_1$ or $\gamma_2$, respectively, we obtain

$$\gamma_1 = c + c^\dagger = \gamma_1^\dagger \tag{2.3}$$

and

$$\gamma_2 = i\left(c^\dagger - c\right) = \gamma_2^\dagger \tag{2.4}$$

and conclude that since their creation operator is equal to the annihilation operator, a Majorana fermion is its own antiparticle.

Following the definition in Equations (2.1) and (2.2), any fermionic state is formed by two Majorana fermions, but in most cases they are not spatially separated [30]. As most of the interesting physics arises when we create a fermionic state from two spatially separated Majorana operators, we will approach this next.

## 2.3 THE KITAEV CHAIN

Some of the central properties of Majorana modes can be understood using a simple toy model. Following Kitaev [22], we consider a 1D tight-binding chain of $N$ spinless electrons that act under a superconducting p-wave pairing. The corresponding Hamiltonian is given by

$$\begin{aligned} H_{\text{kit}} = \sum_{j=1}^{N} \Big[ - t \left( c_j^\dagger c_{j+1} + c_{j+1}^\dagger c_j \right) + \Delta_{\text{p}} c_j c_{j+1} + \Delta_{\text{p}}^* c_j^\dagger c_{j+1}^\dagger \\ - \mu \left( n_j - \frac{1}{2} \right) \Big], \end{aligned} \tag{2.5}$$

where $n_j = c_j^\dagger c_j$ is the number operator on site $j$, $\mu$ is the chemical potential, $\Delta_{\text{p}} = |\Delta_{\text{p}}| e^{i\theta}$ is the p-wave pairing gap, and $t$ is the hopping amplitude between sites $j$ and $j+1$.

We can safely disregard the phase dependence of the pairing gap by defining Majorana operators [22]

$$\begin{aligned} \gamma_{2j-1} &= e^{i\frac{\theta}{2}} c_j + e^{-i\frac{\Theta}{2}} c_j^\dagger \\ \gamma_{2j} &= -i e^{i\frac{\theta}{2}} c_j + i e^{-i\frac{\Theta}{2}} c_j^\dagger \end{aligned} \tag{2.6}$$

that fulfill the relationship $\gamma = \gamma^\dagger$.

Solving for $c_j$, $c_j^\dagger$ and inserting into Equation (2.5) yields

$$\begin{aligned} H_{\text{kit}} = \frac{i}{2} \sum_{j=1}^{N} \Big[ - \mu \gamma_{2j-1} \gamma_{2j} + \left( |\Delta_{\text{p}}| + t \right) \gamma_{2j} \gamma_{2j+1} \\ + \left( |\Delta_{\text{p}}| - t \right) \gamma_{2j-1} \gamma_{2j+2} \Big]. \end{aligned} \tag{2.7}$$

We will examine two cases of this Hamiltonian next. If we pick parameters $t = \Delta_{\text{p}} = 0$ and $\mu < 0$, Equation (2.7) reduces to

$$H_{\text{kit}} = -\mu \frac{i}{2} \sum_{j=1}^{N} \left( \gamma_{2j-1} \gamma_{2j} \right) = -\mu \sum_{j=1}^{N} \left( c_j^\dagger c_j - \frac{1}{2} \right). \tag{2.8}$$

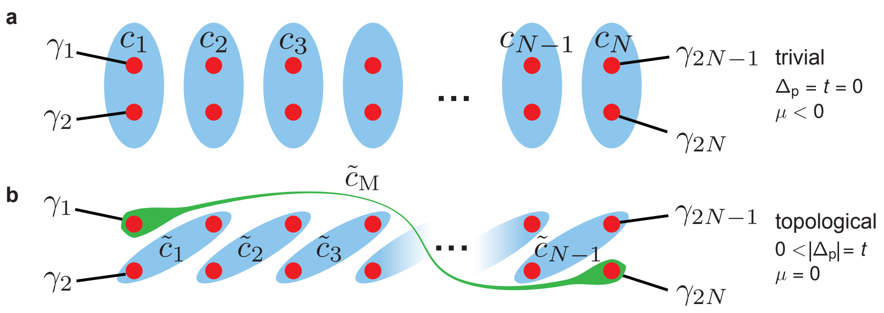

Figure 2.1: **Trivial and topological pairing in the Kitaev chain. a,** In the trivial regime, $\Delta_\text{p} = t = 0$, Majorana operators (red) from the same site form a fermion (light blue) with associated operator $c_j$. **b,** In the topological regime, such as for $0 < |\Delta_\text{p}| = t$, Majorana operators from adjacent sites form a fermion with operator $\tilde{c}_j$, leaving two unpaired Majorana operators at the chain ends that can be parameterized as a new fermion $\tilde{c}_\text{M}$ (green) at zero energy.

This describes the trivial case of $N$ non-interacting fermions on a chain, as shown in Figure 2.1a.

For the topological case $|\Delta_\text{p}| = t$ and $\mu = 0$, however, the Kitaev model finds [22]

$$H_\text{kit} = it \sum_{j=1}^{N} \gamma_{2j}\gamma_{2j+1} \tag{2.9}$$

If we now construct new fermion operators,

$$\tilde{c}_j = \frac{1}{2}(\gamma_{2j} + i\gamma_{2j+1}) \tag{2.10}$$

and

$$\tilde{c}_j^\dagger = \frac{1}{2}(\gamma_{2j} - i\gamma_{2j+1}), \tag{2.11}$$

that couple sites $2j$ and $2j+1$, we can write Equation (2.9) as

$$H_\text{kit} = 2t \sum_{j=1}^{N-1} \left( \tilde{c}_j^\dagger \tilde{c}_j - \frac{1}{2} \right). \tag{2.12}$$

The system of $N$ fermions with associated creation operators $c_j$ can, in this regime, therefore equivalently be described by $N-1$ fermions with associated operators $\tilde{c}_j$ that pair Majorana operators on sites $2j$ and $2j+1$, shown in light blue in Figure 2.1b, in addition to a highly delocalized fermion associated with annihilation operator

$$\tilde{c}_\text{M} = \frac{1}{2}(\gamma_1 + i\gamma_{2N}) \tag{2.13}$$

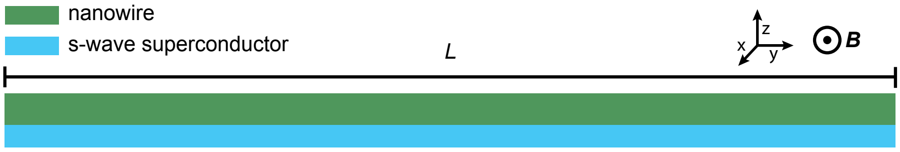

Figure 2.2: **Nanowire in proximity to a superconductor.** A magnetic field, **B**, can be applied along the nanowire axis.

and creation operator

$$\tilde{c}_M^\dagger = \frac{1}{2}\left(\gamma_1 - i\gamma_{2N}\right). \tag{2.14}$$

This peculiar pairing of the outermost Majorana operators is indicated schematically in green in Figure 2.1b.

We take note of a few interesting properties of the peculiar fermion described by $\tilde{c}_M$: It is composed of two Majorana operators, one at either end of the chain. It constitutes a zero-energy excitation of the system, as it does not appear in the Hamiltonian in Equation (2.12). Lastly, its emergence is independent of the chain length, as long as the system parameters stay constant along the chain.

## 2.4 NANOWIRE IN PROXIMITY TO A SUPERCONDUCTOR

In the previous treatment we have assumed that superconducting p-wave pairing had already been introduced in the chain. It was realized by several proposals [37,38] that similar physics can be obtained for semiconducting nanowires with high g-factors and strong spin-orbit coupling, as is the case for InAs [40,42] or InSb [39,41], in proximity to an s-wave superconductor like aluminum [40,42] or niobium titanium nitride [39,44].

We sketch the derivation in the proposals [37,38] by considering a single-mode nanowire of length $L$ with proximity induced s-wave superconducting pairing of strength $\Delta$ in an external magnetic field **B**, shown in Figure 2.2. We assume that the nanowire is pointing in the y-direction, that the magnetic field **B** is pointing in the x-direction, and that spin-orbit interaction is present in the nanowire and directed along the z-axis. The results of the following derivation are, however, valid as long as the magnetic field is orthogonal to the direction of spin-orbit coupling.

In Bogoliubov-de Gennes (BdG) notation, the Hamiltonian of this nanowire is given by [37, 38]

$$\hat{H} = \int_{0}^{L} \Psi^{\dagger}(y)\mathcal{H}\Psi(y)\mathrm{d}y \tag{2.15}$$

with

$$\mathcal{H} = \left(\frac{p^2}{2m} - \mu(y)\right)\tau_z + \frac{\alpha_\mathrm{R}}{\hbar} p\sigma_z\tau_z + g\mu_\mathrm{B}\frac{B(y)}{2}\sigma_x + \Delta(y)\tau_x, \tag{2.16}$$

spinor $\Psi^{\dagger} = \left(\psi^{\dagger}_{\uparrow}, \psi^{\dagger}_{\downarrow}, \psi_{\uparrow}, -\psi_{\uparrow}\right)$, and Pauli matrices $\tau$ and $\sigma$ operating in particle-hole space and spin space respectively. Here, $\mu$ is the chemical potential, $\mu_\mathrm{B}$ is the Bohr magneton, $\hbar$ is the reduced Planck constant, $p$ is the momentum operator, $g$ is the g-factor, $m$ is the electron mass, and $\alpha_\mathrm{R}$ is the strength of Rashba-type spin-orbit coupling.

Assuming constant $\mu$, $\alpha_\mathrm{R}$, $\Delta$ and $B$ along the nanowire, the eigenvalues can be easily calculated by squaring $\mathcal{H}$ twice [38], yielding

$$E_{\pm}^2 = E_\mathrm{Z}^2 + \Delta^2 + \xi_p^2 + \left(\frac{\alpha_\mathrm{R}}{\hbar}p\right)^2 \pm 2\sqrt{E_\mathrm{Z}^2\Delta^2 + E_\mathrm{Z}^2\xi_p^2 + (\frac{\alpha_\mathrm{R}}{\hbar}p)^2\xi_p^2} \tag{2.17}$$

with Zeeman-energy $E_\mathrm{Z} = g\mu_\mathrm{B}\frac{B}{2}$ and $\xi_p = \frac{p^2}{2m} - \mu$.

We will first assume the absence of superconductivity ($\Delta = 0$), no magnetic field ($B = E_\mathrm{Z} = 0$) and set $\mu = 0$ for simplicity. The dispersion relation reduces to

$$E_{\pm}\left(k_\mathrm{y}\right) = \frac{\hbar^2 k_\mathrm{y}^2}{2m} \pm \alpha_\mathrm{R} k_\mathrm{y}, \tag{2.18}$$

where we have made use of $p = \hbar k_\mathrm{y}$. This describes two parabolic bands, shifted by $\pm k_\mathrm{SO} = \pm\frac{m\alpha_\mathrm{R}}{\hbar^2}$ due to spin-orbit coupling, as shown in Figure 2.3a. The associated energy scale is the spin-orbit energy $E_\mathrm{SO} = \frac{m\alpha_\mathrm{R}^2}{2\hbar^2}$.

Applying a magnetic field will lead to a finite Zeeman term in Equation (2.17) and cause the opening of an energy gap of $2E_\mathrm{Z}$ at $k_\mathrm{y} = 0$, shown in Figure 2.3b. If the chemical potential is in the gap, as it is the case for $\mu = 0$, spin and momentum are locked. For sufficiently small fields $E_\mathrm{Z} < E_\mathrm{SO}$, spins for states with opposite wave-vector will be nearly anti-parallel (spin-$\leftarrow$ for $k_\mathrm{y} > 0$, spin-$\rightarrow$ for $k_\mathrm{y} < 0$) and the wire is in a helical state (Figure 2.3b). Increasing the magnetic field will push the lower band down, such that for $E_\mathrm{Z} \gg E_\mathrm{SO}$ and $\mu = 0$ spins will be nearly parallel (Figure 2.3c).

Next, we introduce a superconducting pairing by setting $\Delta > 0$ and, for simplicity, examine the special case that $\mu = 0$. Introducing

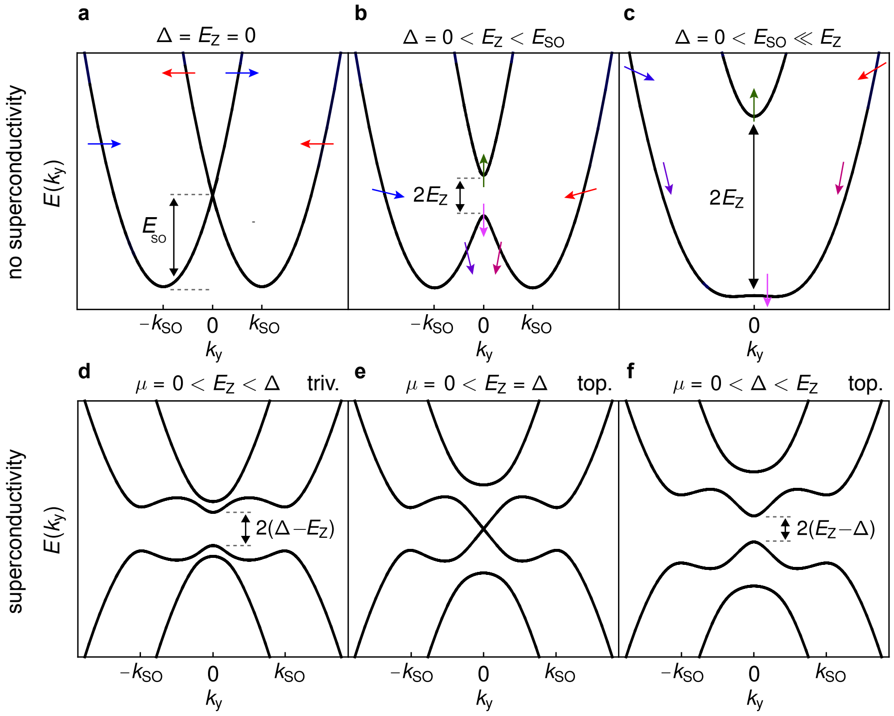

Figure 2.3: **Nanowire band structure. a,** Spin-split bands due to spin-orbit coupling in the non-superconducting regime. **b,** An applied magnetic field opens up a gap with magnitude $2E_Z$ at $k_y = 0$. For a chemical potential in the gap, states with $\pm k_y$ have nearly antiparallel spins. The nanowire is in a helical state. **c,** For a higher magnetic field so that $E_Z \gg E_{SO}$, and a chemical potential in the gap, spins at $\pm k_y$ are nearly parallel. **d,** BdG spectrum in the topologically trivial superconducting phase. **e,** For $E_Z = \Delta$, the gap closes and a topological phase transition takes place. **f,** At higher magnetic fields the gap at $k_y = 0$ reopens and the nanowire is in the topological superconducting phase.

superconducting pairing will double the bands due to electron-hole symmetry and, for $E_Z = 0$, open a gap of $\pm E_G = \Delta$ around the Fermi energy. For a finite magnetic field $E_Z < \Delta$, this gap is said to be pairing dominated, but reduced by the Zeeman term according to $\pm E_G = \Delta - E_Z$, shown in Figure 2.3d. The wire is still in the topologically trivial phase. For higher magnetic fields so that $E_Z = \Delta$, shown in Figure 2.3e, we find that $E_G = 0$ and the gap closes, which leads to an inversion of energy bands and a phase transition towards a topologically superconducting phase. As vacuum is topologically trivial, a band inversion has to take place at the system boundary, leading to the formation of near-zero energy Majorana states at the wire ends. For $E_Z > \Delta$, the gap is said to be Zeeman dominated with $\pm E_G = E_Z - \Delta$ at $k_y = 0$ the dominant energy gap at low fields. For higher fields, however, the gap at $k_\mathrm{y} = \pm k_\mathrm{SO}$ will be dominant due to the steadily increasing Zeeman gap at $k_\mathrm{y} = 0$.

While the band structures in Figure 2.3(d-f) have been calculated for the special case of $\mu = 0$, the requirement for the emergence of topological superconductivity in the general case is $E_\mathrm{Z} > \sqrt{\Delta^2 + \mu^2}$.

## 2.5 MODE HYBRIDIZATION FOR FINITE SYSTEMS

We saw that in the Kitaev model [22] the Majorana state is described by the operator $\tilde{c}_\mathrm{M} = \frac{1}{2}\left(\gamma_1 + i\gamma_{2N}\right)$ and we have motivated the emergence of Majorana states at the wire ends in the full treatment of the Hamiltonian in Equation (2.16). A complete analysis reveals that the individual Majorana wave functions for the left and right Majorana extend into the center of the nanowire on a characteristic length scale $\xi$. Calculating the exact spatial extent of a Majorana wave function is rather involved, making use of Green's functions and theoretical approaches beyond the scope of this thesis [45]. The results, insofar as they are relevant for an understanding of the presented physics, will be briefly summarized here, along with a sketch of the derivation.

For a nanowire with length $L$ and endpoints at $y = 0$ and $y = L$ we find for the wave function of the left Majorana [45]

$$\Psi_l(y) \propto e^{-\frac{y}{\xi}} e^{\pm i k_\mathrm{F,eff} y}. \tag{2.19}$$

One can further show that the right Majorana is described by

$$\Psi_r(y) = \sigma_z \Psi_l(L - y) \tag{2.20}$$

and thus

$$\Psi_r(y) \propto e^{-\frac{(L-y)}{\xi}} e^{\mp i k_\mathrm{F,eff} y}. \tag{2.21}$$

We note that the spatial dependence of the Majorana wave function is given by a periodic oscillation at the Fermi wavelength $\lambda_\mathrm{F} = \frac{2\pi}{k_\mathrm{F}}$ and an envelope that decays exponentially with distance from the end of the topological region. As Majoranas always come in pairs to form a single fermionic state, we can describe the fermionic state by

$$\Psi_\mathrm{M}(y) = c_l \Psi_l(y) + c_r \Psi_r(y) \tag{2.22}$$

with normalization requirement $|c_l|^2 + |c_r|^2 = 1$. Its energy is calculated [45] according to

$$\begin{aligned} \Delta E &= \frac{\int \Psi_\mathrm{M}^\dagger(y)\hat{H}\Psi_\mathrm{M}(y)\mathrm{d}y}{\int \Psi_\mathrm{M}^\dagger(y)\Psi_\mathrm{M}(y)\mathrm{d}y} \\ &\approx \hbar^2 k_\mathrm{F,eff}\frac{e^{-\frac{L}{\xi}}}{m\xi}\cos\left(k_\mathrm{F,eff}L\right) \\ &= \Delta E_\mathrm{max}\cos\left(k_\mathrm{F,eff}L\right). \end{aligned} \tag{2.23}$$

Due to the $e^{-\frac{L}{\xi}}$ term we expect a finite splitting for short nanowires with $L \sim \xi$, while for longer wires the amplitude of the energy splitting $\Delta E_\mathrm{max}$ will vanish exponentially with $L$. The $\cos\left(k_\mathrm{F,eff}L\right)$ factor will lead to oscillations of $\Delta E$ when varying $B$ or $\mu$ due to their effect on $k_\mathrm{F,eff}$. For the device geometries presented in this thesis, the device length $L$ is fixed and it is easier to vary magnetic field than chemical potential. According to BCS theory, the superconducting coherence length $\xi = \frac{\hbar v_\mathrm{F}}{\pi\Delta}$ decreases with the inverse of the gap [46]. Since the magnetic field dependence of the induced gap can be approximated by

$$\Delta(B) = \Delta_0\sqrt{1-\left(\frac{B}{B_\mathrm{C}}\right)^2}, \tag{2.24}$$

where $\Delta_0$ is the induced gap at $B = 0$, and $B_\mathrm{C}$ is the critical field of the superconductor, we expect the oscillatory amplitude $\Delta E_\mathrm{max}$ to increase as a function of magnetic field. This behavior is shown for a length of $L = 2,\ 1,$ and 0.4 µm in the numerical simulations in Figure 2.4, taken from Stanescu et al. [47].

## 2.6 STATE-CONTINUUM ANTI-CROSSING

The proposal to realize Majorana physics in semiconducting nanowires proximitized by a superconductor, outlined in Chapter 2.4, requires strong spin-orbit coupling, high g-factors, and induced superconductivity with high critical fields. In Chapter 2.5, it was motivated that the Majorana state obtains a finite energy $\Delta E = \Delta E_\mathrm{max}\cos\left(k_\mathrm{F,eff}L\right)$ after the topological phase transition, with magnetic field dependent oscillations due to the cosine factor.

Numerical simulations show a closing and reopening of the gap when crossing the topological phase transition, although local density of states arguments suggest that this is not necessarily visible in transport [48]. In the case of strong Majorana overlap and a finite energy splitting, simulations show that the magnetic field evolution of

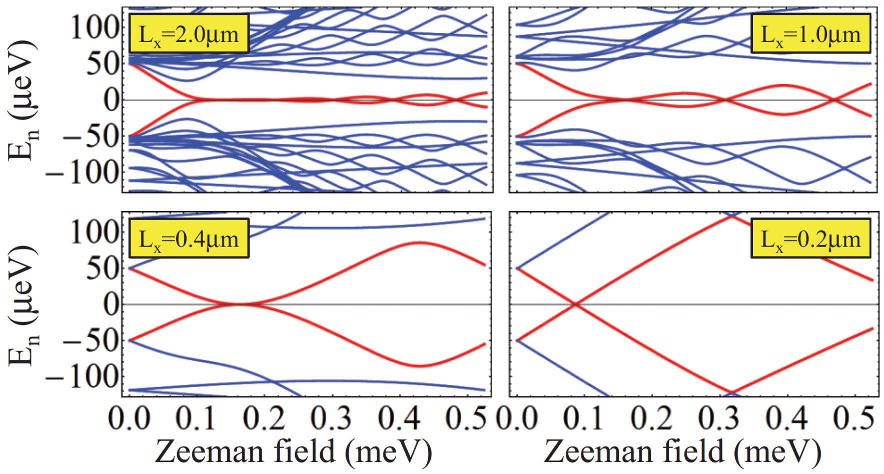

Figure 2.4: **Majorana mode hybridization.** Majorana state energies oscillate in an applied magnetic field. The amplitude of energy oscillation decreases for longer wire lengths $L_x$. The shortest wire length $L_x = 200\,\text{nm}$ on the order of the spin-orbit length $l_{SO} \sim 150$ nm, shows state crossings associated with an effective quenching of spin-orbit coupling. Figure adapted from Stanescu et al. [47].

the Majorana state is characterized by an anti-crossing between the hybridized Majorana mode and the next higher energy state at or near the turnaround point $\Delta E = E_{\text{max}}$ [47, 49]. This is shown in the simulations in Figure 2.4 for the $L = 2,\ 1,$ and 0.4 μm devices.

Of particular interest is the regime in which the device length becomes comparable to the spin-orbit length in the semiconductor. The simulations in Figure 2.4 are based on a spin-orbit length of $l_{SO} \sim 150$ nm. For $L = 0.2$ μm, spin-orbit coupling is effectively quenched, resulting in unprotected state crossings at finite energies after the zero-energy transition, which can be seen at $E_Z \sim 0.3$ meV in the bottom right panel in Figure 2.4. The effective absence of spin-orbit coupling additionally leads to a linear dependence of the state energy on the Zeeman field, as opposed to the non-linear dependence given by Equation (2.17) and evident for the other device lengths. Although it is highly overlapping and topologically unprotected, the finite-energy state for $L = 0.2$ μm in the regime $E_Z \sim 0.1 - 0.3$ meV is adiabatically connected to the Majorana modes arising for longer device lengths, see reference [47] for further information on this. It can therefore be seen as a Majorana-precursor state. In this regard, the experimental observation of a crossover between the different regimes in Figure 2.4, going from state crossings to state-anticrossings as the length is increased, is a strong indication of Majorana behavior.

## 2.7 WAVE FUNCTION AT THE TOPOLOGICAL PHASE TRANSITION

For the Coulomb-blockaded geometries in this thesis, a magnetic field is used to drive the nanowire into the topological regime. In the following section we will therefore analyze the transition into the topological phase as a function of magnetic field.

According to Equation (2.22), the topological regime of the nanowire is characterized by a highly non-local fermionic ground state with large weight at the ends of the topological region and an exponentially decaying tail [22, 23]. Due to the difficulty of spatially resolved probes at cryogenic temperatures, no experimental data that directly maps the wave functions of Majorana states exists for nanowire systems yet. Spatial probes on atomic chains, where energy scales are larger, have, however, impressively demonstrated midgap excitations localized at the chain ends, which were identified as Majorana modes [43].

Theoretical simulations for nanowires with strong spin-orbit coupling show that for certain system parameters Andreev bound states can be localized at the wire ends even in the topologically trivial phase [48, 50]. This seems counter-intuitive, as the delocalized nature of Majorana modes is heralded as one of their defining characteristics. The wave function peaks at the end can, however, be understood by examining the BdG spectrum as a function of different values of the chemical potential.

The insets of Figure 2.5 shows the calculated BdG spectrum in the trivial (red, $B = 0.9B_\mathrm{T}$) and topological (yellow, $B = 1.1B_\mathrm{T}$) regime for two values of chemical potential $\mu$ in an $L = 4.5\,\mu\mathrm{m}$ nanowire. Here, $B_\mathrm{T}$ denotes the magnetic field at which the topological phase transition takes place. The main panels shows the spatial extent of the wave function belonging to the lowest lying state. In the case of the topological regime (yellow) this is the Majorana state at $E = 0$. In the trivial regime (red), on the contrary, the ground state is the lowest lying state in the energy band.

We first turn our attention to the calculation for $\mu = 2\Delta$, shown in Figure 2.5a. To our initial surprise, the ground state in both the topological (yellow) and the trivial (red) regime has strong wave function weight at the wire ends, with both curves looking very similar at first glance.

We compare this to a simulation for $\mu = \Delta/2$ in Figure 2.5b. For this value of chemical potential, the Majorana state (yellow) is localized at the wire ends, while the lowest energy mode in the trivial regime

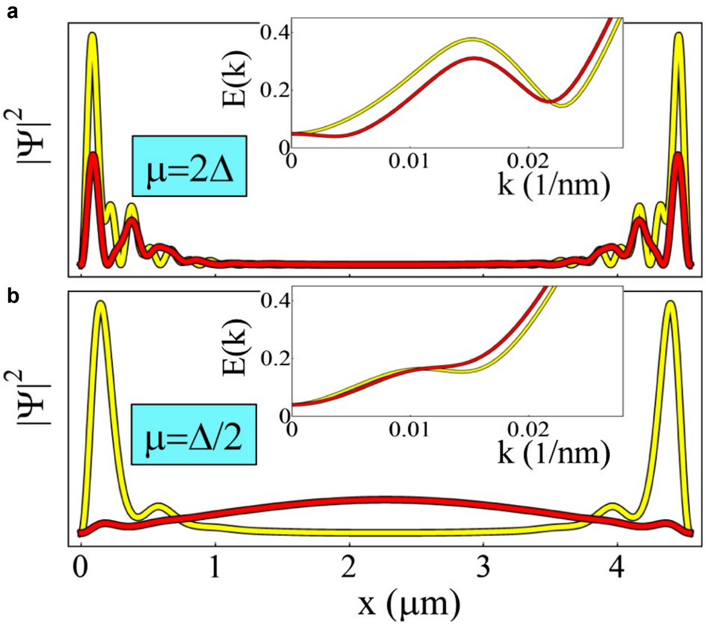

Figure 2.5: **Ground state wave functions.** Calculated $|\Psi|^2$ of the lowest energy BdG states in the trivial (red, $B = 0.9B_{\mathrm{T}}$) and the topological (yellow, $B = 1.1B_{\mathrm{T}}$) state, as a function of position $x$ along the nanowire, for two values of the chemical potential $\mu$. $B_{\mathrm{T}}$ is the magnetic field at which the topological phase transition takes place. Inset shows the calculated BdG spectrum. **a,** For $\mu = 2\Delta$, the simulations show that even in the topologically trivial case (red), the ground state can be localized at the wire ends and look superficially similar to the Majorana wave function (yellow). This is associated with the band minimum at finite $k$ that leads to a localization at the wire ends (inset, red curve). **b,** For $\mu = \Delta/2$, the Majorana state (yellow) is characterized by large wave function weight at the ends of the wire. The trivial ground state (red) is given by a delocalized bulk mode, which can be associated with the band minimum at $k \sim 0$ (inset, red curve). Figure adapted from Stanescu et al. [48].

(red) is now delocalized with an anti-node in the center of the wire and nodes at both ends, reminiscent of the first mode of a particle in a one-dimensional box [51].

The reason for this striking behavior can be found in the BdG spectrum shown in the insets of both panels. For $\mu = 2\Delta$ the minimum of the BdG spectrum in the trivial regime is at finite wave-vector $k$, resulting in a ground state with a small wavelength and a localized wave function. On the contrary, the trivial regime for $\mu = \Delta/2$ is characterized by a minimum of the energy band at $k = 0$, resulting in a long-wavelength mode with $\lambda \sim 2L$.

Understanding this behavior is of fundamental importance to the interpretation of transport experiments that probe Majorana states using tunneling spectroscopy. Here, a sudden increase in state-lead coupling could be indicative of a phase transition of the type shown in Figure 2.5a [42], whereas the absence of a drastic change in observed coupling could suggest the type shown in Figure 2.5b.

Finally, we note that despite the similarity of the two wave functions for $\mu = 2\Delta$, the trivial wave function is not characterized by the exponential decay towards the inside of the nanowire given by Equation (2.22).

## 2.8 CONCLUSION

From a historical perspective, the first experiments reporting signatures of Majorana modes in nanowires have used single-ended tunneling spectroscopy [39, 40] to probe Majorana states. For single-ended geometries, in which the superconductor is grounded, transport through a Majorana state at $E = 0$ manifests itself in a zero-bias conductance peak that appears at a finite magnetic field corresponding to the topological phase transition inside the nanowire.

The experiments in this thesis differ from previous studies on Majorana wires, as they are based on a geometry in which the superconducting region is of mesoscopic size, and electrically isolated from source and drain contacts by two tunnel barriers. Based on our knowledge of Majorana fermions, we will examine the physics of such systems in the next chapter.

# 3

# QUANTUM DOTS AND TUNNELING SPECTROSCOPY

Quantum dots are artificial structures in which electrons can be confined. The confinement potential causes a discretization of their electronic spectrum, which is why they are colloquially referred to as artificial atoms. The ability to engineer their spectra has led to the development of quantum dot based LEDs [52–54] in quantum dot displays, quantum dot lasers [55,56], sensors [57–59], solar cells [60,61], or field effect transistors [62,63], among others. In addition, quantum dots have many applications in quantum information science, where they can be used as qubits [15,64,65]. They can be composed from a wide variety of host materials and geometries, such as two-dimensional electron gases [15,66–68], carbon nanotubes [69], graphene [59], and nanowires [42,70–72].

This chapter will focus on the transport properties of quantum dots, and introduce the theoretical basics of Coulomb-blockade spectroscopy, a highly useful technique to measure subgap state energies in Majorana islands.

## 3.1 TRANSPORT THROUGH QUANTUM DOTS

In this thesis, nanowire superconductor-semiconductor hybrid quantum dots connected to normal-metal leads are probed by measuring electron transport in the Coulomb blockade regime, with weak dot-lead conductance $g \ll \frac{e^2}{h}$, where $e^2/h$ is the conductance quantum. Coulomb blockade implies that $E_C \gg k_B T$, with quantum dot charging energy $E_C = e^2/C_\Sigma$, and total quantum dot capacitance $C_\Sigma$, so that the total charge on the dot, $N$, is a good quantum number.

Electron transport in Coulomb blockade is a useful tool to measure the spectrum of electronic states inside the dot, as it allows to infer ground state energies based on the spacing and movement of Coulomb peaks, that occur at degeneracies of charge states [25,73]. As this is one of the main spectroscopic techniques of the work in this thesis, the relevant theory will be sketched in the following section.

We consider a quantum dot connected to metallic source and drain electrodes, with chemical potentials $\mu_\mathrm{S}$ and $\mu_\mathrm{D}$, respectively. The quantum dot is capacitatively coupled to a gate with applied voltage $V_\mathrm{G}$, and gate capacitance $C_\mathrm{G}$. The ground state energy of the quantum dot occupied by $N$ electrons is then given by [67]

$$E(N) = \sum_n \epsilon_n + \frac{\left(-e(N-N_0) + C_\mathrm{G} V_\mathrm{G}\right)^2}{2C_\Sigma}, \tag{3.1}$$

with single-particle energy levels $\epsilon_n$ due to quantum confinement, total dot capacitance including contributions from source and drain $C_\Sigma = C_\mathrm{G} + C_\mathrm{S} + C_\mathrm{D}$, and assuming $N_0$ electrons on the quantum dot at $V_\mathrm{G} = 0$.

We define the quantum dot's electrochemical potential for an occupation of $N$ as the energy required to add the $N$-th electron if the quantum dot is already occupied by $N-1$ electrons [74], that is

$$\mu_N = E(N) - E(N-1) = \epsilon_N + \frac{e^2(N - N_0 - 1/2)}{C_\Sigma} - \frac{eC_\mathrm{G}V_\mathrm{G}}{C_\Sigma}. \tag{3.2}$$

For small bias voltages in the linear regime, sequential through the quantum dot, by successively filling and removing the $N$-th electron, occurs at a gate voltage $V_\mathrm{G}^N$ chosen so that $\mu_\mathrm{S} = \mu_\mathrm{D} = \mu_N = 0$. We make use of Equation (3.2) to obtain

$$V_\mathrm{G}^N = \eta^{-1}\left(\epsilon_N + \frac{e^2(N - N_0 - 1/2)}{C_\Sigma}\right), \tag{3.3}$$

where we have defined the gate lever arm $\eta = eC_\mathrm{G}/C_\Sigma$. The spacing between two subsequent peaks is given by [75]

$$\begin{aligned} S = V_\mathrm{G}^N - V_\mathrm{G}^{N-1} &= \eta^{-1}\left(\epsilon_N - \epsilon_{N-1} + \frac{e^2}{C_\Sigma}\right) \\ &= \eta^{-1}\left(\Delta E_N + E_\mathrm{C}\right), \end{aligned} \tag{3.4}$$

where $\Delta E_N$ is the energy spacing between the $(N-1)$th and $N$th energy level. For semiconducting quantum dots, $\Delta E_N > 0$ for all $N$, as we are subsequently filling states that are increasingly higher in energy. As will be shown in Chapter 3.3, this does not hold anymore for superconductor-semiconductor hybrid quantum dots, where $\Delta E$ can be negative due to the presence of a superconducting condensate.

From Equation (3.4) we deduce that a variation in $\Delta E$ for subsequent charge states leads to variations in the Coulomb blockade peak spacing $S$. The conceptually easiest example of this is the filling of spin-degenerate energy levels in a carbon nanotube quantum dot [69].

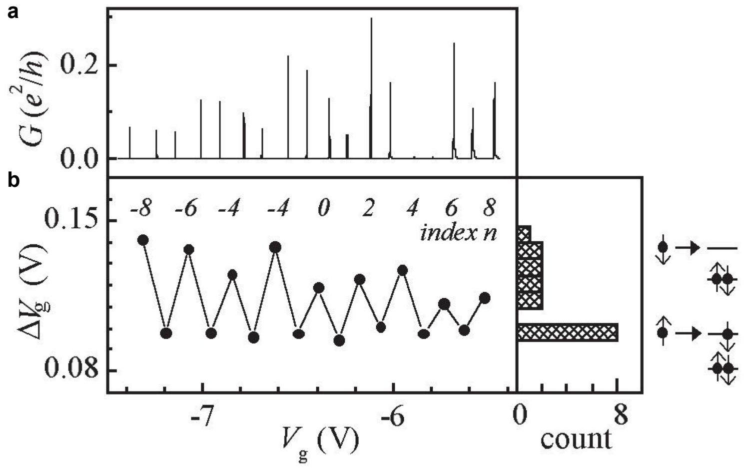

Figure 3.1: **Shell filling in a carbon nanotube quantum dot. a,** Differential conductance, $G$, as a function of gate voltage, $V_g$, showing a series of Coulomb peaks. **b,** The peak spacing, $\Delta V_g$, as a function of peak index exhibits an alternating pattern. (right panel) The histogram of peak spacings shows a bi-modal distribution, suggesting that the larger spacings are due to the additional energy cost of adding an electron into a new shell, whereas for lower spacings an electron with different spin direction is added to an already occupied shell. Figure adapted from Cobden et al. [69].

As shown conceptually in Figure 3.1, each spin-degenerate level can take exactly one spin-$\uparrow$ and one spin-$\downarrow$ electron. For an even $N$, levels are spaced by $\Delta E = \epsilon_{N+1} - \epsilon_N$, with single-level energies $\epsilon_n$. For the transition from odd $N$ to even $N$, we are instead filling a spin-$\uparrow$ electron into the level already occupied by a spin-$\downarrow$ electron, and consequently only have to pay the charging energy.

The Coulomb peak spacing in gate voltage is then given according to $S = \eta^{-1}\left(E_C + p_N\left(\epsilon_{N+1} - \epsilon_N\right)\right)$ with $p_N = 1$ ($p_N = 0$) if $N$ is even (odd). This leads to a Coulomb blockade pattern in which every even Coulomb valley is larger than the odd, as shown in Figure 3.1, and in which the spacing is directly related to the energy of the states in the quantum dot.

## 3.2 BIAS SPECTROSCOPY OF N-S INTERFACES

We derived in the previous section that the ground state of quantum dots can be spectroscopically probed using the position of Coulomb peaks. By peak movement alone, however, we cannot infer the energy of excited states of the quantum dot. This necessitates techniques such as bias spectroscopy, which we will briefly introduce.

In a landmark paper, Blonder, Tinkham and Klawijk studied transport at interfaces between a normal metal and a superconductor [75], in the following referred to as an N-S interface. As charge carriers in the superconductor are Cooper pairs at the Fermi energy, and a continuum of higher energy quasiparticles, while the normal metal has electrons, they were interested in the conversion from normal to supercurrent as a function of the barrier strength $Z$ at the N-S interface. They found that for very opaque barriers ($Z^2 \gg 1$) the current through the N-S junction at applied bias $V_{\mathrm{SD}}$ is given by

$$I_{\mathrm{NS}}\left(V_{\mathrm{SD}}\right) = \frac{1}{eR_{\mathrm{N}}} \int_{-\infty}^{\infty} \left[f_0\left(E - eV_{\mathrm{SD}}\right) - f_0\left(E\right)\right] D_{\mathrm{S}}(E) \mathrm{d}E, \tag{3.5}$$

where $f_0(E)$ is the Fermi distribution function for electrons at energy $E$, $R_{\mathrm{N}}$ is the normal state resistance, and $D_{\mathrm{S}}(E)$ is the density of states of the superconductor at energy $E$. Setting $\mu = 0$, the differential conductance at bias voltage $V_{\mathrm{SD}}$ consequently reduces to

$$\begin{aligned} g(V_{\mathrm{SD}}) &= \frac{\mathrm{d}I}{\mathrm{d}V_{\mathrm{SD}}} \\ &= \frac{1}{eR_{\mathrm{N}}} \int_{-\infty}^{\infty} \frac{\mathrm{d}f_0\left(E - eV_{\mathrm{SD}}\right)}{\mathrm{d}V_{\mathrm{SD}}} D_{\mathrm{S}}(E) \mathrm{d}E. \end{aligned} \tag{3.6}$$

We use that in the zero temperature limit the Fermi function becomes the Heaviside step function $f_0(E) = \Theta(-E)$, and that

$$\mathrm{d}\Theta(x)/\mathrm{d}x = \delta(x). \tag{3.7}$$

Inserting into Equation (3.6) yields

$$\begin{aligned} g(V_{\mathrm{SD}}) &\overset{T \to 0}{=} \frac{1}{eR_{\mathrm{N}}} \int_{-\infty}^{\infty} \frac{\mathrm{d}\Theta\left(eV_{\mathrm{SD}} - E\right)}{\mathrm{d}V_{\mathrm{SD}}} D_{\mathrm{S}}(E) \mathrm{d}E \\ &= \frac{1}{eR_{\mathrm{N}}} \int_{-\infty}^{\infty} \delta\left(eV_{\mathrm{SD}} - E\right) D_{\mathrm{S}}(E) \mathrm{d}E \\ &= \frac{1}{eR_{\mathrm{N}}} D_{\mathrm{S}}(eV_{\mathrm{SD}}), \end{aligned} \tag{3.8}$$

from which we conclude that the differential conductance at $V_{\mathrm{SD}}$ in the zero-temperature limit is proportional to the density of states of the superconductor at $E = eV_{\mathrm{SD}}$. We can thus spectroscopically probe states in the superconductor by measuring differential conductance as a function of bias voltage, which is known as bias spectroscopy. While we sketched the result for N-S interfaces, the analogous calculation for an N-S-N double-junction, or even a superconducting quantum dot, is more involved and analytically unexplored for Majorana islands.

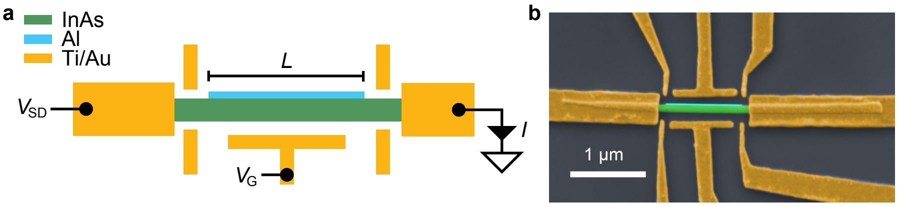

Figure 3.2: **Majorana island device. a,** The InAs nanowire (green) with epitaxial Al island (light blue) of length $L$ is contacted by normal metal (Ti/Au) Ohmic contacts (yellow). A bias voltage, $V_{SD}$, can be applied across the device, with measured current $I$ indicated. **b,** Electron micrograph (false colored) of a fabricated device.

## 3.3 DENSITY OF STATES OF A MAJORANA ISLAND

With Coulomb-blockade spectroscopy and bias spectroscopy, we have two powerful tools at hand to probe states inside the Majorana island. We will examine the expected density of states of Majorana islands next.

The type of Majorana island which is discussed in this thesis is an indium arsenide nanowire coated with an epitaxial aluminum island of length $L$, schematically shown in Figure 3.2, and coupled to normal metal (titanium/gold) Ohmic contacts (for fabrication details see section 4.4) through a semiconducting wire segment. The bare InAs region allows to tune the coupling to the leads by changing the density in the semiconductor using electrostatic cutter gates, while the chemical potential of the device is controlled by applying a voltage $V_G$ to a plunger gate.

The epitaxial coupling between the superconducting Al and the semiconducting InAs causes the semiconductor to inherit the superconducting properties of the Al [76]. This proximity effect can be modeled for Majorana wires in different ways, which we will briefly review. An effective superconducting pairing can be either introduced "by hand" [37,38] (such as for the Hamiltonian in Equation (2.16), and in Figure 3.3a, taken from Chevallier et al. [50]), or by explicitly modeling the tunnel coupling between the semiconductor and the superconductor [48,50,77,78], schematically shown in Figure 3.3b. The latter has the advantage that the calculated density of states accurately reflects the finite level spacing inside the semiconducting nanowire due to longitudinal quantization along the nanowire axis. At energies larger than the superconducting gap, $\Delta$, the density of states is continuous, as expected for a superconductor. For energies below the superconducting energy gap, however, multiple Andreev bound

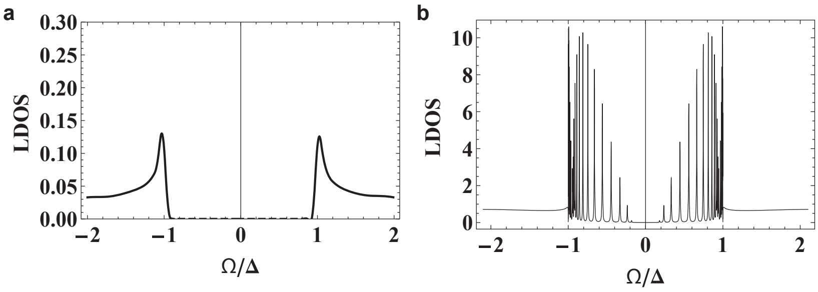

Figure 3.3: **Superconducting proximity effect.** Local density of states (LDOS) in a nanowire in proximitiy to a superconductor as a function of energy $\Omega$, normalized to the energy gap of the proximitizing superconductor $\Delta$. **a,** Superconducting pairing introduced "by hand". **b,** Proximity effect modeled using a hopping term between the superconductor and the semiconductor, showing the emergence of Andreev bound states at energies smaller than the gap. Figure adapted from Chevallier et al. [50].

states (ABS) appear in the spectrum. Their energy spacing $\propto 1/L$ reflects the quantization along the nanowire axis [50], where $L$ is the nanowire length. The number of Andreev levels with $0 < E < \Delta$ is given roughly by the ratio between level spacing and $\Delta$. The energy of the lowest subgap state and consequently the quality of the proximity effect is determined by the coupling between the semiconductor and the superconductor, with stronger coupling resulting in higher state energies up until the gap-edge [78,79].

The numerical results shown in Figure 3.3b were modeled for a system with level spacing significantly smaller than the superconducting gap. For level spacings comparable to the gap, which was experimentally found to apply for shorter devices with $L < 1$ µm [42,72], only a single ABS contributes to the density of states at energies $E < \Delta$. The complete density of states of the hybrid system, in this approximation, is consequently given by the sum of the BCS density of states $\rho_{\mathrm{BCS}}$, and that of the Andreev state, $\rho_0$, according to [72]

$$D(E) = \rho_{\mathrm{BCS}}(E) + \rho_0(E). \tag{3.9}$$

The BCS density of states can be approximated as [46]

$$\rho_{\mathrm{BCS}}(E) = \frac{\rho_{\mathrm{Al}} V |E|}{\sqrt{E^2 - \Delta(B)^2}} \theta\left(|E| - \Delta(B)\right), \tag{3.10}$$

with normal-state density of states per volume in the aluminum, $\rho_{\mathrm{Al}}$, aluminum volume $V$, and the magnetic field dependent superconducting energy gap

$$\Delta(B) = \Delta_0 \sqrt{1 - \left(\frac{B}{B_C}\right)^2}, \tag{3.11}$$

with zero-field gap $\Delta_0 \sim 180 - 200$ µeV for aluminum.

As the Andreev state is spinful, its energy $E_0^{\pm}$ for each spin direction is given by

$$E_0^{\pm}(B) = \frac{\Delta(B)}{\Delta_0} E_0(B = 0) \pm \frac{1}{2} g \mu_B B, \tag{3.12}$$

where the first term takes into account the lowering of the state energy due to the magnetic field-induced suppression of the superconducting gap, and the second term is the Zeeman energy $E_Z$.

The density of states contribution for each spin direction $\rho_0^{\pm}$ is taken to be a Lorentzian level with broadening $\gamma$. Due to electron hole symmetry $D(E) = D(-E)$ we should include positive and negative energies for each spin direction according to

$$\rho_0^{\pm}(E) = \frac{\gamma/2\pi}{(E - E_0^{\pm})^2 + (\gamma/2)^2} + \frac{\gamma/2\pi}{(E + E_0^{\pm})^2 + (\gamma/2)^2}, \tag{3.13}$$

yielding for the total density of states contribution of the Andreev state

$$\rho_0(E) = \frac{1}{2}\left(\rho_0^{+}(E) + \rho_0^{-}(E)\right). \tag{3.14}$$

The prefactor of $\frac{1}{2}$ is necessary because we artificially doubled the states in Equation (3.13). In this formalism the normalization of each Lorentzian in Equation (3.13) implies that $\int_{-\infty}^{+\infty} \rho_0^{\pm}(E)\mathrm{d}E = 2$, but the state corresponding to the two terms can not be occupied simultaneously, which we need to correct for.

Inserting Equations (3.10) and (3.14) into Equation (3.9) we arrive at

$$D(E) = \frac{\rho_{\mathrm{Al}} V |E|}{\sqrt{E^2 - \Delta(B)^2}} \theta\left(|E| - \Delta(B)\right) + \frac{1}{2}\left(\rho_0^{+}(E) + \rho_0^{-}(E)\right), \tag{3.15}$$

the total density of states of a Majorana island in the large level spacing regime. This is sketched and compared to a measurement in Figure 3.4.

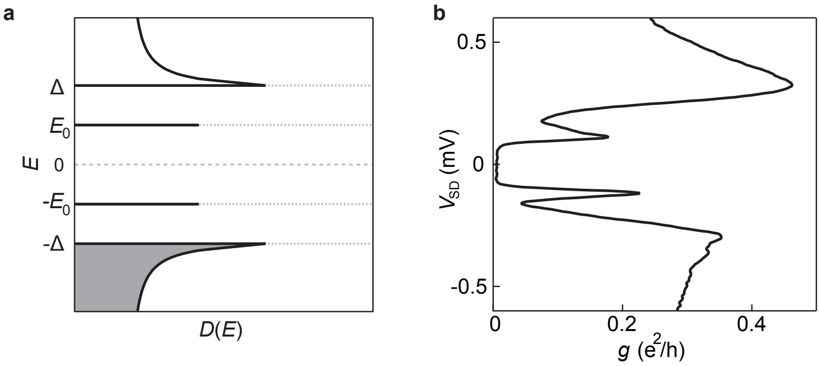

Figure 3.4: **Density of states of a Majorana island. a,** For a large level spacing, the density of states can be approximated as a Bardeen-Cooper-Schrieffer continuum at energies larger than the superconducting energy gap Δ in addition to a single subgap state at energy $E_0$. **b,** Tunneling spectroscopy in a Majorana island with $L = 310$ nm shows transport through a single subgap state and a higher energy continuum [72].

## 3.4 COULOMB-BLOCKADE SPECTROSCOPY OF MAJORANA ISLANDS

In Chapter 3.1 we learned how peak spacings in quantum dots relate to state energies, which we explored in Chapter 3.3 for semiconductor-superconductor hybrid nanowires. Combining the two, we will now proceed to apply the theory of Coulomb blockade to Majorana islands. The interesting property of this hybrid system is that while a single quasiparticle must occupy the subgap state at $E = E_0$, superconductivity provides an even-$N$ ground state in which all quasiparticles pair up into Cooper pairs at $E = 0$. This will give rise to an even-odd effect that is qualitatively different from the subsequent filling of spin-degenerate shells [80].

Following Equation (3.1), the energy of the quantum dot with $N$ electrons can be written as

$$E_N = \frac{E_C}{2}(N_G - N)^2 + p_N E_0 \tag{3.16}$$

with $p_N = 0$ for even and $p_N = 1$ for odd $N$. This describes a series of parabolas, which is shown in Figure 3.5 for three state energies $E_0$. Transport through the device can occur at degeneracies of charge states, indicated by solid circles.

The dominant transport process through the Majorana island depends critically on the ratio of charging energy and subgap state energy. In the first regime, $E_0 > E_C/2$, there is an even-$N$ ground state

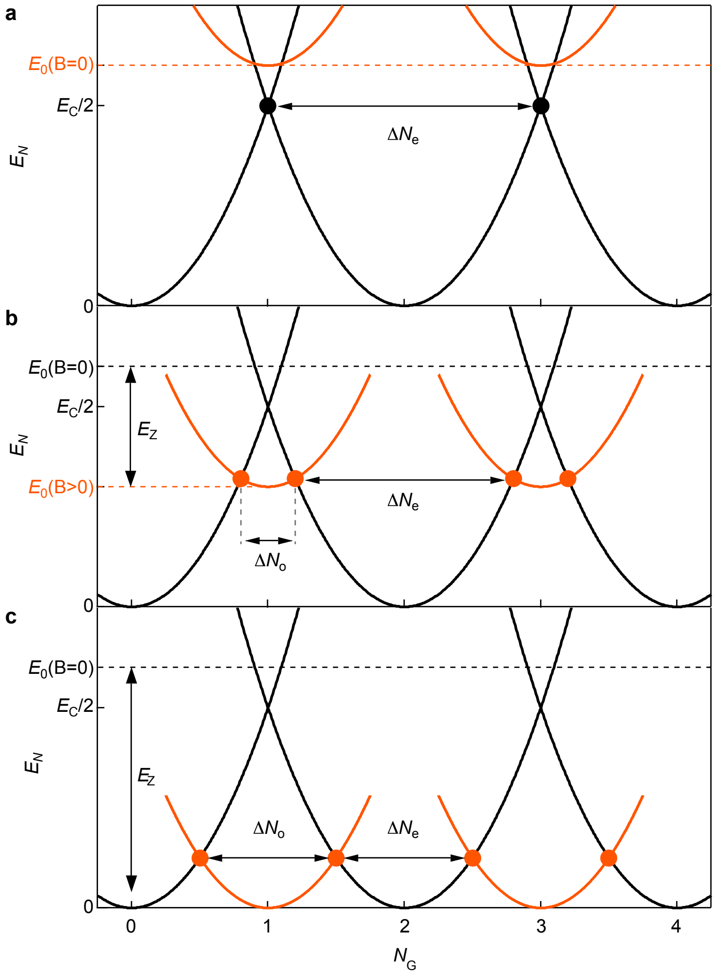

Figure 3.5: **Energy of a Majorana island. a,** For a subgap state energy $E_0 > E_C/2$ at $B = 0$, Coulomb peaks occur at degeneracies of charge states differing by $2e$, indicated by solid black circles, and feature an even spacing $\Delta N_e$ (see text). **b,** In an applied magnetic field, $E_0$ is lowered by the Zeeman energy $E_Z$. For $E_0(B > 0) < E_C/2$, an odd ground state emerges around integer values of $N_G$. Coulomb peaks can now occur at degeneracies of charge states differing by $1e$, indicated by solid orange circles, and feature even and odd spacings of $\Delta N_e$ and $\Delta N_o$. **c,** For $E_0(B) = 0$, i.e. $E_Z = E_0(B = 0)$, degeneracies occur at half-integer values of $N_G$, leading to evenly spaced Coulomb peaks with $\Delta N_e = \Delta N_o$.

for any value of $N_G$. This leads to degeneracies of even-$N$ states at odd-integer values of $N_G$, indicated by black solid circles in Figure 3.5a. Coulomb peaks, occurring at degeneracies of charge states, are thus regularly spaced and $2e$ periodic. As $N$ and $N+2$ states differ by a charge of $2e$, the device is subsequently charged with Cooper pairs, with Andreev reflection between the leads and the superconducting island as the dominant transport process at the degeneracy points. A measurement that shows this effect for a Majorana island with $L = 790$ nm [42] is shown in Figure 3.6a.

In the second regime, $E_0 < E_C/2$, diagrammed in Figure 3.5b, an odd ground state becomes available around integer values of $N_G$. This regime can be achieved by engineering the device parameters for a large charging energy, or, as indicated in Figure 3.5b, by lowering $E_0$ by the Zeeman energy $E_Z$ in an applied magnetic field $B$.

Coulomb peaks can now occur at degeneracies of states that differ by one charge, resulting in quasiparticle tunneling as the dominant transport process. Assuming $N$ is even, the peak position in gate-induced charge on the higher gate voltage side, $N_{G,oe}$, of an odd valley can be calculated by setting $E_{N-1} = E_N$, i.e.

$$\frac{E_C}{2}\left(N_{G,oe} - (N-1)\right)^2 + E_0 = \frac{E_C}{2}\left(N_{G,oe} - N\right)^2 \tag{3.17}$$

and therefore

$$N_{G,oe} = N - \frac{1}{2} - \frac{E_0}{E_C}. \tag{3.18}$$

Correspondingly, for the peak on the higher gate voltage side, $N_{G,eo}$, of the subsequent even valley we find

$$N_{G,eo} = N + \frac{1}{2} + \frac{E_0}{E_C}. \tag{3.19}$$

The spacings for even and odd Coulomb valleys, $\Delta N_e$ and $\Delta N_o$ which are indicated in Figure 3.5b, are thus given by

$$\begin{aligned}\Delta N_e &= N_{G,eo} - N_{G,oe} \\ &= 1 + 2\frac{E_0}{E_C}\end{aligned} \tag{3.20}$$

and

$$\Delta N_o = 2 - \Delta N_e = 1 - 2\frac{E_0}{E_C}. \tag{3.21}$$

We can convert into a spacing in gate voltage using the lever arm and the charging energy, according to $S_{e,o} = \eta^{-1} E_C \Delta N_{e,o}$, see section 3, and derive an even Coulomb valley spacing

$$S_e = \eta^{-1}\left(E_C + 2E_0\right) \tag{3.22}$$

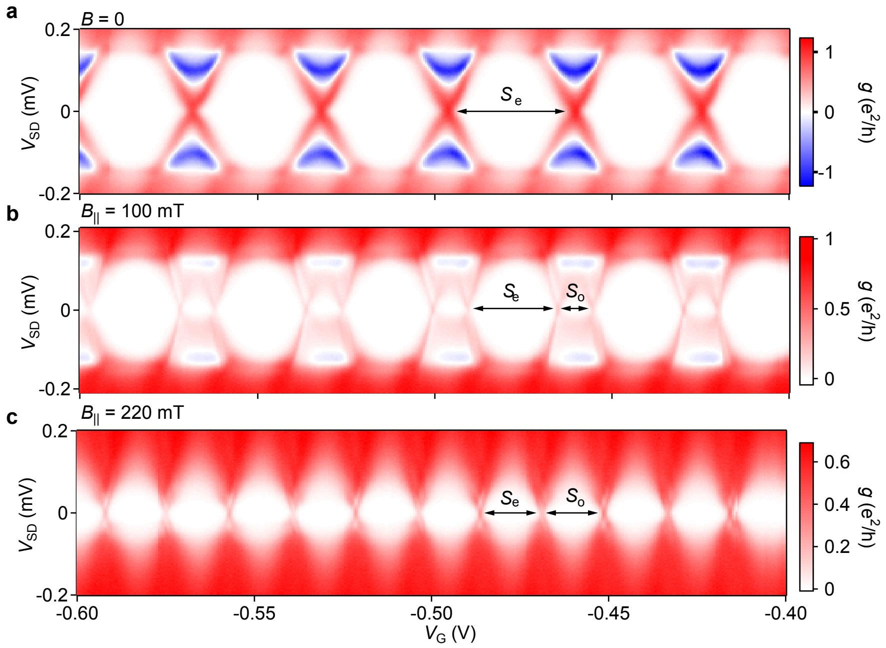

Figure 3.6: **Transport regimes of a Majorana island.** Differential conductance $g$ as a function of gate voltage $V_G$, and source-drain bias $V_{SD}$, for different magnitudes of the applied parallel magnetic field $B_{||}$ in an $L = 790$ nm Majorana island [42]. **a,** For $B = 0$, Coulomb diamonds are $2e$ periodic and evenly spaced with width $S_e$ at $V_{SD} = 0$. Conductance at high bias $V_{SD} \sim 0.2$ mV is $1e$ periodic. **b,** For $B_{||} = 100$ mT, $S_e$ decreases and an odd diamond with width $S_o$ emerges. **c,** At $B_{||} = 220$ mT, even and odd Coulomb diamonds are $1e$ periodic and uniformly spaced, with $S_e = S_o$. A uniform Coulomb blockade spacing with transport through discrete resonances, energetically isolated from a higher-energy continuum, suggests the presence of a state at $E_0 = 0$.

and an odd Coulomb valley spacing

$$S_o = \eta^{-1}\left(E_C - 2E_0\right). \tag{3.23}$$

This behavior can be seen in the measurement in Figure 3.6b, where the state energy $E_0$ has been lowered in an applied magnetic field of $B_{||} = 100$ mT, and an odd Coulomb diamond with width $S_o$ has emerged, while the even diamond's width $S_e$ has shrunk commensurately.

Equations (3.22) and (3.23) imply that the energy of the subgap state can be easily inferred from the spacing according to

$$E_0 = \frac{\eta}{4}\left(S_e - S_o\right). \tag{3.24}$$

In particular, we find that $E_0 = 0$ implies $S_e = S_o$, and the Coulomb blockade pattern is uniform and 1e periodic, as shown in the energy diagram in Figure 3.5c and the corresponding measurement of Coulomb-diamonds for $B_{||} = 220$ mT in Figure 3.6c.

## 3.5 BIAS SPECTROSCOPY IN MAJORANA ISLANDS

In order to directly infer the energy of the quantum state, bias spectroscopy needs to be performed at fixed chemical potential. It is convenient to pick a gate voltage $V_G$ corresponding to a half-integer value of $N_G$, schematically shown in Figure 3.7. We will examine why this is useful in the following section.

Assuming that $N$ is even, the closest degeneracy point to $N_G = N + 1/2$ is between the $E_N$ and $E_{N+1}$. Their energy difference at this gate voltage is consequently

$$\begin{aligned} E_{N+1} - E_N = \frac{E_C}{2}\left(N + \frac{1}{2} - (N+1)\right)^2 + E_0 \\ - \frac{E_C}{2}\left(N + \frac{1}{2} - N\right)^2 \\ = E_0. \end{aligned} \tag{3.25}$$

As two tunneling processes are required to transfer a charge across the island, for $N_G = N + 1/2$ an onset of current $I$ at $V_{SD}$ is thus indicative of a state, or states, at $E = eV_{SD}/2$. In particular, a discrete state at $E_0 = 0$ with an excitation gap to a continuum should be characterized by an even spacing $S_e = S_o$ and a peak at $V_{SD} = 0$ at half-integer gate induced charge.

Away from half-integer values of gate induced charge $N_G$, a conductance peak at $V_{SD}$ cannot be interpreted as indicative of density of states at $E = \frac{eV_{SD}}{2}$ anymore.

## 3.6 DISCUSSION

Coulomb-blockade spectroscopy is a useful tool to probe the ground state energies of quantum dots and has been employed in the past to measure the discrete electronic spectrum of few-electron quantum dots [66, 73, 81–83], to explore the role and magnitude of deviations from the constant interaction model [82, 83], and to demonstrate spin-selection rules [73] when subsequent electrons are added.

In contrast to bias spectroscopy, that allows to probe excited states of the system, Coulomb-blockade spectroscopy probes the ground state of the system. Nonetheless, Coulomb-blockade spectroscopy

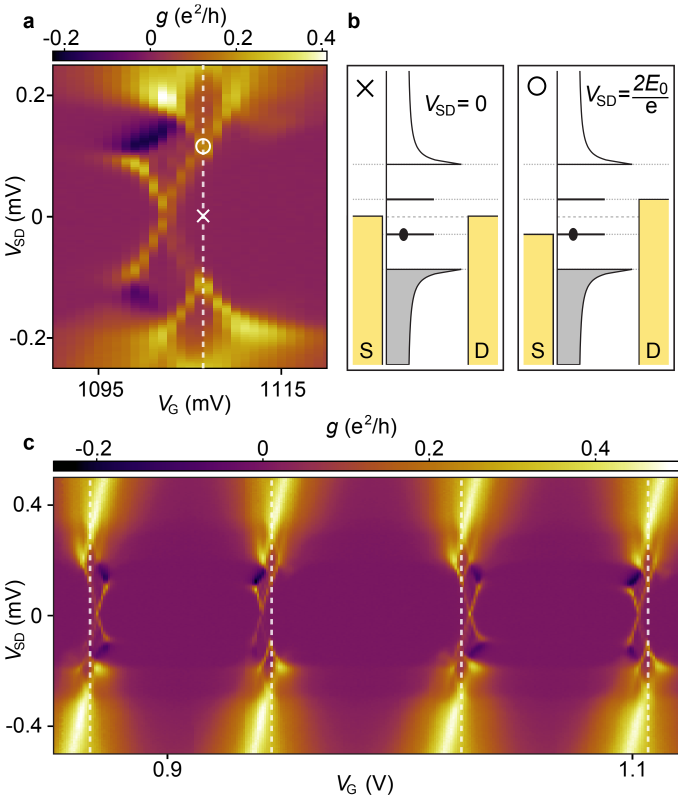

Figure 3.7: **Gate voltage and induced charge. a,** Differential conductance $g$ as a function of gate voltage $V_G$, and bias voltage $V_{SD}$ for an $L = 310$ nm Majorana island [72]. The gate voltage corresponding to half-integer gate-induced charge, $N_G = N + 1/2$, is indicated by a dashed white line. Energy level schematics at positions indicated by $\times$ and $\circ$ are shown in **b**. **b,** (left panel) Source and drain chemical potential are in the middle of the energy gap and no current can flow through the device. (right panel) At higher bias, the subgap state is in resonance with the chemical potentials of source and drain electrodes, leading to quasiparticle transport. **c,** Measurement of an even-odd Coulomb blockade pattern with gate voltages corresponding to $N_G = N + 1/2$ indicated.

of Andreev bound states has several advantages. In a Coulomb-blockaded geometry, bias spectroscopy is inherently difficult as it needs to be performed at a fixed chemical potential to accurately measure state energies. Especially when it is of interest to explore the magnetic field evolution of a quantum state, bias spectroscopy requires that there is no field-dependent common mode peak motion. Common mode peak motion can be caused, for example, by a nearby field-dependent charge trap that effectively gates the quantum dot as the magnetic field is varied, and shifts all peaks systematically in a single gate-direction, see for example Figure 3.8. As Coulomb

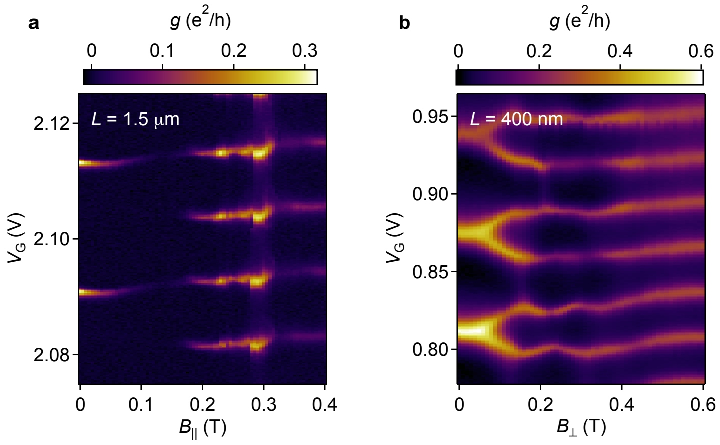

Figure 3.8: **Common mode peak motion. a,** for an $L = 1.5$ µm Majorana island in a parallel magnetic field $B_{||}$. **b,** for an $L = 400$ nm Majorana island in a perpendicular magnetic field $B_{\perp}$.

blockade peak spacings $S_{e,o}$ measure differences in chemical potential, Coulomb-blockade spectroscopy is insensitive to this effect. Using Coulomb-blockade spectroscopy, it is also possible to probe the spatial location of the quantum dot by examining capacitative coupling to different gates.

Another advantage that Coulomb-blockade spectroscopy has over bias spectroscopy is its ability to unambiguously measure negative bound state energies $E_0 < 0$. We define negative energies here as negative with respect to the BCS-condensate. This corresponds to a situation in which it is energetically more favorable for the superconductor-semiconductor hybrid system to have an odd number of quasiparticles. Inserting $E_0 < 0$ into Equation (3.24), we find $S_o > S_e$ and conclude that the odd diamond will be wider than the even diamond for negative state energies. This is shown for measurements taken at four magnetic fields, $B_{||} = 0, 300, 600, 700$ mT, in Figure 3.9. Here, the device is barely in the regime where $E_0 < E_C/2$ at $B = 0$, leading to a tiny odd Coulomb diamond. For increasing fields the odd diamond grows, until it is bigger than its adjacent even diamond at $B_{||} = 700$ mT, clearly indicating an energy $E_0 < 0$. This is in contrast to bias spectroscopy, where a negative state energy is indistinguishable from a positive state energy due to electron-hole symmetry.

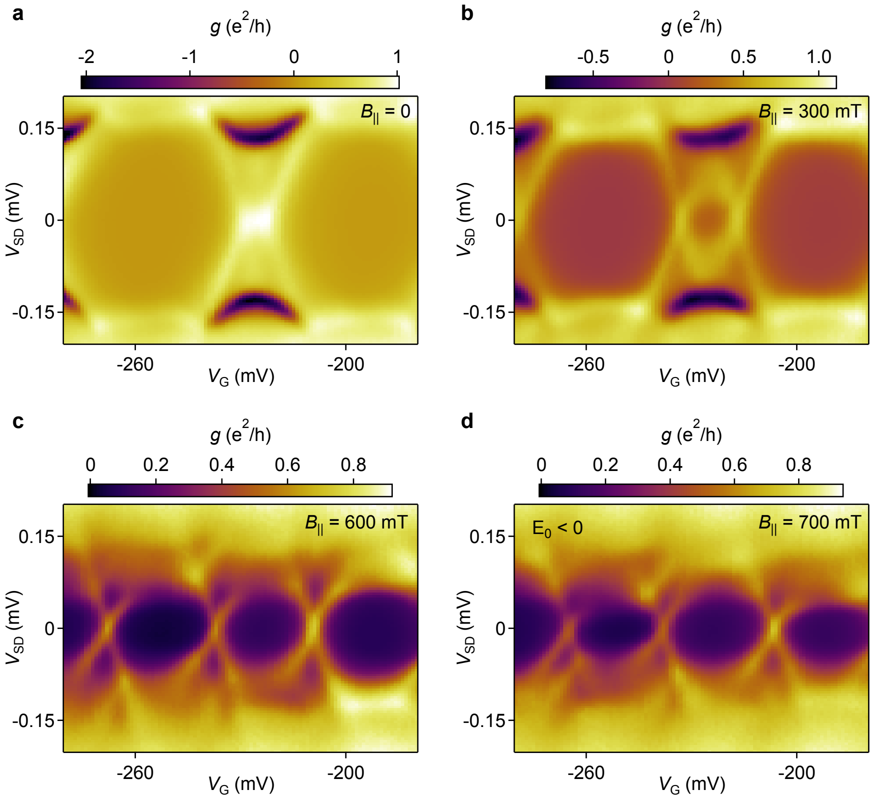

Figure 3.9: **Negative state energies.** Coulomb blockade patterns in an $L =$ 400 nm Majorana island. **a,** For $B_{||} = 0$ there is a strong even-odd parity effect, implying that $E_0$ is just below $E_C/2$, leading to an almost vanishing odd diamond. **b,** For $B_{||} = 300\,\mathrm{mT}$ the odd diamond has grown as $E_0$ is lowered by the Zeeman energy. **c,** Near-zero-energy state at $B_{||} = 600$ mT, shortly before the state energy $E_0$ changes sign. **d,** For $B_{||} = 700$ mT, the odd diamond has grown so that $S_o > S_e$. This is indicative of a state energy $E_0 < 0$ as the Majorana island is driven into the topological regime.

## 3.7 CONCLUSION

In Chapter 2 we have gained an understanding of the physics of Majorana modes, and in Chapter 3 we learned about their experimental signatures in Majorana islands. Advances in fabrication procedures only recently allowed for the epitaxial coupling of semiconductors and superconductors in nanowire geometries that made Majorana islands possible [84]. This has also been found to be a key ingredient towards obtaining the hard superconducting gaps [79, 85] required for topologically protected Majorana states. We will turn our attention towards the fabrication of Majorana islands in the next chapter.

# 4

# DEVICE FABRICATION

This chapter provides information on the nanofabrication procedures used to make Majorana island devices based on InAs nanowires with epitaxial Al shell. It summarizes the entire process, from chip blanks to a finished device, while giving an overview of nanowire selection criteria and other useful information for a succesful fab.

## 4.1 CHIP BLANKS

A chip blank is a pre-fabricated piece of wafer that already includes structures that are useful for further fabrication steps and can be fabricated in larger numbers easily. The chip blanks used in this thesis were fabricated from 4″ degenerately doped silicon wafers purchased from University Wafers. Wafer specifications are shown in Table 4.2. The blanks are based on a previous design [76], which was modified to account for changes in the process that was developed over the course of this thesis.

The lithographic patterns pre-fabricated on the chip blanks are shown in Figure 4.1a. They consist of three sets of alignment marks, in addition to lines and bondpads. The lines were originally patterned as meanders using UV-photolithography (parameters shown in Table 4.3) in order to increase their total resistance and make them useful as a filter. This, however, was deemed unnecessary in the better filtered QDev fridges. They were replaced by straight lines in later iterations of the design. Alignment marks consist of a large set used for rough alignment, patterned using UV-photolithography, a set of small alignment marks outside the write field area, and a 50 µm × 50 µm grid of small alignment marks in the write field area, that is used to determine the position of nanowires. The set of small alignment marks was patterned using electron beam lithography (EBL), in order to use it for lithography with $< 50$ nm precision.

A sample chip with lithographic contacts to a nanowire, bonded onto a chip carrier, is shown with a size reference in Figure 4.1b.

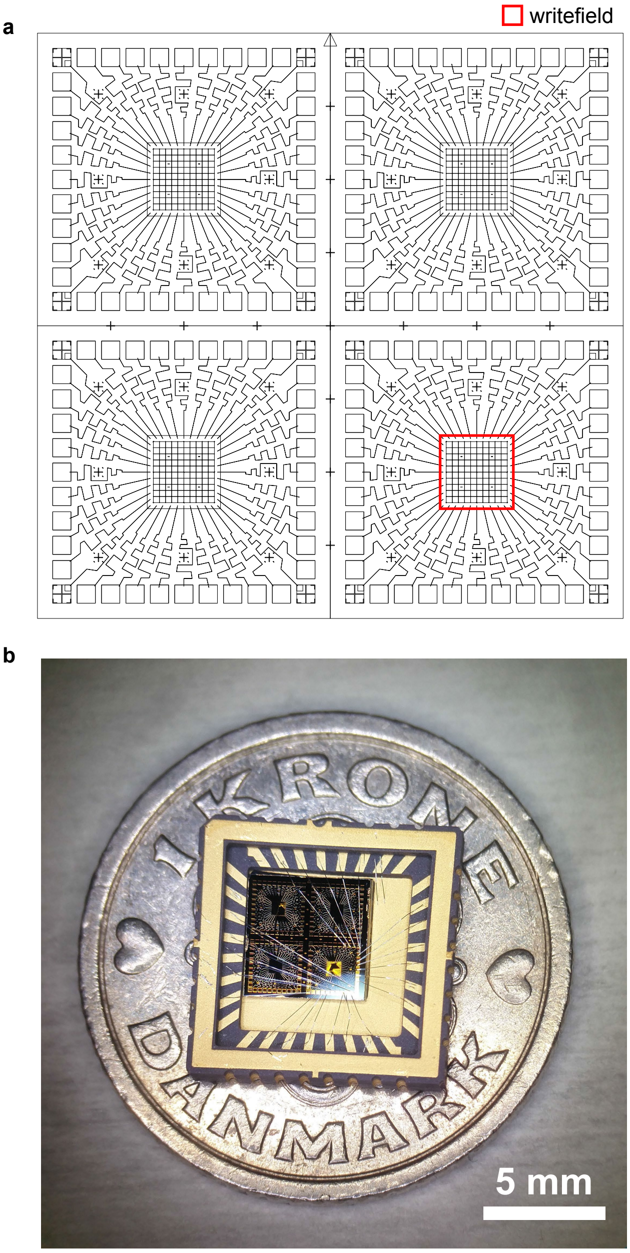

Figure 4.1: **Chip blanks and bonded sample. a,** CAD design for a chip blank showing four quadrants with 40 bond pads respectively. Each quadrant features a 600 µm × 600 µm write field for nanowire deposition and electron beam lithography steps in the center, indicated by a red rectangle for the bottom right quadrant. **b,** Magnification of a sample bonded to a ceramic chip carrier, with a Danish 1-kr piece for size reference. Electric contacts to nanowires have been lithographically patterned in the lower right quadrant. Bond wires connect the bond pads to the chip carrier.

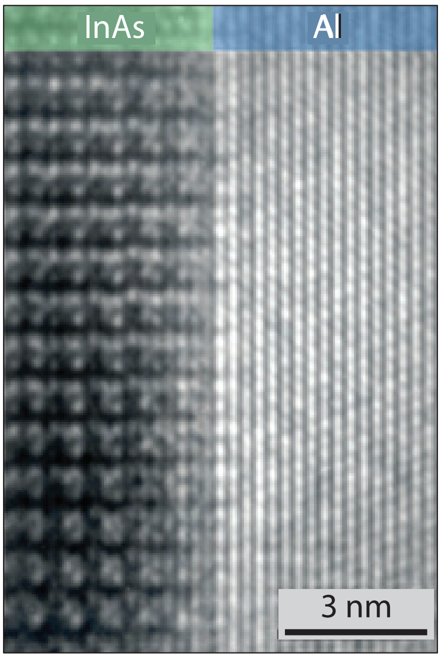

Figure 4.2: **Epitaxial interface between Al and InAs.** The TEM image shows the atomically precise interface between the semiconductor and the superconductor. Figure adapted from Krogstrup et al. [84].

## 4.2 NANOWIRE GROWTH

The InAs nanowires with epitaxial Al used for the work in this thesis were grown using molecular beam epitaxy (MBE) [84]. The growth consists of a two step process using the vapour-liquid-solid method. In the first step, the InAs core of the nanowire is grown at 420 °C with Au as a catalyst. Afterwards, the system is cooled down to -30 °C, whereupon the two-facet Al shell is grown *in situ* in the MBE chamber. As the nanowires remain in ultra-high vacuum during the growth process, the interface between Al and InAs is epitaxially matched, see Figure 4.2, leading to a good superconducting proximity effect and a hard induced gap in the semiconductor [79, 84].

At the end of the growth, the nanowires are standing upright with inter-wire distances of $\sim 2\ \mu m$, shown in the scanning electron micrograph in Figure 4.3. With typical growth regions of $1$ cm $\times$ $1$ cm, this leads to tens of millions of wires on a growth chip.

## 4.3 NANOWIRE DEPOSITION

After growth, the nanowires need to be transferred onto chip blanks in order to fabricate nanowire devices. The three favored methods for

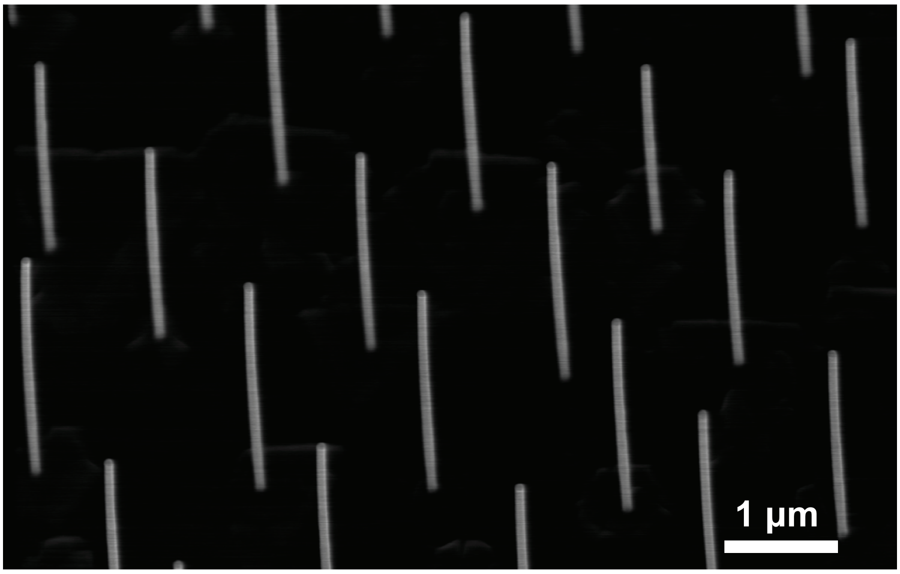

Figure 4.3: **Nanowire forest on a substrate.** The Au catalyst can be identified as a small droplet on the top of the nanowires. The lattice mismatch between Al and InAs induces a strain, causing the nanowires to bend towards the side with deposited Al half-shell, which is the same for all nanowires. Image courtesy of P. Krogstrup.

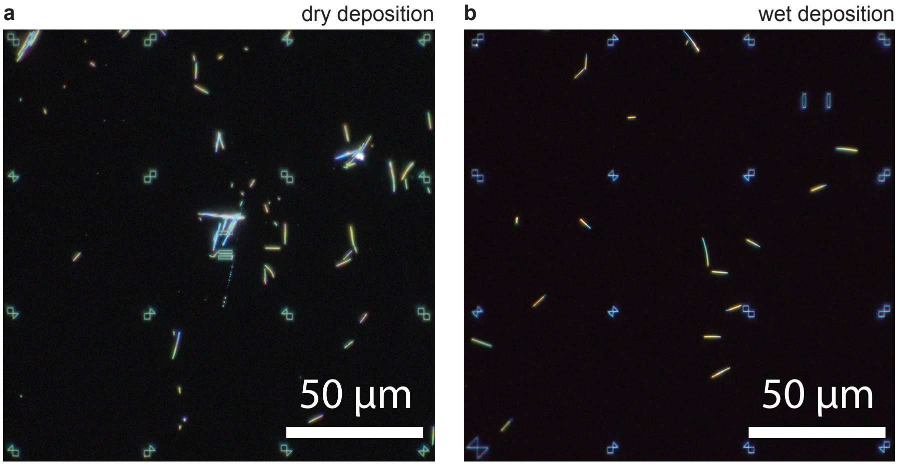

Figure 4.4: **Wet and dry deposition of nanowires. a,** Dry deposition tends to form aggregates of nanowire fragments that are unevenly distributed across the chip surface. **b,** Wet deposition leads to a more even distribution of nanowires, with little visible fragmentation.

nanowire transfer are dry deposition using cleanroom wipes, wet deposition, and single-wire micromanipulator aided dry deposition. For the purpose of the work presented in this thesis only dry deposition using cleanroom wipes and wet deposition techniques were used.

### 4.3.1 *Dry deposition*

In order to deposit nanowires on the chip blank, a new and pristine piece of cleanroom wipe is cut into a triangular shape using ordinary scissors. The section of the cleanroom wipe from which the triangular piece is taken should at this point not have been touched by gloves, or generally anything else except for other pieces of cleanroom wipes. The triangular piece can then be taken up using pointy tweezers in a way that leaves a tip of about 2-3 mm of loose cleanroom wipe extending from the end of the tweezers, with the tip of the tweezers pointing in the fiber direction of the cleanroom wipe. This piece of cleanroom wipe can then be dipped on a suitable area on the growth substrate. For the chip blanks used in this thesis, this was the center of one or more of the quadrants shown in Figure 4.1a. Afterwards it can be tapped or swiped multiple times on the area where the deposition has to take place, depending on the concentration of wires on the growth substrate. Usually, after three to four taps no more nanowires will stick to the chip and the cleanroom wipe should be disposed of. It is recommended to check the concentration of deposited wires after every piece of cleanroom wipe is discarded, in order to get a feeling for the required number of taps. This can vary widely, depending on the concentration, the types of wires, and the experimentalist's perception of how hard a tap should be. As not as many nanowires are dragged across the chip surface, taps are gentler than swipes, but it is more difficult to cover a large area with wires with this method. For the work in this thesis a combination of dragging and swiping was used, with multiple checks on an optical microscope in between to determine the concentration.

Due to the brutal nature of dry deposition, in which large quantities of nanowires are picked up, dragged across the substrate chip and then dragged across the chip blank, it leads to an aggregation of nanowires in large chunks of hundreds of wires, in addition to a large number of wire fragments on the chip surface. This can be clearly seen in the optical micrograph, shown in Figure 4.4a. The nanowire fragmentation can make drawing the lithographic pattern significantly more time consuming, as it is necessary to avoid shorts between adjacent lines due to bridging nanowires. This will almost certainly impede the scalability of multi-wire devices based on nanowires that were deposited this way. The chunks of nanowires can be problematic when spinning resist, which is why care should be taken to get the concentration of nanowires just right.

### 4.3.2 *Wet deposition*

For wet deposition, a small wafer piece of the growth substrate of around 2 mm × 2 mm is sonicated in a small beaker filled with methanol. It's recommended that the beaker should be as small as possible while still allowing for removal of the chip using tweezers. The chip should be less than 5 mm below the surface of the methanol in order to increase the concentration of nanowires in the solution. The exact time of sonication until a suitable concentration of nanowires is reached depends sensitively on the growth substrate, which is why no precise estimate can be given. For the work in this thesis, these times ranged between 10 s and 20 s. Afterwards small drops of methanol-nanowire solution were pipetted onto the chip surface and dried using a nitrogen gun. When successful, wet deposition can lead to a significantly more even distribution of nanowires, with few short wire fragments (Figure 4.4b). It is however more difficult to control the concentration this way, with many pipetting steps required to achieve an adequate concentration. For the presented work, the piece of growth substrate was disposed of after deposition, as it was unclear how damaging repeated sonication is to the nanowires. This makes wet deposition the most wasteful technique for nanowire deposition.

### 4.3.3 *Micromanipulator deposition*

Deposition using a micromanipulator was not done for the presented work, but its advantages and drawbacks are nonetheless discussed briefly. The method involves using a micron size tip with micrometer precision to pick single nanowires from a growth substrate under a microscope. The wires are picked up at the stem and stick to the tip due to van der Waals forces. Afterwards, the tip is brought into proximity with the chip blank until the nanowires stick to the surface. The orientation of the nanowire can be changed by using the tip to push it around the chip surface. Additionally, several nanowires can be placed in close proximity to each other by placing the second nanowire several microns away and then pushing it closer, which allows to place parallel nanowires with sub-micron inter-wire spacing. It is not recommended to place the second nanowire too close to the first one, as they tend to stick to each other when deposited this way.

This method has many advantages, as it allows to place nanowires in deterministic positions and orientations on the chip surface and makes multi-wire devices possible. Due to the selection of single wires it is also extremely conserving of nanowires. The process is, however, extremely time consuming, as it can take even an experienced user twelve hours to place five parallel nanowire pairs on the chip surface. Assuming no loss of wires during the deposition process and a substrate with one million wires, it would take an experienced user about 140 years of consecutive uninterrupted work to run out of wires from one growth substrate.

Another issue with micromanipulator aided deposition is that its effect on the structural integrity of the nanowires and the epitaxial interface between InAs and Al is currently unclear. While there have been no systematic studies on this, published results demonstrating consistently good proximity effect are at present still pending. Due to the cumbersome deposition process it is also not possible to post-select the best nanowires from a large pool of deposited nanowires, for example after an electron microscopy step.

### 4.3.4 *Comparison*

The main advantages of dry depositing nanowires using cleanroom wipes and wet deposition are that both methods are fast and produce reliable results. It is currently unclear to what extent any of the three deposition methods can induce cracks in the Al-shell or dislocations in the epitaxial matching between Al and InAs. The fabrication done for this thesis relied on a large number of nanowires that were transferred onto the chip blank, and were subsequently imaged. This made it possible to fabricate devices only on the most visually pristine nanowires that show no visible defects sustained during growth or depositon. Although no systematic study of this was undertaken, no difference in switching frequency or quality of observed proximity effect was observed between wet or dry-deposited wires. Micromanipulator deposition has, however, as this point not led to devices showing the same quality data as was obtained with the other two methods.

Micromanipulator aided deposition should be used when wires are scarce, a precise control of wire orientation is needed, or multi-wire devices are required. As it is not possible to post-select for untapered wires when depositing using the micromanipulator, the device fail-

| Method | Advantages | Disadvantages |
|---|---|---|
| Dry deposition | fast<br>post-selection of wires<br>proven to work | moderately wasteful<br>lots of debris<br>hard to control<br>non-deterministic |
| Wet deposition | moderately fast<br>post-selection of wires<br>even distribution<br>little debris<br>proven to work | very wasteful<br>hard to control<br>non-deterministic |
| Micro-manipulator | deterministic<br>close positioning<br>conserves wires | very slow<br>no post-selection<br>could damage wires |

Table 4.1: Different nanowire deposition methods.

ure rate should expected to be significantly higher compared to the other two methods (see section 4.4). This needs to be considered in the case of experiments requiring hard superconducting gaps to conserve Majorana state parities, such as fusion rules [27] and Majorana braiding [28,86,87].

The advantages and disadvantages of the different techniques are summarized in Table 4.1.

## 4.4 MAKING MAJORANA ISLANDS

The primary geometry that is analyzed in this thesis consists of an isolated Coulomb island in an InAs nanowire with epitaxial Al half shell contacted by normal (Ti/Au) leads, shown in Figure 3.2. The steps to fabricate these devices upon deposition of the nanowires will be outlined in the following sections.

### 4.4.1 *Wire localization and aluminum etch*

The nanowires are localized on the chip surface using an optical microscope and dark-field micrographs at a magnification corresponding to several cells of alignment marks are taken. For the chip blanks used in this thesis this could be done using six images that in total covered the whole area write field area of $600\,\mu\text{m} \times 600\,\mu\text{m}$. Afterwards, these micrographs were imported in a CAD program (DesignCAD) and stitched together and aligned to the chip design file using the alignment marks of the chip blanks, shown in Figure 4.5a. It is important to image the whole chip and not only the areas with suitable nanowires, to account for possible nanowire debris or nanowire aggregations in later lithography steps.

Using the CAD program, etch windows are placed on both ends of the nanowire. The etch can run up to 100 nm on both sides of the nanowire, leading to a smaller length of the exposed Al shell. This should be considered when placing the etch windows. With a diameter of $\sim$ 100 nm, the used nanowires are far below the diffraction limit of the optical microscope and no substructure can be identified. It is, however, possible to determine whether they are of sufficient length, and relatively straight. Due to the mismatch of lattice constants between InAs and Al, the Al induces a strain, causing the nanowires to bend towards the Al side, which makes it possible to identify the orientation of the Al shell from an optical image. This makes it more likely that the wire is lying on the chip surface in a way in which the two facets with the Al shell are perpendicular to the chip surface. A suitable nanowire is straight or slightly bent, and not immediately surrounded by other nanowires or nanowire debris. If a nanowire looks thicker on an optical micrograph, this suggests that two wires have stuck together, and they should be avoided. A nanowire that is bent towards one side is fine, although too large of a bend can result in a significantly reduced critical field in the case of long devices. Any S-shaped nanowires or nanowires with multiple bends should not be fabricated on, as this points towards damage sustained during transfer.

As only wet deposition and dry deposition techniques were used, there were usually a large number (30-50) of visually good nanowires on the chip surface after deposition. In order to increase the yield, etch windows were patterned using electron beam lithography on all of these nanowires. The details of the used resist stack based on polymethyl methacrylate (PMMA) are shown in Table 4.4.

After patterning of etch windows in the PMMA resist, the chip is developed in a solution of Methyl isobutyl ketone (MIBK) in Isopropyl alcohol (IPA) (ratio 1:3) for 90 s. Afterwards, the chip is briefly rinsed in IPA. In order to remove surplus resist that could interfere with the etch, this is followed by an oxygen plasma cleaning (ashing) step of 30 s in a converted microwave oven. Next, the Transene Al

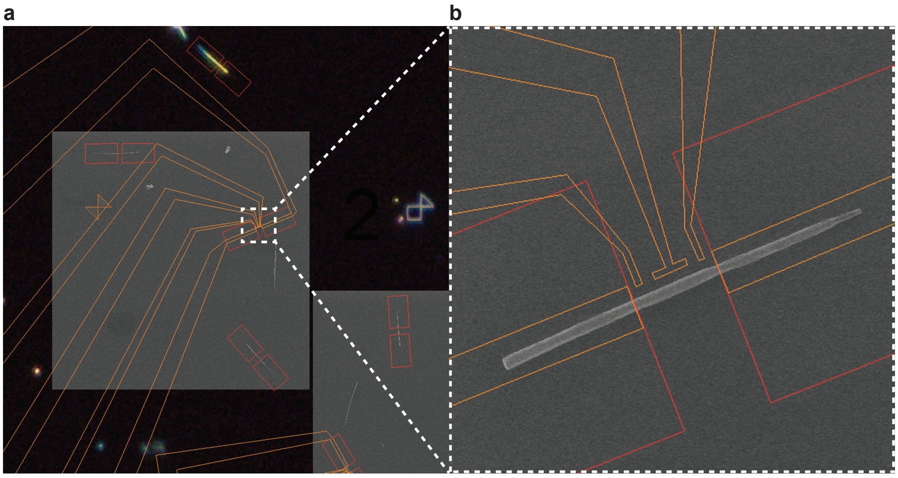

Figure 4.5: **CAD design of a Majorana island.** Lithographic patterns for contacts, two cutter-type gates, and one plunger gate outlined in orange, etch windows outlined in red. **a,** Overview with optical image (dark) in the background, and electron micrograph overlay (gray) aligned to the alignment marks in the foreground. **b,** Magnification of dashed area in **a**.

etchant D is filled into a small acid resistant beaker (with a lid) and pre-heated to a temperature of 55 °C in a water bath for at least 30 minutes. Two beakers of distilled water are prepared and placed in close proximity to the water bath. Shortly before the etch, one of the beakers is placed in the water bath next to the beaker with Al etchant. This makes it faster to dip the chip into the distilled water after it is removed from the etchant and leads to a more controlled etch. The chip is picked up using pointy, acid resistant tweezers and dipped into the etchant for 10 s. It is recommended to pick it up from one side, with one tip of the tweezers on the front and one of the backside of the chip. This prevents air bubbles to form between the tweezers and the chip, which could potentially ruin the time-sensitive etch. After 10 s of exposure to the Al etchant, the chip is removed and immediately dropped into the adjacent beaker with distilled water for at least 30 s. Subsequently, it is rinsed in the second beaker with distilled water and can be dropped into acetone to remove the resist.

The parameters of the etch are summarized in Table 4.5.

### 4.4.2 *Fabrication of Ohmic contacts and gates*

In order to fabricate Ohmic contacts and electrostatic gates, it is first necessary to determine the quality of the Al etch and the precise position of the nanowires. For this, the chip with etched nanowires is stripped of resist and imaged using a scanning electron microscope (SEM). When taking images it is important that for each nanowire at least one alignment mark is imaged in the same micrograph. The present chip blanks feature 50 μm separation between alignment marks on the write field, and nanowires with length $< 8\,\mu$m. Consequently, this translates to a required image size of 40 μm. As a precise ($< 60$ nm) positioning of gates is required, distortions of the SEM image need to be avoided as much as possible. This can be achieved by performing a thorough write field alignment and focus correction immediately prior to imaging. Translations of the micrograph up to several micrometer can be corrected for using the imaged alignment mark, but a correctly scaled undistorted image is absolutely necessary. In order to image a large number of nanowires in this way, an SEM with a CAD overlay feature and a piezo-controlled laser stage is strongly recommended. If possible, it is advisable to correct for the inevitable chip rotation before taking the image, to avoid having to do this in batch processing (slow) or the CAD program (slower) later.

Next, the images are imported into the CAD program and placed on the chip design. For the present work this was done using a python script that created an automatic DesignCAD macro to place the images with correct scaling at the correct position in the CAD file. This is possible because the SEM software supplies an additional file detailing the location and the image dimensions for each taken SEM image, another reason why CAD overlay is so useful.

Using the SEM and the corresponding write field alignment procedures, this typically results in an accuracy on the order of 100 nm for placing the images. Using the alignment marks in the pictures this can be reduced further down to the spatial resolution at which the images were taken, or the distortions inherent in the SEM image.

Untapered, straight, and visually defect free wires are identified and marked as candidates for fabrication. The percentage of useful wires ranged within 10-30 %. On a typical chip with about 30-50 deposited wires, this usually left around 5 very good wires. The threshold at which wires are unusable for measurements has not been systematically studied, but the presence of optically visible defects strongly suggests that the more sensitive electronic properties are affected by potential steps associated with lattice dislocations, defects or impurities. Despite the low statistics, it was observed that any optical defects correlated with switchy devices, or a bad proximity effect.

Tapered wires were avoided in the fabrication process at all costs in order to avoid changes in sub-band spacing and occupation.

As the etch has a tendency of running along the nanowire, the length of the exposed Al shell needs to be determined from the micrograph and the extent of the normal metal contacts can be varied accordingly. For the quantum dots in this thesis the bare InAs junctions were designed to be $\sim 70 - 100$ nm in length. Gates and contacts are drawn using the CAD software, as shown in Figure 4.5b.

The resist stack used for the second lithography step, that fabricates contacts and gates, is double layer PMMA A4. This creates only a minor undercut and allows for precise lithographic features and small gates. The pattern is written using the EBL machine and the resist is developed for 90 s in MIBK:IPA. In order to fabricate good Ohmic contacts, the surface oxide on the InAs wire was removed using either ion milling or sulfur passivation [88]. Ion milling resulted in significantly more stable (less switchy) devices, was faster and less prone to fabrication errors such as a damage to the Al half-shell, which is why it should be the preferred method. The chips were milled using using a Kaufman & Robinson KDC 40 4-CM DC Ion Source with an acceleration voltage of 120 V. The ion beam current density at the sample surface is estimated to be $0.5\ \mathrm{mA/cm^2}$. Milling times ranged from $85 - 110$ s. Sulfur passivation of the bare InAs nanowire surface consisted of dipping the chip in a solution of $(NH_4)_2S$ in de-ionized water with 0.15 M dissolved elemental sulphur at 40 °C for 20 min. In this case the milling step was omitted before the evaporation of the normal metal leads.

The evaporation step involved depositing a 5 nm sticking layer of titanium followed by the deposition of 70-100 nm of gold. The titanium wets the surface of the nanowire and prevents gold droplets to form by self assembly. Although titanium is a superconductor, the reverse proximity effect of the thick gold layer kills superconductivity in the thin titanium film completely.

The resist parameters and milling and evaporation parameters for making electrostatic gates and Ohmic contacts are summarized in Tables 4.6 and 4.7.

| | |
|---|---|
| Vendor | University Wafer |
| Wafer diameter [″] | 4 |
| Wafer thickness [µm] | $500 \pm 25$ |
| Resistivity [Ωcm] | $0.001 - 0.005$ |
| Dopant | Boron |
| Oxide thickness [nm] | 100 |

Table 4.2: Wafer specifications for the chip blanks.

| | |
|---|---|
| Resist | Shipley 1813 |
| Spin speed [rpm] | 4000 |
| Acceleration [rpm/s] | 1000 |
| Spin duration [s] | 45 |
| Baking time [s] | 120 |
| Baking temperature [°C] | 115 |

Table 4.3: Resist stack parameters of the UV-lithography step for making the chip blanks.

| | |
|---|---|
| Resist stack | PMMA A6 single layer |
| Spin speed [rpm] | 4000 |
| Acceleration [rpm/s] | 1000 |
| Spin duration [s] | 45 |
| Baking time [s] | 120 |
| Baking temperature [°C] | 185 |
| Beam current [pA] | 500 |
| Dose [$\mu C/cm^2$] | 1500 |
| Developer | MIBK:IPA 1:3 |

Table 4.4: Resist parameters for making the etch windows.

| | | |
|---|---|---|
| Etchant | Al Etchant D | |
| Vendor | Transene | |
| Composition [Wt %] | Sodium-M-Nitrobenzene Sulfonate | 5-10 |
| | Phosphoric Acid | 55-65 |
| | Acetic Acid | 1-5 |
| | Distilled Water | 20-39 |
| Temperature [°C] | 55 | |
| Etching time [s] | 10 | |
| Etch-Stop | Distilled Water | |

Table 4.5: Parameters of the Al etch.

| | |
|---|---|
| Resist stack | PMMA A4 double layer |
| Spin speed [rpm] | 4000 |
| Acceleration [rpm/s] | 1000 |
| Spin duration [s] | 45 |
| Baking time [s] | 120 |
| Baking temperature [°C] | 185 |
| Beam current [pA] | 500 |
| Dose [µC/cm$^2$] | 1050-1200 |
| Developer | MIBK:IPA 1:3 |

Table 4.6: Resist parameters for the electrostatic gates and Ohmic contacts.

| | |
|---|---|
| Ion source | Kaufman & Robinson<br>KDC 40 4-CM DC |
| Acceleration voltage [V] | 120 |
| Ion beam current density [mA/cm$^2$] | 0.5 |
| Milling time [s] | $85-110$ |
| Deposited metals | Ti/Au |
| Thickness [nm] | $5/70-100$ |

Table 4.7: Milling and evaporation parameters for the electrostatic gates and Ohmic contacts.

# Part II

# QUASIPARTICLE DYNAMICS I

# 5

# PARITY LIFETIME OF BOUND STATES IN A PROXIMITIZED SEMICONDUCTOR NANOWIRE

---

This chapter is published as:

Parity lifetime of bound states
in a proximitized semiconductor nanowire

A. P. Higginbotham[*], S. M. Albrecht[*], G. Kiršanskas, W. Chang,
F. Kuemmeth, P. Krogstrup, T. S. Jespersen, J. Nygård, K. Flensberg,
and C. M. Marcus

*Nature Physics* **11**, 1017–1021 (2015)

It presents the measurement of an even-odd parity effect in InAs-Al nanowire hybrid quantum dots. All devices were fabricated by Sven Marian Albrecht based on nanowires grown by Peter Krogstrup. Measurements and data analysis were done by Sven Marian Albrecht and Andrew Higginbotham under the supervision of Charles Marcus. The theoretical models were developed by Gediminas Kiršanskas, Karsten Flensberg and Andrew Higginbotham. The nanowire materials were developed by Peter Krogstrup, Thomas Jespersen and Jesper Nygård. Willy Chang, Thomas Jespersen, Ferdinand Kuemmeth and Jesper Nygård contributed to interpreting the data and gave valuable input. The manuscript was written by Sven Marian Albrecht and Andrew Higginbotham.

---

[*] These authors contributed equally to this work.

## 5.1 INTRODUCTION

Quasiparticle excitations can compromise the performance of superconducting devices, causing high frequency dissipation, decoherence in Josephson qubits [89–94], and braiding errors in proposed Majorana-based topological quantum computers [24, 95, 96]. Quasiparticle dynamics have been studied in detail in metallic superconductors [97–101] but remain relatively unexplored in semiconductor-superconductor structures, which are now being intensely pursued in the context of topological superconductivity. To this end, we introduce a new physical system comprising a gate-confined semiconductor nanowire with an epitaxially grown superconductor layer, yielding an isolated, proximitized nanowire segment. We identify bound states in the semiconductor via bias spectroscopy, determine the characteristic temperatures and magnetic fields for quasiparticle excitations, and extract a parity lifetime (poisoning time) of the bound state in the semiconductor exceeding 10 ms.

## 5.2 DEVICE GEOMETRY

Semiconductor-superconductor hybrids have been investigated for many years [26, 102–105], but have received renewed interest as platforms for emergent topological superconductors with Majorana end modes. Such modes are expected to show nonabelian statistics, allowing, in principle, topological encoding of quantum information [37, 38, 106] among other interesting effects [107, 108].

Transport experiments on semiconductor nanowires proximitized by a grounded superconductor have recently revealed characteristic signatures of Majorana modes [39, 40]. Semiconductor quantum dots with superconducting leads have also been explored experimentally [71, 109–111], and have been proposed as a basis for Majorana chains [112–114]. Here, we expand these geometries by creating an isolated semiconductor-superconductor hybrid quantum dot (HQD) connected to normal leads. The device forms the basis of an isolated, mesoscopic Majorana system with protected total parity [115, 116].

The measured device consists of a hexagonal InAs nanowire with epitaxial superconducting Al on two facets [79,84], and Au ohmic contacts (Figs. 5.1a,b), forming a normal metal-superconductor-normal metal (NSN) device. Four devices showing similar behavior have been measured. Differential conductance, $g$, was measured in a di-

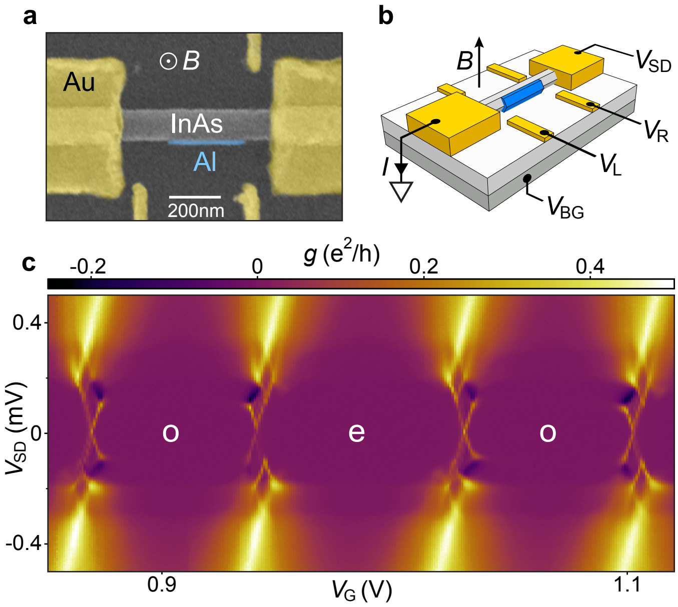

Figure 5.1: **Nanowire-based hybrid quantum dot.** **a**, Scanning electron micrograph of the reported device, consisting of an InAs nanowire (gray) with segment of epitaxial Al on two facets (blue) and Ti/Au contacts and side gates (yellow) on a doped silicon substrate. **b**, Device schematic and measurement setup, showing orientation of magnetic field, $B$. **c**, Differential conductance, $g$, as a function of effective gate voltage, $V_G$, and source-drain voltage, $V_{SD}$, at $B = 0$. Even (e) and odd (o) occupied Coulomb valleys labeled.

lution refrigerator ($T \sim 50$ mK) using standard lock-in techniques. Local side gates and a global back gate were adjusted to form an Al-InAs HQD in the Coulomb blockade regime. The lower right gate, $V_R$, was used to tune the occupation of the dot, with a linear compensation from the lower left gate, $V_L$, to keep tunneling to the leads symmetric. We parameterize this with a single effective gate voltage, $V_G$ (see Supplement).

## 5.3 PARITY EFFECT

Differential conductance as a function of $V_G$ and source-drain bias, $V_{SD}$, reveals a series of Coulomb diamonds, corresponding to incremental single-charge states of the HQD (Figure 5.1c). While conductance features at high bias are essentially identical in each diamond, at low bias, $V_{SD} < 0.2$ mV, a repeating even-odd pattern of left- and right-facing conductance features is observed. This results in an even-odd alternation of Coulomb blockade peak spacings at zero bias, similar to metallic superconductors [117, 118]. However, the parity-dependent reversing pattern of subgap features at nonzero bias has not been reported before, to our knowledge. The repeating even-odd pattern indicates that a parity-sensitive bound state is being repeatedly filled and emptied as electrons are added to the HQD.

Measured charging energy, $E_C = 1.1$ meV, and superconducting gap, $\Delta = 180$ μeV, satisfy the condition ($\Delta < E_C$) for single electron charging [46, 119]. Differential conductance at low bias occurs in a series of narrow features symmetric about zero bias, suggesting transport through a bound state, with negative differential conductance (NDC) observed at the border of odd diamonds. NDC arises from slow quasiparticle escape, similar to current-blocking seen in metallic superconducting islands in the opposite regime, $\Delta > E_C$ [120, 121].

## 5.4 MODEL

We present a simple model of transport through a single bound state in the InAs plus a Bardeen-Cooper-Schrieffer (BCS) continuum in the Al. The model makes several simplifying assumptions: a fixed-energy bound state, motivated by the repetitive pattern observed in the Coulomb diamonds, and symmetric coupling of both the bound state and continuum to the leads, motivated by the observed symmetry in $V_{SD}$ of the Coulomb diamonds. Transition rates were calculated from Fermi's golden rule and a steady-state Pauli master equation was solved for state occupancies. Conductance was then calculated from occupancies and transition rates (see Supplement).

Measured and model conductances are compared in Figs. 5.2a,b. The coupling of the bound state to each lead, noting the near-symmetry of the diamonds, was estimated to be $\Gamma_0 = 0.5$ GHz, based on zero-bias conductance (Figure 5.2d). The energy of the state, $E_0 = 58$ μeV at zero magnetic field, was measured using finite bias spectroscopy (Figure 5.2e). The normal-state conductance from each lead to the continuum, $g_{Al} = 0.15\ e^2/h$, was estimated by comparing Coulomb blockaded transport features in the high bias regime ($V_{SD} = 0.4$ mV). The superconducting gap, $\Delta = 180$ μeV, was found from the onset of NDC at $eV_{SD} = \Delta - E_0$ (Figure 5.2f). While the rate model shows good agreement with experimental data, some features are not captured, including broadening at high bias, with greater broadening correlated with weaker NDC, and peak-to-peak fluctu-

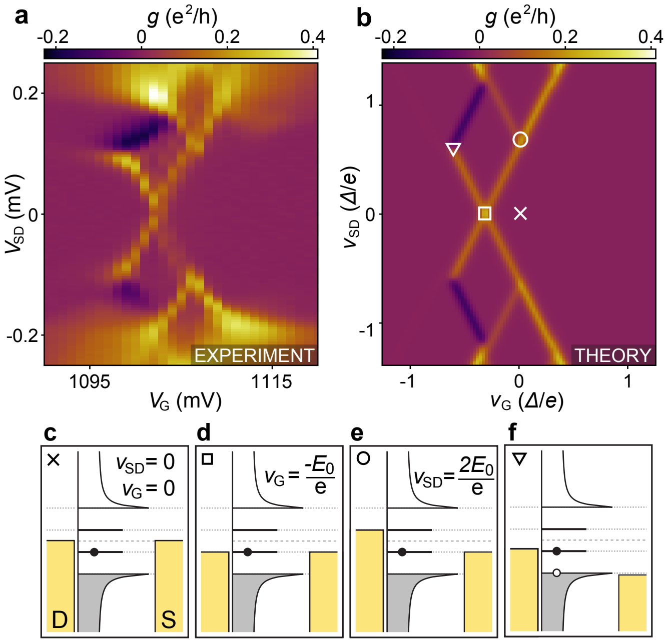

Figure 5.2: **Subgap bias spectroscopy, experiment and model. a**, Experimental differential conductance, $g$, as a function of gate voltage $V_\mathrm{G}$ and source-drain $V_\mathrm{SD}$, shows characteristic pattern including negative differential conductivity (NDC). **b**, Transport model of **a**. $v_\mathrm{G} = \alpha V_\mathrm{G}$ up to an offset, where $\alpha$ is the gate lever arm. Axis units are $\Delta/e = 180\ \mu\mathrm{V}$, where $\Delta$ is the superconducting gap. See text for model parameters. **c**, Source and drain (gold) chemical potentials align with the middle of the gap in the HQD density of states. No transport occurs due to the presence of superconductivity. **d**, Discrete state in resonance with the leads at zero bias. Transport occurs through single quasiparticle states. **e**, Discrete state in resonance with the leads at high bias. Transport occurs through single and double (particle-hole) quasiparticle states. **f**, Discrete state and BCS continuum in the bias window. Transport is blocked when a quasiparticle is in the continuum, resulting in NDC.

ations in the slope of the NDC feature. These features may be related to heating or cotunneling, not accounted for by the model.

The observation of negative differential conductance places a bound on the relaxation rate of a single quasiparticle in the HQD from the continuum (in the Al) to the bound state (in the InAs nanowire). NDC arises when an electron tunnels into the weakly coupled BCS continuum, blockading transport until it exits via the lead. The blocking condition is shown for a hole-like excitation in Figure 5.2f. Unblocking occurs when the quasiparticle relaxes into the bound state, followed by a fast escape to the leads. NDC thus indi-

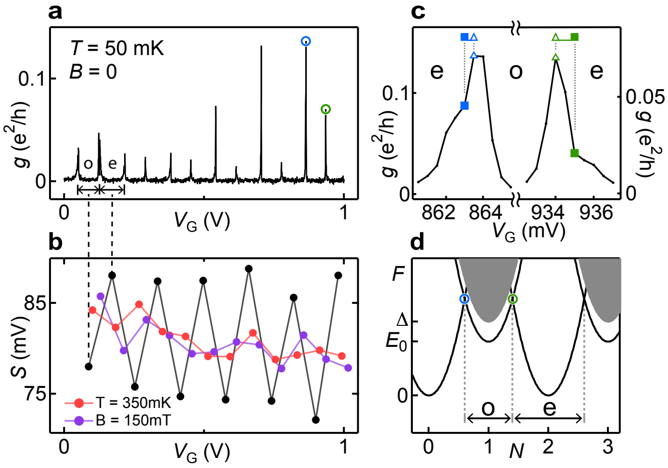

Figure 5.3: **Even-odd Coulomb peak spacings.** **a**, Measured zero-bias conductance, $g$, versus gate voltage, $V_{\mathrm{G}}$, at temperature $T \sim 50$ mK, and magnetic field $B = 0$. **b**, Peak spacing, $S$, versus gate voltage. Black points show spacings from **a** calculated using the peak centroid (first moment), red points $T = 350$ mK and $B = 0$, purple points $B = 150$ mT and $T \sim 50$ mK. **c**, Right-most peaks in **a**. Peak maxima (△) and centroids (■) are marked. **d**, Free energy, $F$, at $T = 0$ versus gate-induced charge, $N$, for different HQD occupations, where $N = CV_{\mathrm{G}}/e$ up to an offset and $C$ is the gate capacitance. Parabola intersection points are indicated by circles, corresponding to Coulomb peaks. BCS continuum (shaded), shown for odd occupancy. Odd Coulomb diamonds carry an energy offset $E_0$ for quasiparticle occupation of the sub gap state, resulting in a difference in spacing for even and odd diamonds.

cates a long quasiparticle relaxation time, $\tau_{\mathrm{qp}}$, from the continuum to the bound state. Using independently determined parameters, the observed NDC is only compatible with the model when $\tau_{\mathrm{qp}} > 0.1$ μs (see Supplement), which is used below to constrain the poisoning time for the bound state.

Turning our attention to the even-odd structure at zero-bias, we observed consistent large-small peak spacings (Figs. 5.3(a,b)), associating larger spacings with even occupation, as expected theoretically [46, 119]. Parity reversals were observed on the timescale of hours, similar to observations in metallic devices [101]. Peak spacing alternation disappears at higher magnetic fields, $B$, consistent with the superconducting-to-normal transition, and also disappears at elevated temperature, $T > 0.4$ K, significantly below the superconducting critical temperature, $T_c \sim 1$ K. The temperature dependence is similar to metallic structures [117, 118], and can be understood as the

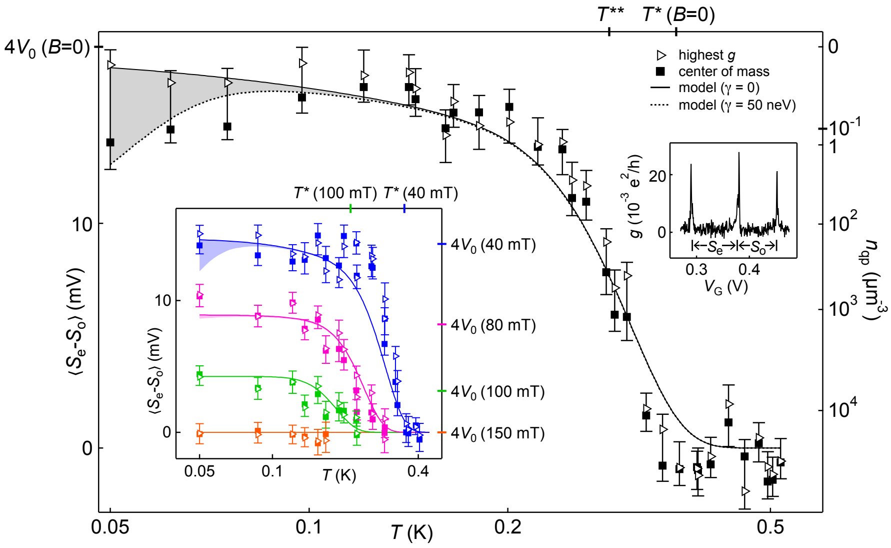

Figure 5.4: **Temperature and magnetic field dependence of the even-odd peak spacings.** Average even-odd spacing difference, $\langle S_e - S_o \rangle$, versus temperature, $T$. Spacing between peak maxima (triangle) and centroids (square) are shown, with error bars from standard deviation of peak maxima. Spacing expected from lower Zeeman-split bound state, $4V_0(B) = 4E_0(B)/(\alpha e)$ indicated. Quasiparticle activation temperature, $T^*$, and crossover temperature, $T^{**}$, indicated on top axis. Right axis shows calculated aluminum quasiparticle density, $n_{qp}$ (see text). Solid curve is Equation (5.1) with a HQD density of states measured from Figure 5.2 ($\Delta = 180$ μeV, $E_0 = 58$ μeV, $\alpha = 0.013$), and the fitted aluminum volume, $V_{Al} = 7.4 \times 10^4$ nm$^3$. Dotted curve includes a discrete state broadening, $\gamma = 50$ neV, fit to the centroid data. *Left inset:* Same as main, but at $B = 40, 80, 100, 150$ mT, from top to bottom and $4V_0$ appearing on the right-hand axis. Curves are fit to two shared parameters: g-factor, $g = 6$, and superconducting critical field, $B_c = 120$ mT, with other parameters fixed from main figure. *Right inset:* Representative Coulomb peaks showing even ($S_e$) and odd ($S_o$) spacings.

result of thermal activation of quasiparticles within the HQD with fixed total charge.

As seen in Figure 5.3c, individual Coulomb peaks are asymmetric in shape, with their centroids (first moments) on the even sides of the peak maxima. The asymmetric shape is most pronounced at low temperature, $T < 0.15$ K, and decreases with increasing magnetic field. The degree of asymmetry is not predicted by the rate model, even taking into account the known small asymmetry due to spin degeneracy [122]. In the analysis below, we consider peak positions defined both by peak maxima and centroids.

A model of even-odd Coulomb peak spacing that includes thermal quasiparticle excitations follows earlier treatments [46, 117, 118], including a discrete subgap state as well as the BCS continuum [118] (Figure 5.3d). Even-odd peak spacing difference, $S_\mathrm{e} - S_\mathrm{o}$, depends on the difference of free energies,

$$S_\mathrm{e} - S_\mathrm{o} = \frac{4}{\alpha e}\left(F_\mathrm{o} - F_\mathrm{e}\right), \tag{5.1}$$

where $\alpha$ is the (dimensionless) gate lever arm. The free energy difference, written in terms of the ratio of partition functions,

$$F_\mathrm{o} - F_\mathrm{e} = -k_\mathrm{B}T\ln\left(\frac{Z_\mathrm{o}}{Z_\mathrm{e}}\right), \tag{5.2}$$

depends on $D(E)$, the density of states of the HQD,

$$\frac{Z_\mathrm{o}}{Z_\mathrm{e}} = \int_0^\infty \mathrm{d}E\ D(E)\ln\coth[E/(2k_\mathrm{B}T)], \tag{5.3}$$

where $D(E)$ consists of one subgap state and the continuum. For $\Delta \gg k_\mathrm{B}T$, this can be written

$$F_\mathrm{o} - F_\mathrm{e} \approx -k_\mathrm{B}T\ln(N_\mathrm{eff}e^{-\Delta/k_\mathrm{B}T} + 2e^{-E_0/k_\mathrm{B}T}), \tag{5.4}$$

where $N_\mathrm{eff} = \rho_\mathrm{Al}V_\mathrm{Al}\sqrt{2\pi k_\mathrm{B}T\Delta}$ is the effective number of continuum states for Al with volume $V_\mathrm{Al}$ and electron density of states $\rho_\mathrm{Al}$ [117, 118].

Within the thermodynamic model, one can identify a characteristic temperature, $T^* \sim \Delta/[k_\mathrm{B}\ln(N_\mathrm{eff})]$, less than the gap and independent of $E_0$, above which even-odd peak spacing alternation is expected to disappear. A second (lower) characteristic temperature, $T^{**} \sim (\Delta - E_0)/[k_\mathrm{B}\ln(N_\mathrm{eff}/2)]$, is where the even-odd alternation is affected by the bound state, leading to saturation at low temperature [117, 118]. For a zero-energy ($E_0 = 0$) bound state - the case for Majorana modes - these characteristic temperatures coincide and even-odd structure vanishes, as pointed out in Ref. [115]. For $E_0 = \Delta$ the saturation temperature vanishes, $T^{**} = 0$, and the metallic result is recovered [117, 118].

Experimentally, the average even-odd peak spacing difference, $\langle S_\mathrm{e} - S_\mathrm{o}\rangle$, was determined by averaging over a set of 24 consecutive Coulomb peak spacings, including those shown in Figure 5.3. Figure 5.4 shows even-odd peak spacing difference appearing abruptly at $T_\mathrm{onset} \sim 0.4$ K, and saturating at $T_\mathrm{sat} \sim 0.2$ K, with a saturation amplitude near the value expected from the measured bound state energy,

$4V_0 = 4E_0/(\alpha e)$. Figure 5.4 shows good agreement between experiment and the model, Equation (5.1), using a density of states determined independently from data in Figure 5.2, with $V = 7.4 \times 10^4$ nm$^3$ as a fit parameter, consistent with the micrograph (Figure 5.1a), and $\rho_{\mathrm{Al}} = 23$ eV$^{-1}$nm$^{-3}$ [101].

The asymmetric peak shape amounts to larger peak tails on the even valley side, causing the centroids to be more regularly spaced than the maxima. This is evident in Figure 5.4, where the centroid method shows a decreasing peak spacing difference at low temperature, while with the maximum method the spacing remains flat. The thermal model of $S_e - S_o$ can also show a decrease at low temperature if broadening of the bound state is included. We do not understand at present if this effect explains the difference between centroids and maxima, however, it is worth noting that the fit gives a broadening $\gamma = 50$ neV, reasonably close to the value estimated from the lead couplings, $(h\Gamma_0)^2/\Delta = 20$ neV.

Applied magnetic field (direction shown in Figure 5.1b) reduces the characteristic temperatures $T_{\mathrm{onset}}$, $T_{\mathrm{sat}}$, and saturation amplitudes. Field dependence is modeled by including Zeeman splitting of the bound state and orbital reduction of the gap. The fit g-factor, $g = 6$, lies within the typical range for InAs nanowires [70, 123], supporting our interpretation that the bound state resides in the InAs.

Agreement with the thermodynamic model suggests that ensemble averages of even-odd spacing, $S_e - S_o$, provide a measure of the equilibrium quasiparticle density, $n_{\mathrm{qp}}$. Figure 5.4 (right axis) gives the value $n_{\mathrm{qp}}(T) = V_{\mathrm{Al}}^{-1} N_{\mathrm{eff}}^2 e^{-2\Delta/k_B T}$, an expression valid for large charging energy [124] (see Supplemental Material, Sec. 5). Below $T_{\mathrm{sat}} \sim 0.2$ K, even-odd spacing saturates at the bound-state value $4V_0$, making it difficult to infer a quasiparticle density in this low-temperature range. Instead, we conservatively take $n_{\mathrm{qp}}(T_{\mathrm{sat}}) \sim 0.1$ µm$^{-3}$ as an upper bound for the quasiparticle density at low temperature. This value is within the range from the recent literature, $0.03 - 30$ µm$^{-3}$ [91–94, 100]. Because the volume of Al is small, the upper bound on the number of quasiparticles, $n_{\mathrm{qp}} V_{\mathrm{Al}} < 10^{-5}$, is, correspondingly, quite small.

## 5.5 CONCLUSION

Finally, we determine a lower bound on the poisoning time, $\tau_p$, of the bound state. The physical mechanism for this poisoning is relaxation of a quasiparticle into the InAs from the Al, which preserves the overall parity of the HQD but changes the parity of the bound state. This process is expected to set the fundamental limit on parity lifetime [24]. The poisoning rate, $1/\tau_{\mathrm{p}}$, is given by the product of the relaxation rate of a single quasiparticle from the Al, $1/\tau_{\mathrm{qp}}$, and the number of quasiparticles in the Al [24], which, from above, is bounded by $n_{\mathrm{qp}} V_{\mathrm{Al}} < 10^{-5}$. Quantitative analysis of the strength of negative differential conductance at finite bias - which vanishes for fast quasiparticle relaxation - provides a lower bound on the quasiparticle relaxation time, $\tau_{\mathrm{qp}} > 0.1\ \mu\mathrm{s}$ (Supplement Sec. 2). Together, these values give a conservative lower bound on the poisoning time of the bound state, $\tau_{\mathrm{p}} = \tau_{\mathrm{qp}}/(n_{\mathrm{qp}} V_{\mathrm{Al}}) > 10\ \mathrm{ms}$.

Quasiparticle density depends sensitively on device geometry, filtering, and shielding, resulting in a wide range of experimental values ($0.03 - 30\ \mu\mathrm{m}^{-3}$) [91–94], and thus poisoning times. We note that recent work in transmon qubits [100] found $n_{\mathrm{qp}} = 0.04\ \mu\mathrm{m}^{-3}$, corresponding to state-poisoning times well above 10 ms. We also note that the Coulomb blockade geometry effectively enforces quasiparticles from the Al shell to be created only in pairs, which is different from non-charging device geometries.

Based on previous work, $\tau_{\mathrm{qp}}$, hence $\tau_{\mathrm{p}}$, is expected to depend weakly on the bound-state energy for low-energy bound states [98,125,126], including zero-energy Majorana modes with $E_0 = 0$. The long poisoning time found here, $\tau_{\mathrm{p}} > 10\ \mathrm{ms}$, is auspicious for application of this system to topological quantum computing, suggesting that a large number of braiding operations of Majorana modes could be performed before the parity of the bound state is poisoned by the proximitizing Al. Future work will examine Majorana modes in this geometry.

## 5.6 METHODS

### 5.6.1 *Sample preparation*

InAs nanowires were grown without stacking faults in the [001] direction with wurzite crystal structure with Al epitaxially matched to [111] on two of the six $\{1\bar{1}00\}$ sidefacets [79,84]. They were then deposited randomly onto a doped silicon substrate with 100 nm of thermal oxide. Electron-beam lithographically patterned wet etch of the epitaxial Al shell (Transene Al Etchant D, 55 C, 10 s) resulted in a sub-micron Al segment (310 nm, Figure 5.1a). Ti/Au (5/100 nm) ohmic contacts were deposited on the ends following *in situ* Ar milling (1 mTorr, 300 V, 75 s), with side gates deposited in the same step. For the device presented here, the end of the upper left gate broke off during processing. However, the device could be tuned well without it.

### 5.6.2 *Master equations*

The master equations (used for Figure 5.2b) consider states with fixed total parity, composed of the combined parity of quasiparticles in the thermalized continuum and the 0, 1, or 2 quasiparticles in the bound state (see Supplement).

### 5.6.3 *Free energy model*

Even and odd partition functions in Equation (5.2), $F_\mathrm{o} - F_\mathrm{e} = -k_\mathrm{B}T\ln(Z_\mathrm{o}/Z_\mathrm{e})$, can be written as sums of Boltzmann factors over respectively odd and even occupancies of the isolated island. For even-occupancy,

$$Z_\mathrm{e} = 1 + \sum_{i\neq j} e^{-E_i/k_\mathrm{B}T} e^{-E_j/k_\mathrm{B}T} + \ldots, \tag{5.5}$$

where the first term stands for zero quasiparticles, the second for two (at energies $E_i$ and $E_j$), and additional terms for four, six, etc. $Z_\mathrm{o}$ similarly runs over odd occupied states. Rewriting these sums as integrals over positive energies yields

$$F_\mathrm{o} - F_\mathrm{e} = -k_\mathrm{B}T \ln\tanh \int_0^\infty \mathrm{d}E\; D(E) \ln\coth(E/2k_\mathrm{B}T), \tag{5.6}$$

where $D(E)$ is the density of states of the HQD,

$$D(E) = \rho_\mathrm{BCS}(E) + \frac{1}{2}\rho_0^+(E) + \frac{1}{2}\rho_0^-(E). \tag{5.7}$$

We take $\rho_\mathrm{BCS}(E)$ to be a standard BCS density of states,

$$\rho_\mathrm{BCS}(E) = \frac{\rho_\mathrm{Al} V E}{\sqrt{E^2 - \Delta(B)^2}}\theta(E-\Delta) \tag{5.8}$$

($\theta$ is the step function), and $\rho_0$ to be a pair of Lorentzian-broadened spinful levels symmetric about zero,

$$\rho_0^\pm(E) = \frac{\gamma/2\pi}{(E-E_0^\pm)^2 + (\gamma/2)^2} + \frac{\gamma/2\pi}{(E+E_0^\pm)^2 + (\gamma/2)^2}. \tag{5.9}$$

Zeeman splitting of the bound state and pair-breaking by the external magnetic field are modeled with the equations

$$E_0^{\pm}(B) = \frac{\Delta(B)}{\Delta}E_0 \pm \frac{1}{2}g\mu_B B, \tag{5.10}$$

$$\Delta(B) = \Delta\sqrt{1-\left(\frac{B}{B_c}\right)^2}, \tag{5.11}$$

where $E_0$ is the zero-field state energy and $\Delta$ is the zero field superconducting gap. In the event that a bound state goes above the continuum, $E_s^+ > \Delta(B)$, we no longer include the state in the free energy. Equation (5.6) was integrated numerically to obtain theory curves in Figure 5.4.

Equations (5.10) and (5.11) are reasonable provided the lower spin-split state remains at positive energy, $E_0^- > 0$. For sufficiently large $B_c$, the bound state will reach zero energy, resulting in topological superconductivity and Majorana modes, the subject of future work.

# Part III

# EXPONENTIAL PROTECTION

# 6

# EXPONENTIAL PROTECTION OF ZERO MODES IN MAJORANA ISLANDS

This chapter is published as:

Exponential protection of zero modes in Majorana islands

S. M. Albrecht[*], A. P. Higginbotham[*], M. Madsen, F. Kuemmeth,
T. S. Jespersen, J. Nygård, P. Krogstrup, and C. M. Marcus

*Nature* **531**, 206-209 (2016)

It presents measurements on InAs-Al nanowire hybrid quantum dots brought into the topological regime by applying a magnetic field. All devices were fabricated by Sven Marian Albrecht based on nanowires grown by Peter Krogstrup. Measurements and data analysis were done by Sven Marian Albrecht together with Andrew Higginbotham and Morten Madsen under the supervision of Charles Marcus. Thomas Jespersen, Ferdinand Kuemmeth and Jesper Nygård contributed to interpreting the data and gave valuable input. The manuscript was written by Sven Marian Albrecht and Andrew Higginbotham.

---

[*] These authors contributed equally to this work.

## 6.1 INTRODUCTION

Majorana zero modes are quasiparticle excitations in condensed matter systems that have been proposed as building blocks of fault-tolerant quantum computers [16]. They are expected to exhibit non-Abelian particle statistics, in contrast to the usual statistics of fermions and bosons, enabling quantum operations to be performed by braiding isolated modes around one another [16,17]. Quantum braiding operations are topologically protected insofar as these modes are pinned near zero energy, and the pinning is predicted to be exponential as the modes become spatially separated [22, 23]. Following theoretical proposals [37, 38], several experiments have identified signatures of Majorana modes in proximitized nanowires [39–41, 127, 128] and atomic chains [43], with small mode-splitting potentially explained by hybridization of Majoranas [45,47,49]. Here, we use Coulomb-blockade spectroscopy in an InAs nanowire segment with epitaxial aluminum, which forms a proximity-induced superconducting Coulomb island (a "Majorana island") that is isolated from normal-metal leads by tunnel barriers, to measure the splitting of near-zero-energy Majorana modes. We observe exponential suppression of energy splitting with increasing wire length. For short devices of a few hundred nanometers, sub-gap state energies oscillate as the magnetic field is varied, as is expected for hybridized Majorana modes. Splitting decreases by a factor of about ten for each half a micrometer of increased wire length. For devices longer than about one micrometer, transport in strong magnetic fields occurs through a zero-energy state that is energetically isolated from a continuum, yielding uniformly spaced Coulomb-blockade conductance peaks, consistent with teleportation via Majorana modes [115,116]. Our results help to explain the trivial-to-topological transition in finite systems and to quantify the scaling of topological protection with end-mode separation.

## 6.2 THE MAJORANA ISLAND

The set of structures we investigate consist of InAs nanowires grown by molecular beam epitaxy in the [0001] wurtzite direction with an epitaxial Al shell on two facets of the hexagonal cross section [84]. The Al shell was removed except in a small segment of length $L$ and isolated from normal metal (Ti/Au) leads by electrostatic gate-

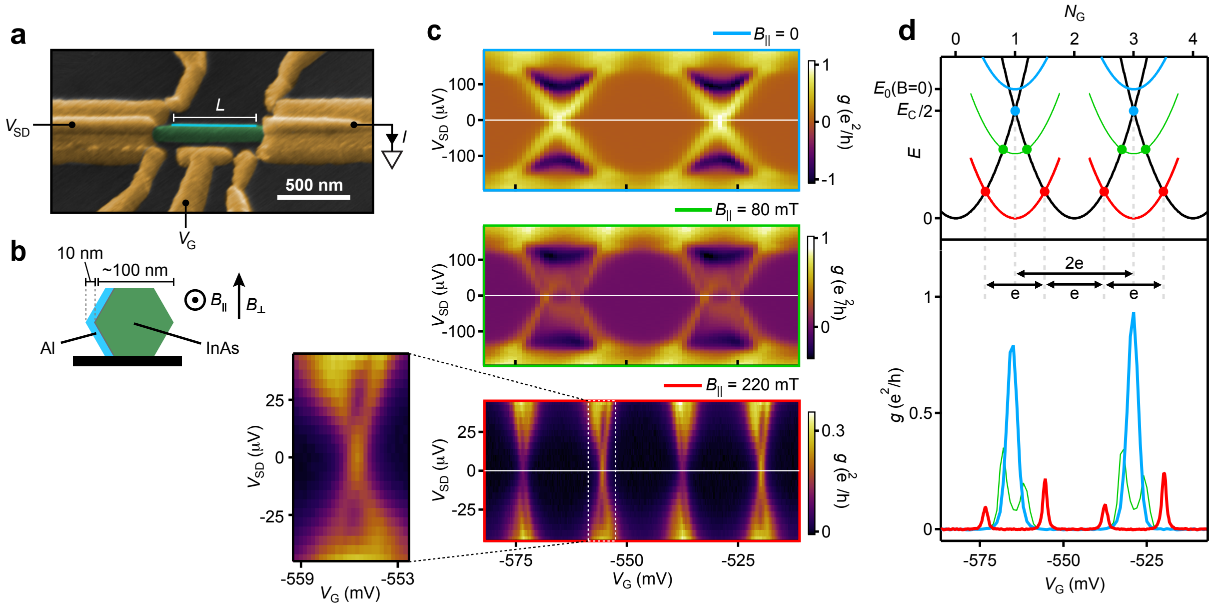

Figure 6.1: **Majorana island device. a**, Electron micrograph (false color) of a device that is lithographically similar to the measured devices. Gold contacts (yellow), InAs nanowire (green), and two-facet Al shell of length $L$ (light blue). Applied voltage bias, $V_{SD}$, and gate voltage, $V_G$, indicated. **b**, Cross section of hexagonal InAs nanowire, showing orientation of Al shell and field directions $B_{||}$ and $B_\perp$. **c**, Differential conductance, $g$, as a function of gate voltage, $V_G$, and source-drain bias, $V_{SD}$, for parallel magnetic fields, $B_{||} = 0, 80, 220$ mT, showing a series of Coulomb diamonds. For $B_{||} = 0$ the Coulomb diamonds are evenly spaced. An odd diamond has appeared for $B_{||} = 80$ mT. For $B_{||} = 220$ mT the Coulomb diamonds feature evenly spaced discrete states while the period in gate voltage has halved. Horizontal white lines indicate cuts in (d). **d**, (upper panel) Energy $E_N$ of the device with electron occupancy $N$, as a function of normalized gate voltage $N_G$. Ground-state energies for even (odd) $N$ shown in black (color). Odd-$N$ energies are raised by the single-particle-state energy, $E_0$ compared to even-$N$ energies. The even-$N$-only regime, $E_0 > E_C/2$ (light blue), and the even-and-odd-$N$ regime, $E_0 < E_C/2$ (green) are indicated. The Majorana case, $E_0 = 0$, is in red. Transport can occur at the intersections of parabolas, indicated by circles. (lower panel) Differential conductance, $g$, versus gate voltage $V_G$ at zero bias from measurements in (c) for magnetic fields $B_{||} = 0, 80, 220$ mT. The splitting of the $2e$-periodic peak (light blue line) reflects a transition from Cooper pair tunneling to single-quasiparticle charging of the quantum dot. Evenly spaced, $1e$ periodic Coulomb peaks are characteristic of a zero-energy state.

controlled barriers (Figure 6.1a). Charging energy, $E_C$, of the device ranges from greater than to less than the superconducting gap of Al ($\sim$ 0.2 meV). The thin Al shell ($8-10$ nm thickness on the two facets) gives a large critical field, $B_c$, before superconductivity is destroyed: for fields along the wire axis, $B_{c,||} \sim 1$ T; out of the plane of the substrate but roughly in the plane of the two Al-covered facets, $B_{c,\perp} \sim 700$ mT (Figure 6.1b). The very high achieved critical fields make these wires a suitable platform for investigating topological superconductivity [84].

Five devices over a range of Al shell lengths $L \sim 0.3-1.5\,\mu\mathrm{m}$ were measured (see Methods for device layouts). Charge occupation and tunnel coupling to the leads were tuned via electrostatic gates. Differential conductance, $g$, in the Coulomb blockade regime (high-resistance barriers) was measured using standard ac lock-in techniques in a dilution refrigerator (electron temperature $\sim$ 50 mK).

Figure 6.1c shows $g$ as a function of gate voltage, $V_G$, and source-drain bias, $V_{SD}$. For the $L = 790$ nm device, the zero-field data (top panel) show a series of evenly spaced Coulomb diamonds with a characteristic negative-differential conductance (NDC) region at higher bias. NDC is known from metallic superconductor islands [120, 121] and has recently been reported in a proximitized semiconductor device similar to those investigated here [72]. The zero-magnetic-field diamonds reflect transport via Cooper pairs, with gate voltage period proportional to $2e$, the charge of a Cooper pair. At moderate magnetic fields (Figure 6.1c, middle panel), the large diamonds shrink and a second set of diamonds appears, yielding even-odd spacing of Coulomb blockade zero-bias conductance peaks [129], as seen in the cuts in Figure 6.1d. At larger magnetic fields (Figure 6.1c, lower panel) Coulomb diamonds are again periodic, now with precisely half the spacing of the zero-field diamonds, corresponding to $1e$ periodicity. NDC is absent, and resonant structure is visible within each diamond, indicating transport through discrete resonances at low bias and a continuum at high bias (see magnification in Figure 6.1c). Coulomb blockade conductance peaks at high magnetic field (see Figure 6.1d for zero bias cuts) with regular $1e$ periodicity (half the zero-field spacing) accompanied by a discrete subgap spectrum is a proposed signature of electron teleportation by Majorana end states [115, 116]. We designate as a 'Majorana island' (MI) the ungrounded tunneling device in this high-field regime, where a subgap state near zero energy, energetically isolated from a continuum, leads to $1e$-periodic Coulomb blockade conductance peaks.

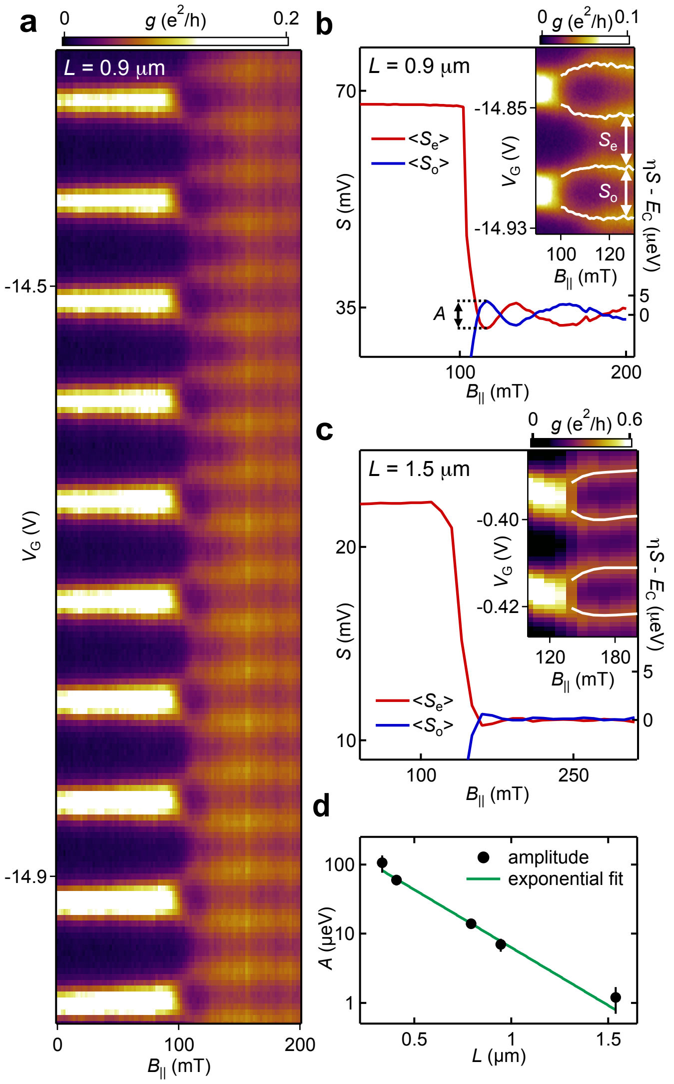

Figure 6.2: **Peak splitting in magnetic field. a**, Zero-bias conductance, $g$, as a function of gate voltage, $V_G$, and parallel magnetic field, $B_{||}$, for $L \sim 0.9$ µm device, showing a series of $2e$-periodic Coulomb peaks below $\sim$ 100 mT and $1e$ nearly-periodic peaks above $\sim$ 100 mT. **b**, (inset) High-resolution measurement for $L = 0.9$ µm (a) with overlay of peak center. Even and odd peak spacings, $S_{e,o}$, are indicated by arrows. (main panel) Average peak spacing for even and odd Coulomb valleys, $\langle S_{e,o} \rangle$, from measurement in (a) as a function of magnetic field, $B_{||}$. The Coulomb peaks become evenly spaced at $B_{||} = 110$ mT; afterwards their spacing oscillates around $\langle S_e \rangle = \langle S_o \rangle$. Right axis shows energy scale $\eta S - E_C \propto E_0$ in $1e$-regime ($\eta$ is gate lever arm, see text). **c**, Same as in (b) but for a longer wire, $L = 1.5$ µm. **d**, Oscillatory amplitude, $A$, plotted against the shell length, $L$, for 5 devices from 330 nm to 1.5 µm (black dots) and exponential fit to $A = A_0 \exp(-L/\xi)$ with $A_0 = 300$ µeV and $\xi = 260$ nm. Error bars indicate uncertainties propagated from lever arm measurements and fits to peak maxima.

Zero-bias conductance can be qualitatively understood within a simple zero-temperature model where the energy of the superconducting island—with or without subgap states (Figure 6.1d)—is given by a series of shifted parabolas, $E_N(N_G) = E_C/2(N_G - N)^2 + p_N E_0$, where $N_G = CV_G/e$ is the gate-induced charge (electron charge $e$ and gate capacitance $C$) [117, 118, 120, 121, 124, 129]. $E_0$ is the energy of the lowest quasiparticle state, which is filled for odd parity ($p_N = 1$, odd $N$), and empty for even parity ($p_N = 0$, even $N$) [72]. Transport occurs when the ground state has a charge degeneracy, i.e., when the $E_N$ parabolas intersect. For $E_0 > E_C/2$, the ground state always has even parity; transport in this regime occurs via tunneling of Cooper pairs at degeneracies of the even-$N$ parabolas. This is the regime of the $2e$-periodic Coulomb blockade peaks seen at low magnetic fields (Figure 6.1d, blue). The odd charge state is spinful and can be lowered by Zeeman energy when a magnetic field is applied. For sufficiently large field, such that $E_0 < E_C/2$, an odd-$N$ ground state emerges. This transition from 2$e$ charging to 1$e$ charging is seen experimentally as the splitting of the $2e$-periodic Coulomb diamonds into the even-odd double-diamond pattern in Figure 6.1d (green trace). In this regime the Coulomb peak spacing is proportional to $E_C + 2E_0$ for even diamonds and $E_C - 2E_0$ for odd diamonds [117, 118]. For the particular case of a zero-energy Majorana state, $E_0 = 0$, peak spacing is regular and $1e$-periodic. This regime is observed at higher fields (Figure 6.1d, red), though not sufficiently high to destroy superconductivity.

## 6.3 EXPONENTIAL PROTECTION

Coulomb peak spacings are measured as a function of magnetic field, allowing the state energy, $E_0(B)$, to be extracted. An example, showing 10 consecutive peaks for the $L = 0.9$ µm device, is shown in Figure 6.2a. The peaks are $2e$-periodic at $B = 0$, start splitting around $\sim 95$ mT, and become $1e$-periodic at $\sim 110$ mT, well below the spectroscopically observed closing of the superconducting gap at $B_c \sim 600$ mT (see Methods). This points towards the presence of a state close to zero energy within the superconducting regime over a range of $\sim 500$ mT.

Separately averaging even and odd Coulomb peak spacings, $\langle S_{e,o} \rangle$, over an ensemble of adjacent peaks reveals oscillations around the $1e$-periodic value as a function of applied magnetic field. This is consistent with an oscillating state energy $E_0$ due to hybridized Majorana modes [45, 47, 49]. For the $L = 0.9$ µm device (Figure 6.2b), peak spacing oscillations yield an energy oscillation amplitude $A = 7.0 \pm 1.5$ µeV, converted from gate voltage to energy using the gate lever arm, $\eta$, extracted independently from the slope of the Coulomb diamonds. For the $L = 1.5$ µm device (Figure 6.2c) average Coulomb peak spacing oscillations based on 22 consecutive peaks yield a barely resolvable amplitude, $A = 1.2 \pm 0.5$ µeV.

Oscillation amplitudes for the five measured devices (see Methods for device details), are shown in Figure 6.2d along with a two-parameter fit to an exponential function, $A = A_0 e^{-L/\xi}$, giving $A_0 = 300$ µeV and $\xi = 260$ nm as fit parameters. The data fits well to the predicted exponential form that characterizes the topological protection of Majorana modes [22, 23, 45].

## 6.4 EXCITATION SPECTRUM AND BIAS SPECTROSCOPY

Excited states of the MI are probed using finite-bias transport spectroscopy. This technique requires a fixed gate voltage, chosen such that at zero bias the electrochemical potential of the leads aligns with the middle of the spectroscopic gap of the MI. With this choice, the conductance at source-drain bias $V_{\mathrm{SD}}$ is due to states at energy $eV_{\mathrm{SD}}/2$. A conductance peak at zero bias corresponds to a zero-energy state. In the case shown in Figs. 6.3(a,b), the gate voltage is tuned using the characteristic finite-bias conductance spectra for a short InAs/Al island, investigated previously in Ref. [72]. Ground-state energies determined by finite-bias spectroscopy match those extracted from zero-bias peak spacings (see Extended Data Figure 6.11).

Bias spectroscopy shows discrete zero-energy states emerging at sufficient applied field over a range of device lengths. In a short device (Figure 6.3c), the discrete state moves linearly in magnetic field, passing through zero and merging with a continuum at $V_{\mathrm{SD}} \sim 100$ µeV. This merging is expected for Majorana systems in the short-length limit, where quenching of spin-orbit coupling results in unprotected parity crossings and state intersections at high energy [47]. Rather than passing directly through zero, the first zero crossing extends for 40 mT, which is not understood. Medium-length devices show the subgap state bending back toward zero after zero crossings (Figure 6.3d), in agreement with theoretical predictions for the emergence of Majorana behavior with increasing system length [47, 49]. For a long device ($L = 1.5$ µm), bias spectroscopy shows a zero-energy

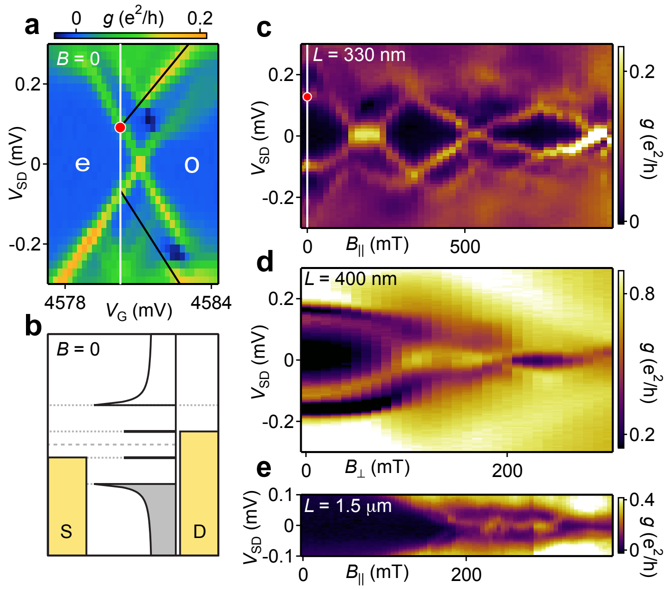

Figure 6.3: **Bias spectroscopy. a**, Conductance, $g$, versus bias voltage, $V_{\mathrm{SD}}$, and gate voltage, $V_{\mathrm{G}}$. Black lines indicate conductance due to bound state, red marker is at $eV_{\mathrm{SD}} = 2E_0$. **b**, Quantum dot and lead density of states at the voltage configuration indicated by red marker in (a). Changing voltage bias moves along the white line in (a). **c**, Conductance versus source-drain bias and magnetic field, $B_{||}$, for $L = 330$ nm device with gate voltage fixed to position indicated by white line in **a**. **d**, Conductance versus source-drain bias and magnetic field, $B_{\perp}$, for $L = 400$ nm device. **e**, Conductance versus source-drain bias and magnetic field, $B_{||}$, for $L = 1.5$ μm device.

state separated from a continuum at higher bias (Figure 6.3e). The zero-energy state is present over a field range of 120 mT, with an associated energy gap $(30\ \mu\mathrm{eV})/k_{\mathrm{B}} = 0.35$ K.

The evolution from unprotected parity crossings, to energetically isolated oscillating states, and then to a fixed zero-energy state, with increasing device length is consistent with the expected crossover from a strongly overlapping precursor of split Majoranas to a topologically protected Majorana state locked at zero energy [47,49]. Note that in the data in Figure 6.3e, the signal from the discrete state disappears above $B_{||} = 320$ mT. This is not expected within a simple Majorana picture. Even though the zero-bias peak disappears, the peak spacing remains $1e$-periodic (see Methods).

The observed effective g-factors, $g \sim 20 - 50$, extracted from the addition spectrum and bias spectroscopy (see Methods), are large compared to previous studies on InAs nanowires [40, 70, 130], perhaps resulting from field focusing from the Al shell. The measured gap to the continuum at zero magnetic field is consistent with the gap of aluminum $\Delta_{\mathrm{Al}} \sim 180$ µeV, and is roughly the same in all devices. The discrete subgap states (Figure 6.3c-e) have zero-field energy less than but comparable to the gap, ranging from $E_0\,(B = 0) \sim 50 - 160$ µeV, consistent with expectations for half-shell geometries [78]. The measured gap between the near-zero-energy state and the continuum in the high-field (topological) regime, $\Delta_{\mathrm{T}} \sim 30$ µeV, along with the coherence length extracted from the exponential fit to the length-dependent splitting (Figure 6.2d), $\xi \sim 260$ nm, are consistent with topological superconductivity. Within this picture, at low magnetic fields, the gap and coherence length are related to the strength of spin-orbit coupling, yielding a value $\alpha_{\mathrm{SO}} \sim \xi \cdot \Delta_{\mathrm{T}} = 8 \times 10^{-2}$ eV · that is consistent with previously reported values in InAs nanowires [40, 131]. For a single subband picture, this implies a Fermi velocity $v_{\mathrm{F}} = \alpha_{\mathrm{SO}}/\hbar = 1 \times 10^4$ m/s that is lower than expected, suggesting that more than one subband is occupied under the Al shell, though we are not able to extract the number of modes directly.

## 6.5 SIGNATURES OF ELECTRON TELEPORTATION

Finally, we consider the magnetic field dependence of Coulomb blockade peak heights (as opposed to spacings), as seen in Figure 6.4. We found in most devices that below the field $B^*$ where $2e$-periodic peaks split, all peaks were uniformly high amplitude. Above $B^*$, peak heights were rapidly suppressed and remained low up to a second characteristic field, $B^{**}$, coincident with $1e$ periodicity (i.e., the field where even-odd spacing differences vanished). Above $B^{**}$, peak heights recovered. In the longer wires, peaks were nearly absent between $B^*$ and $B^{**}$, as seen in Figure 6.4c.

We interpret these observations as follows: In the present lead-wire-lead geometry, transport above $B^*$ involves single electrons entering one end of the wire and leaving from the other. The onset of uniform spacing with the reappearance of high peaks above $B^{**}$ indicates the emergence of a state (or states) at zero energy with strong wave function support at both ends of the wire. This is consistent with teleportation of electrons from one end of the wire to the other via a Majorana mode [115, 116], though not necessarily a unique signature [132]. Thus while the simultaneous brightening of peaks with their becoming uniformly spaced at $B^{**}$ suggests a subgap/Majorana

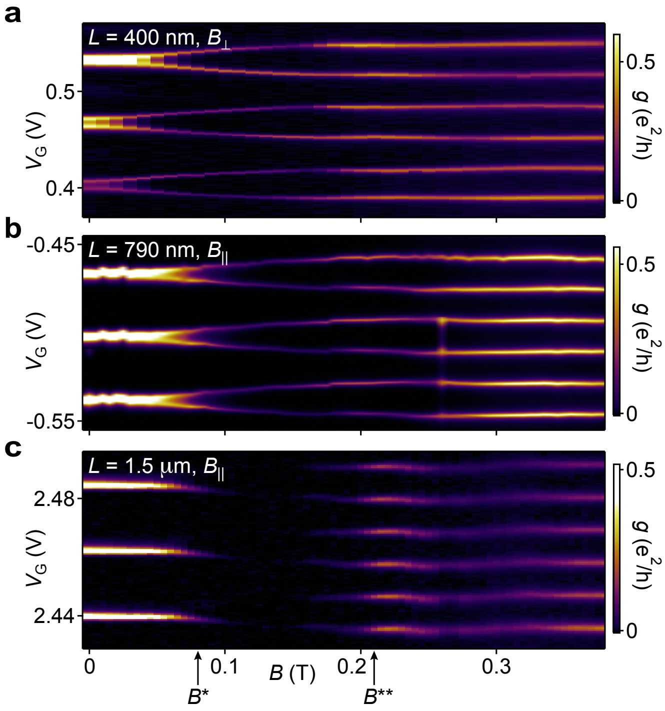

Figure 6.4: **Length dependence of Coulomb peak heights. a-c**, Conductance as a function of magnetic field and gate voltage for device lengths $L = 400$ nm, 790 nm, 1.5 μm. Coulomb peaks become dim at field $B^*$ and brighten at field $B^{**}$, particularly for the $L = 1.5$ μm device, consistent with teleportation at fields above above $B^{**}$.

mode moving to the ends of the wire as it moves to zero energy, we cannot rule out other forms of end-localized zero-energy states that could appear above a critical field.

## 6.6 CONCLUSION

In summary, we have studied Majorana islands composed of InAs nanowires covered on two facets with epitaxial Al, for a range of device lengths. Zero-energy states are observed for wires of all lengths away from zero field. Oscillating energy splittings, measured using Coulomb blockade spectroscopy, are exponentially suppressed with wire length, with a characteristic length $\xi = 260$ nm. This constitutes an explicit demonstration of exponential protection of zero-energy modes. Finite-bias measurements show transport through a discrete zero-energy state, with a measured topological gap $\Delta_T = 30$ μeV for long devices. The extracted $\Delta_T$ and $\xi$ are consistent with known parameters for InAs nanowires and the emergence of topological superconductivity. Brightening of Coulomb peaks at the field where spacing becomes uniform for longer devices suggests the presence of a robust delocalized state connecting the leads, and provides experimental support for electron teleportation via Majorana modes.

## 6.7 EXTENDED DATA

### 6.7.1 *Sample preparation*

The InAs nanowires with epitaxial Al shell were grown via a two-step process by molecular beam epitaxy. First, the InAs nanowires were grown using the vapor-liquid-solid method with Au as a catalyst at 420°C. Second, after cooling the system to $-30°$C the Al was grown on two facets of the hexagonal cross section [84]. Afterwards the nanowires were deposited on degenerately doped Si substrates with 100-500 nm thick thermal oxides using either wet or dry deposition techniques. Wet deposition involves sonicating a growth substrate of nanowires in methanol for a few seconds, then putting several drops of the nanowire-methanol solution onto the chip surface using a pipette. Dry deposition was done by bringing a small piece of cleanroom wipe in touch with the growth substrate, then afterwards swiping it onto the chip surface. We find that while wet deposition results in a more uniform dispersion of nanowires on the chip surface, dry deposition is faster and less wasteful with nanowires. Selective removal of the Al shell was done by patterning etch windows using electron beam lithography on both sides of the nanowire, plasma cleaning the surface of the nanowire using oxygen, then etching the Al using a Transene Al Etchant D with an etching time of 10 seconds at 50°C. Depending on the device, ohmic contacts to the InAs core were fabricated using either ion milling or sulfur passivation to remove surface oxides. Ion milling was done for times ranging from 85 s to 110 s using a Kaufman & Robinson KDC 40 4-CM DC Ion Source with an acceleration voltage of 120V and an ion beam current density of 0.5 mA/cm$^2$ at the chip surface. Sulfur passivation was done using a 2.1% solution of $(NH_4)_2S$ in DI water with 0.15 M dissolved elemental sulfur at 40°C for 20 minutes. This was followed by the deposition of 5 nm of Ti as a sticking layer and $70 - 100$ nm of Au for the ohmic contact. We found that ion milling resulted in more stable devices. Side and plunger gates were lithographically defined

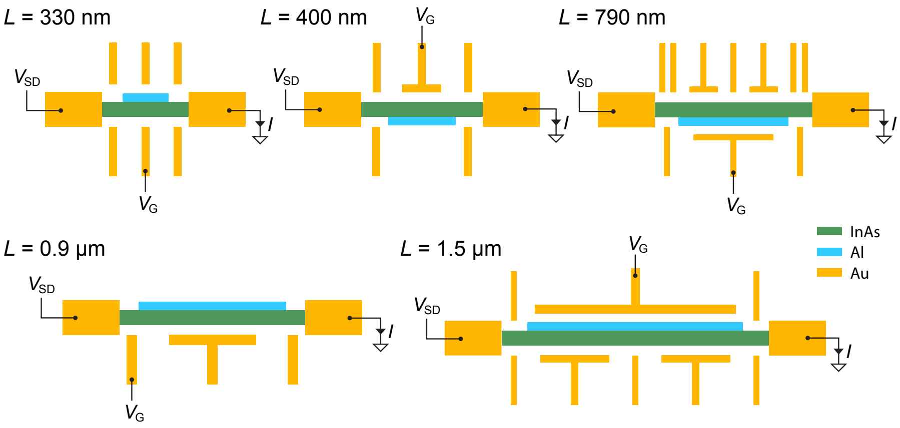

Figure 6.5: **Device Layouts.** Gate pattern for the five measured devices showing applied voltage bias, $V_{\mathrm{SD}}$, and gate voltage, $V_{\mathrm{G}}$.

in the same fabrication step as the ohmic contacts in order to increase device yield. PMMA was used as resist in all lithography steps.

### 6.7.2 *Device geometries*

Gate patterns of the five measured devices are shown in ED Figure 6.5. With the exception of the $L = 0.9$ μm device, all measurements involving gate dependence are tuned through resonances using the plunger gate on either the Al side or the uncoated InAs side. For the $L = 0.9$ μm device, the lower left side gate is used to tune through resonances of the quantum dot, because the central plunger gate was not bonded during the cool down.

### 6.7.3 *Measurements*

Transport measurements were carried out in an Oxford Triton dilution refrigerator with a base electron temperature of $T \sim 50$ mK and a 6-1-1 T vector magnet. Differential conductance, $g = dI/dV_{\mathrm{SD}}$, was measured using the AC-lockin technique with an excitation voltage in the range 2-6 μV.

### 6.7.4 *Peak spacing data summary*

The exponential curve in Figure 6.2d (main text) is derived from even-odd peak spacing measurements in the high critical field directions, $B_{||}$ and $B_{\perp}$, summarized in ED Figure 6.6. Suppression of spacing fluctuations with increased device length is clearly visible. The mea-

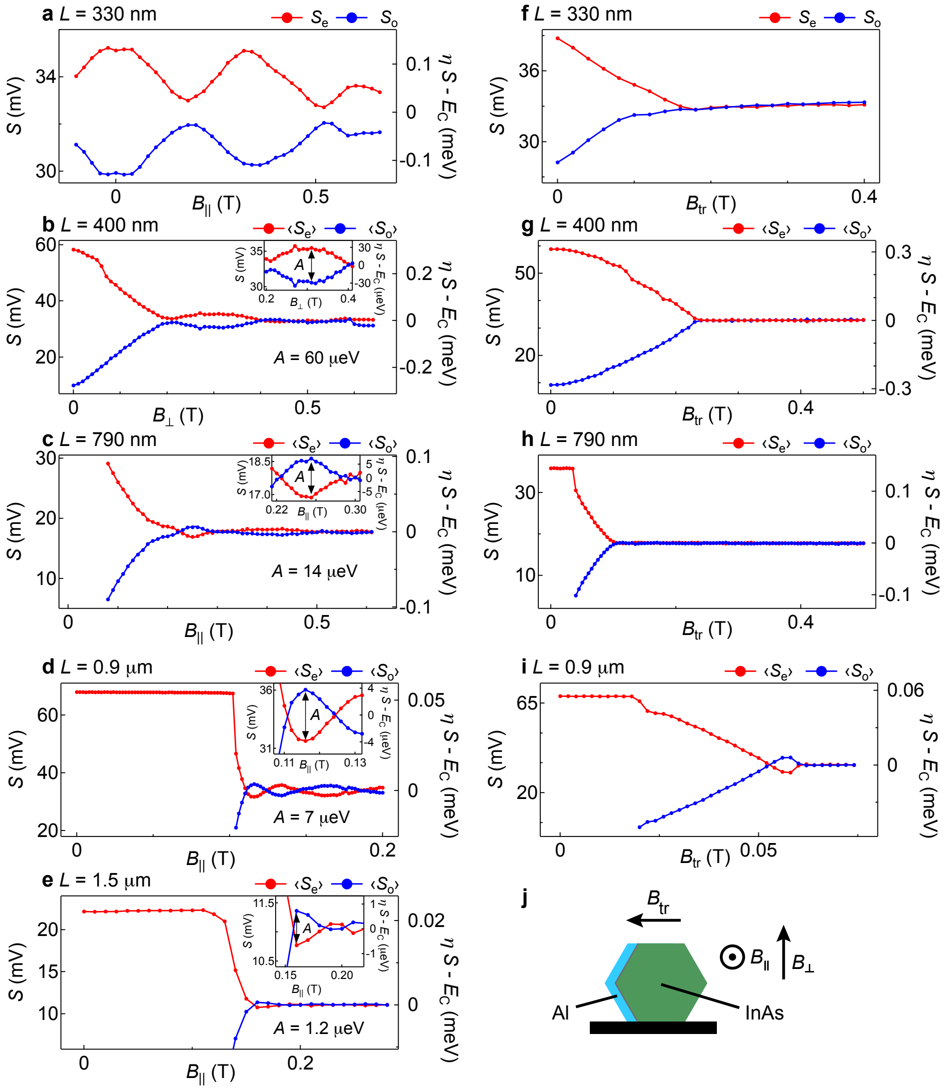

Figure 6.6: **Even-odd peak spacing summary. a-i**, Peak spacings for even and odd valleys, $S_{e,o}$, versus applied magnetic field, similar to Figure 6.2b, for different device lengths. Left axis shows peak spacings, right axis shows corresponding energy scales, converting from gate voltage to energy by the lever arm, $\eta$, measured independently from Coulomb blockade diamonds. Inset shows a magnification of the first energy splitting with an arrow indicating where $A$ is measured. **j**, Cross section of the nanowire, showing the applied field directions $B_{||}$, $B_{\perp}$ and $B_{\text{tr}}$.

| L [nm] | $E_C$ [meV] | $\eta$ [eV/V] | $A$ [µeV] |
|---|---|---|---|
| 330 | 1.6 | 0.048 | 106 |
| 400 | 0.40 | 0.012 | 60 |
| 790 | 0.14 | 0.008 | 14 |
| 950 | 0.054 | 0.0016 | 7 |
| 1540 | 0.022 | 0.002 | 1.2 |

Table 6.1: Device length, $L$, charging energy, $E_C$, lever arm, $\eta$, and characteristic amplitude, $A$, for the five measured devices.

sured $A$ is indicated by black arrows in the inset, and the values are recorded in ED Table 6.1 for each device length, along with charging energies and lever arms.

For $L = 330$ nm, Coulomb peak fluctuations became uncorrelated after several peaks. To obtain a large statistical ensemble, fluctuations were averaged over five sets of Coulomb peaks taken in different device tunings. ED Figure 6.6a shows data from a single set of peaks, and ED Table 6.1 reports the full ensemble average.

In a transverse magnetic field applied in the low critical field direction, $B_{\text{tr}}$, shown in ED Figure 6.6f-i, the oscillations are absent, with the exception of an initial overshoot for $L = 0.9$ µm at $B_{\text{tr}} = 55$ mT (ED Figure 6.6i), before the system is driven into the normal state at $B_{\text{tr}} \sim 65$ mT.

### 6.7.5 *Magnetic field orientation*

The direction of the nanowire on the chip was found by orienting the magnetic field from a vector magnet in the chip plane and spectroscopically measuring the anisotropy of the critical magnetic field. By comparing to the wire-direction based on optical and electron micrographs, we estimate an angular precision of $\pm$ 3 degrees.

### 6.7.6 *Critical field measurements*

The observed $2e$-$1e$ splitting at $B_{||} \sim 95$ mT is compared to the closing of the superconducting gap at a considerably higher critical field, $B_{c,||}$, in ED Figure 6.7. Bias spectroscopy in ED Figure 6.7b shows a closing of the superconducting gap at $B_{c,||} \sim 600$ mT, more than 500 mT after the onset of evenly spaced $1e$-periodic Coulomb peaks. The change

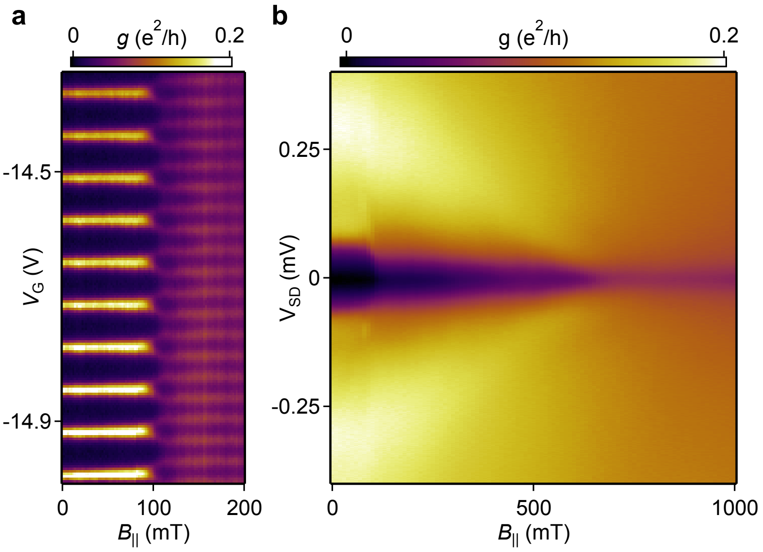

Figure 6.7: **Critical field measurement for 0.9 μm device. a**, Conductance, $g$, versus gate voltage, $V_G$, and parallel magnetic field, $B_{||}$, at zero bias showing the 2$e$-1$e$ peak splitting. **b**, Conductance versus source drain voltage, $V_{SD}$, and $B_{||}$, taken at $V_G = -14.92$ V, showing a closing of the superconducting gap at $B_c \sim 640$ mT, more than 500 mT after the onset of 1$e$-periodicity.

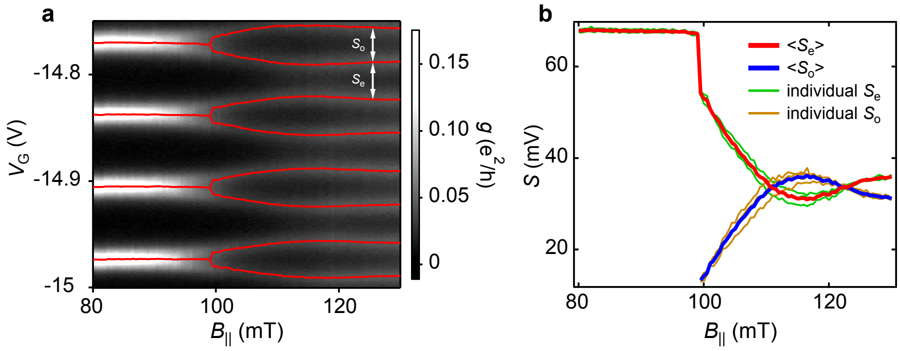

Figure 6.8: **Oscillating 1e-periodic peak spacings. a**, Zero-bias conductance, $g$, versus gate voltage, $V_G$, and parallel magnetic field, $B_{||}$, at zero bias showing the 2$e$-1$e$ peak splitting for $L = 0.9$ μm. The fit peak position is indicated by a red line, even and odd peak spacings, $S_{e,o}$, indicated by white arrows. **b**, Peak spacing, $S_{e,o}$, for even and odd valleys as a function of $B_{||}$. The plot shows the average peak spacing $\langle S_{e,o} \rangle$ as well as the individual peak spacings, $S_{e,o}$.

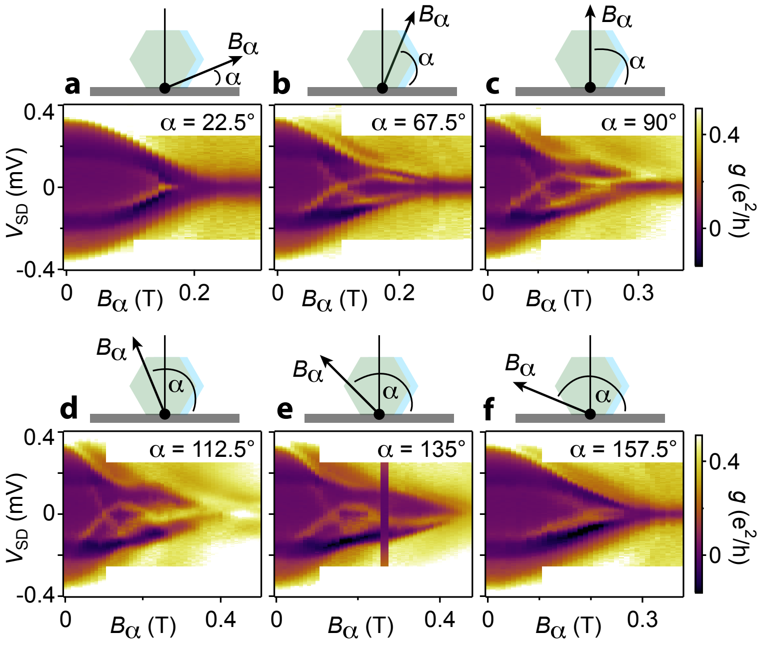

Figure 6.9: **Angle dependence of state-continuum anti-crossing. a-f**, Differential conductance, $g$, as a function of source-drain bias, $V_{SD}$, and magnetic field $B_\alpha$ for different angles, $\alpha = 22.5 - 157.5°$, in the plane perpendicular to the nanowire direction. Measurements are from the $L = 400$ nm device.

from $2e$ to $1e$-periodicity at $B_{||} \sim 100$ mT in ED Figure 6.7a coincides with a reduction in the measured Coulomb gap in ED Figure 6.7b, reflecting the transition from Cooper pair charging (energy penalty $2E_C$) to single-electron charging (energy penalty $E_C$). The measurement in ED Figure 6.7b was taken in a Coulomb valley at the gate voltage $V_G = -14.92$ V.

### 6.7.7 *Averaging of peak spacings*

In Figure 6.2b of the main text, we show the extracted average peak spacing for several even and odd Coulomb valleys. A high resolution measurement of the $2e$-$1e$ splitting is shown in ED Figure 6.8a. The individual even and odd valleys, $S_{e,o}$ in ED Figure 6.8b, exhibit the same oscillating behavior but show a small deviation from the average between $100 - 125$ mT, which might be attributable to $g$-factor fluctuations for successive charge occupations of the quantum dot. Below 100 mT the fluctuations are very small, giving an indication of instrumental noise in the measurement.

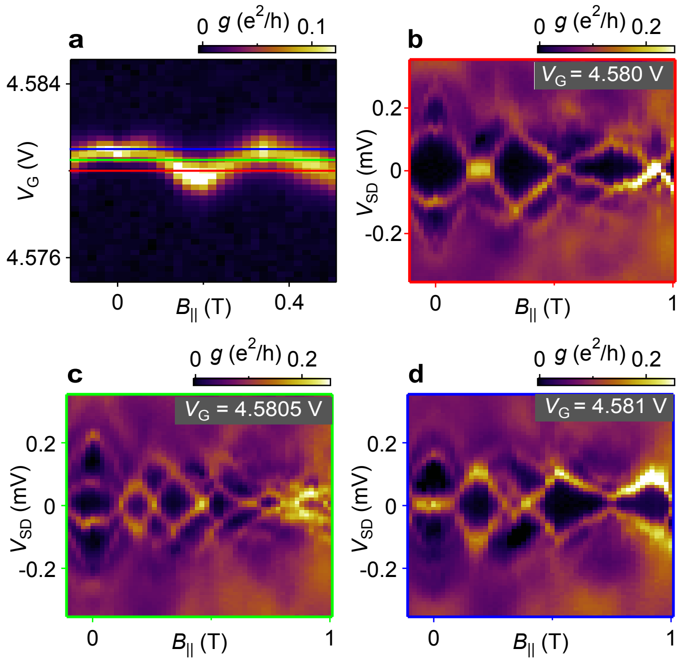

Figure 6.10: **Gate positions. a**, Differential conductance, $g$, as a function of gate voltage, $V_G$, and parallel magnetic field, $B_{||}$, for $L = 330$ nm. Three different gate positions are indicated by colored horizontal lines. **b-d**, Differential conductance as function of bias voltage, $V_{SD}$, and $B_{||}$ for the three gate voltages in (a).

### 6.7.8 *Angle dependence*

Angle dependence of the anti-crossing of the state with the continuum for $L = 400$ nm is shown in ED Figure 6.9. We focus on magnetic fields, $B_\alpha$, with angles, $\alpha$, in the plane perpendicular to the nanowire direction. The measurements show a pronounced anti-crossing between the sub-gap state and an excitation continuum ($\alpha = 112.5°$ and $\alpha = 135°$) that is significantly reduced for $\alpha = 67.5°$. Interpreting angle dependence is complicated by the anisotropy of g-factor and critical field. The critical field is maximized for $\alpha = 120°$, and is reduced drastically for near-perpendicular field alignment ($\alpha = 22.5°$). The observed g-factors are highly dependent on field orientation and device tuning. For the $L = 400$ nm device shown in ED Figure 6.9, we found an approximately sinusoidal variation in $g$-factor by a factor of 2, with maximum g-factor occurring near $\alpha = 90°$.

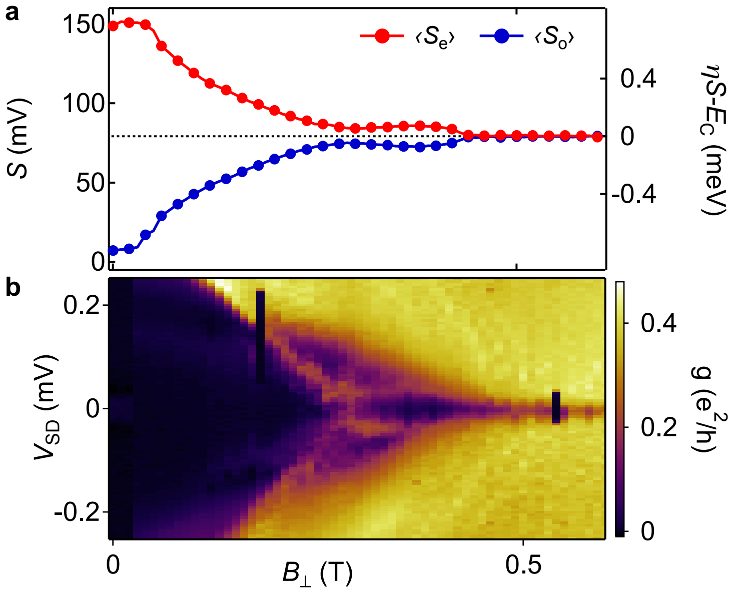

Figure 6.11: **Comparison of peak spacings and bias spectroscopy. a**, Peak spacing for even and odd valleys, $\langle S_{\mathrm{e,o}} \rangle$, versus applied field, $B_\perp$. **b**, Differential conductance, $g$, as a function of source-drain bias, $V_{\mathrm{SD}}$, and magnetic field.

### 6.7.9 *Choice of gate voltage for bias spectroscopy*

For bias spectroscopy, the gate voltage is fixed either by interpreting Coulomb diamonds, as discussed in the main text, or from even-odd peak spacings. While details of the bias spectroscopy, such as locations of zero-crossing, depend on the choice of gate voltage, general features such as slopes, typical fluctuation amplitude, and the presence of a robust excitation gap are not strongly affected by the choice of gate voltage (ED Figure 6.10).

### 6.7.10 *Comparison of addition energies and finite bias spectroscopy*

Peak spacings are used to measure the energy of the lowest-lying state. The same information is present in the bias spectroscopy, and gives consistent results, as shown in ED Figure 6.11.

### 6.7.11 *Bias spectroscopy of long device*

Common-mode fluctuations in Coulomb peak position were observed in the longest ($L = 1.5$ μm) device, as shown in ED Figure 6.12a. The fluctuations evidently correspond to a shift in the electro-

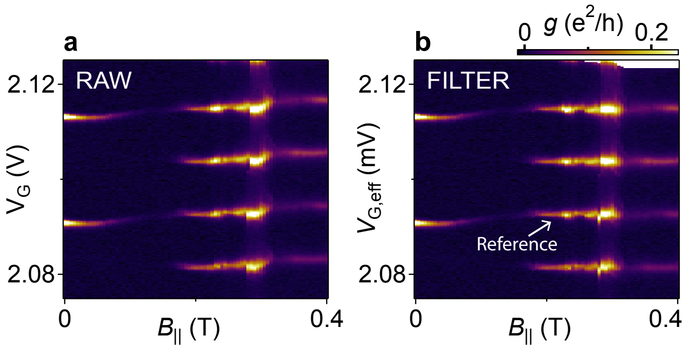

Figure 6.12: **Common-mode peak motion removal. a**, Differential conductance, $g$, versus gate voltage, $V_G$ and applied magnetic field $B_{||}$, for $L = 1.5$ µm device. **b**, Same as (a), but with effective gate voltage, $V_{G,eff}$, defined to remove common-mode peak motion. Reference Coulomb peak, used for common-mode removal, labeled.

chemical potential of the dot, likely due to a nearby, field-dependent charge trap. The fluctuations are small compared to charging energy, but complicate the application of bias spectroscopy which needs to be performed at fixed electrochemical potential. To correct for the fluctuations, we introduce an effective gate voltage,

$$V_{G,eff}(B) = V_G + \delta V(B), \tag{6.1}$$

that removes the common-mode peak motion. The offset voltage is zero at low field, when Coulomb peaks are $2e$ periodic ($\delta V(B) = 0$ for $B \leq 175$ mT). At high field, $\delta V(B)$ is chosen so that the reference Coulomb peak (labeled in ED Figure 6.12b) occurs at constant $V_{G,eff}$. All nonzero $\delta V(B)$ are listed in ED Table 6.2.

As shown in ED Figure 6.12b, this procedure removes the common-mode peak motion. In the case of the 1.5 µm device, bias spectroscopy is performed at fixed $V_{G,eff}$, which allows us to infer the energy of the sub-gap state at fixed electrochemical potential.

### 6.7.12 *Zero-energy state at successive Coulomb peaks*

The zero-energy state is robust over many successive Coulomb peaks, as shown in ED Figure 6.13. The full bias spectroscopy as a function of field is also reproducible over several peaks, as shown in ED Figure 6.14.

| B (mT) | $\delta V$ (mV) |
|---|---|
| 180 | 0.25 |
| 230 | 0.25 |
| 235 | 0.25 |
| 240 | 0.25 |
| 245 | 0.25 |
| 250 | 0.25 |
| 255 | 0.25 |
| 260 | 0.5 |
| 265 | 0.5 |
| 270 | 0.5 |
| 275 | 0.5 |
| 280 | 0.75 |
| 300 | 0.25 |
| 305 | 0.75 |
| 310 | 1.25 |
| 315 | 1.5 |
| 320 | 1.75 |
| 325 | 1.75 |
| 330 | 1.75 |
| 335 | 1.75 |
| 340 | 1.75 |
| 345 | 1.75 |
| 350 | 1.75 |
| 355 | 1.75 |
| 360 | 1.75 |
| 365 | 1.75 |
| 370 | 1.75 |
| 375 | 1.75 |
| 380 | 1.75 |
| 385 | 1.75 |
| 390 | 1.75 |
| 395 | 1.75 |
| 400 | 1.75 |

Table 6.2: All nonzero offset voltage values, $\delta V(B)$, for $L = 1.5$ µm device. Offset is defined for $B = 0, 5, 10, ..., 400$ mT.

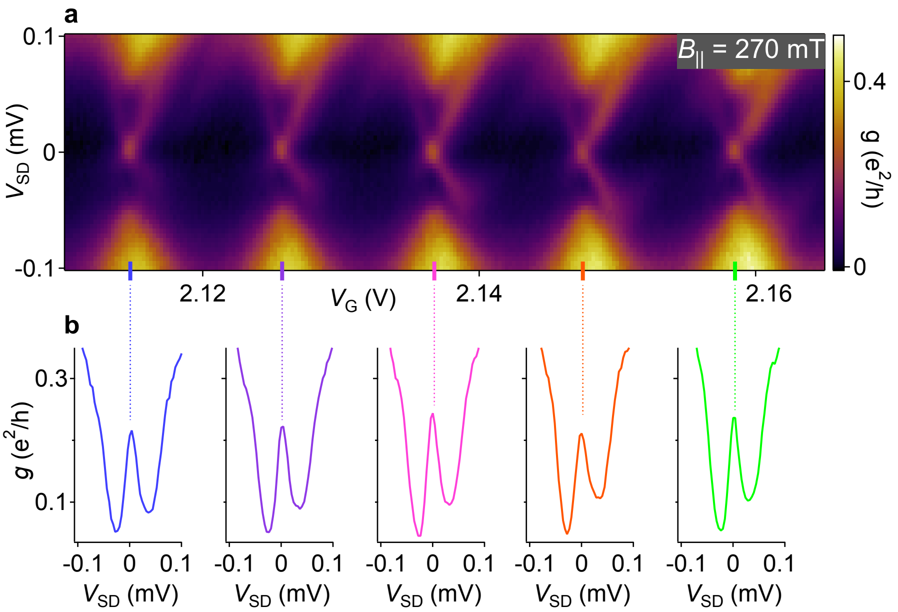

Figure 6.13: **Zero-energy state.** **a**, Differential conductance, $g$, as a function of bias voltage, $V_{\mathrm{SD}}$, and gate voltage, $V_{\mathrm{G}}$, for $L = 1.5$ µm and $B_{||} = 270$ mT, showing an evenly spaced Coulomb diamond pattern and the associated gapped zero-energy state. **b**, Differential conductance versus $V_{\mathrm{SD}}$, at the gate voltages indicated by colored ticks in (a). At these $V_{\mathrm{G}}$ values, the presence of a zero-energy state is indicated by a zero bias peak.

### 6.7.13 *Measured g-factors*

As can be seen in ED Figure 6.15 the state energy does not move linearly in magnetic field. A non-linear behavior with magnetic field is expected in the presence of strong spin-orbit coupling and a finite critical field.

If the behavior was strictly linear one would expect

$$B^{**} = \frac{E_0}{E_0 - E_C/2} B^*, \tag{6.2}$$

because the peak splitting at $B^*$ occurs when $E_0(B = 0) - E_Z = E_C/2$ and the state is at zero energy at $B^{**}$ when $E_Z = E_0(B = 0)$ (see Figure 6.4 in the main text for reference). The non-linear behavior of $E_0(B)$ at higher magnetic fields approaching $B^{**}$ renders this unsuitable for an accurate measurement of the state energy at zero field.

In the low field regime where the state energy is approximately linear with magnetic field we calculate an effective g-factor. Using this slope it is possible to give a rough estimate of the state energy $E_0(B = 0)$ assuming linear behavior and extrapolating the state energy to zero magnetic field.

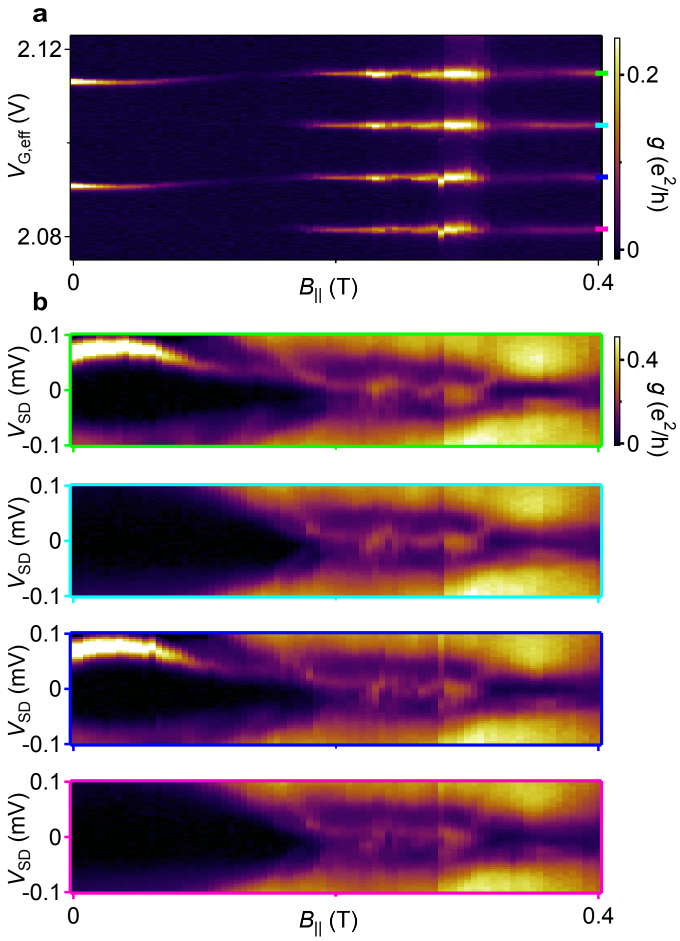

Figure 6.14: **Bias-spectroscopy at successive Coulomb peaks.** **a**, Differential conductance, $g$, versus $V_{G,eff}$ and applied magnetic field $B_{||}$. $V_{G,eff}$ is defined to remove common-mode peak motion, see Methods Section 'Bias spectroscopy of long device.' **b**, Differential conductance versus source-drain bias, $V_{SD}$, and applied magnetic field, $B_{||}$, at fixed $V_{G,eff}$ indicated on right axis of (a).

For bias spectroscopy it should be noted that for gate voltages in the middle of the spectroscopic gap (see main text) transport through a state at $V_{SD} = V_0$ indicates a state energy $E_0 = eV_0/2$. An example for $L = 330$ nm is shown in ED Figure 6.15a.

Using the addition spectrum, the state energy can be calculated from the peak spacing $S$ according to $E_0 = (\eta S - E_C)/2$. Examples of extracted effective g-factors in the linear range are shown in ED Figure 6.15b,c.

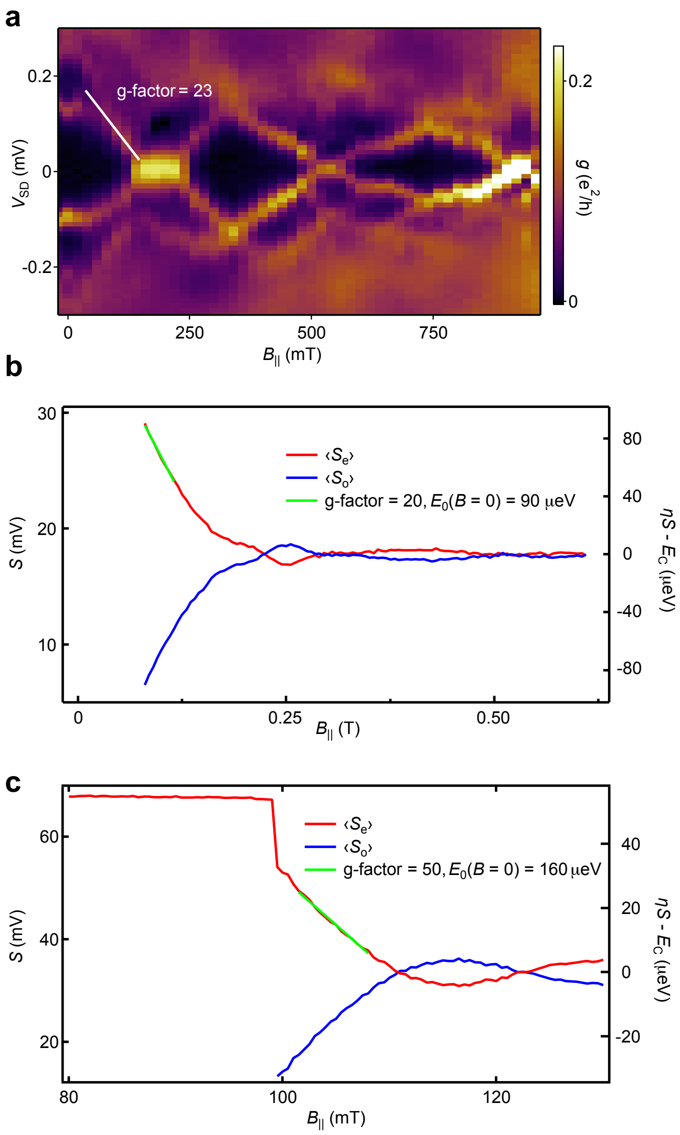

Figure 6.15: **Measurement of the g-factor for three devices. a**, Differential conductance, $g$, versus source-drain voltage, $V_{\mathrm{SD}}$, and applied magnetic field, $B_{||}$, for $L = 330$ nm showing g-factor $= 23$. **b**, Average even and odd peak spacings $\langle S_{e,o} \rangle$ as a function of $B_{||}$, for $L = 790$ nm, showing an extracted g-factor $= 20$. **c**, same as in (b) but for $L = 0.9$ μm with g-factor $= 50$.

# Part IV

# QUASIPARTICLE DYNAMICS II

# 7

# TRANSPORT SIGNATURES OF QUASIPARTICLE POISONING IN A MAJORANA ISLAND

This chapter will be published as:

Transport signatures of quasiparticle poisoning
in a Majorana island

All devices were fabricated by Sven Marian Albrecht based on nanowires grown by Peter Krogstrup. Measurements were done by Sven Marian Albrecht and Andrew Higginbotham under the supervision of Charles Marcus. The data analysis was done by Sven Marian Albrecht. Thomas Jespersen, Ferdinand Kuemmeth, and Jesper Nygård contributed to interpreting the data and gave valuable input. The theoretical model was developed by Esben Bork Hansen, Sven Marian Albrecht, Jeroen Danon, and Karsten Flensberg. The manuscript was written by Sven Marian Albrecht with input from all authors.

## 7.1 ABSTRACT

We investigate the effects of quasiparticle poisoning in a Majorana island with normal-metal leads. For strong island-lead couplings, an additional set of weak "shadow"-Coulomb diamonds shifted by 1e in gate voltage is observed, consistent with transport through the Majorana island in an excited (poisoned) state. At high magnetic fields, corresponding to 1e periodic Coulomb peaks, main-peaks and "shadow"-peaks merge, fully explainable using a simple model. Numerical simulations show good agreement with the experiment, allowing us give an estimate for the quasiparticle poisoning time of the Majorana island for strong coupling ($\sim$ 3 µs) and establish a lower bound for weak coupling ($>$ 10 µs). Increasing the magnetic field beyond the 1e periodic regime, we observe peak spacing oscillations that indicate transport through a hybridized near-zero-energy Majorana mode, with Majorana hybridization energy quantitatively consistent with earlier measurements.

## 7.2 INTRODUCTION

Due to their capacity to host Majorana end modes [37, 38], superconductor-semiconductor hybrid nanowire devices have been the subject of intense research interest in recent years [39–42, 127, 128]. Of particular relevance to Majorana fusion rule-, braiding-, and Majorana-based quantum computation-schemes [27–29, 87] is the Majorana island geometry, in which the topological hybrid nanowire acquires a charging energy that lifts the degeneracy between occupied and empty Majorana states [42, 115, 116, 133, 134], allowing for charge readout of the state parity. A fundamental bound to the coherence of Majorana based qubits is the quasiparticle poisoning time of the Majorana state [24, 27, 96]. Studies on metallic superconductors have explored associated quasiparticle poisoning rates in detail [90, 91, 94, 97–101, 135, 136], while experiments on semiconductor-superconductor hybrids have only established bounds on poisoning from the proximitizing superconductor [72], with quantitative estimates for poisoning from the leads still pending.

In this Letter, we use Coulomb blockade spectroscopy to quantify the quasiparticle poisoning time of a Majorana island. We find that the Majorana island gets excited to a state with one extra quasiparticle in the BCS continuum on a timescale of $\sim$ 3 µs in strongly coupled

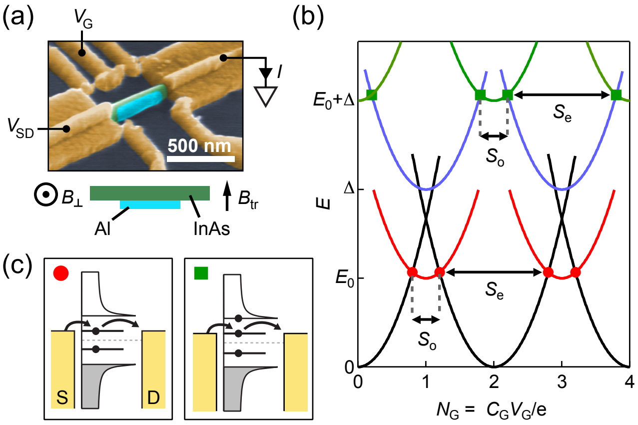

Figure 7.1: (a) Upper panel: Electron micrograph of a lithographically identical Majorana island device with applied bias voltage $V_{\mathrm{SD}}$, gate voltage $V_{\mathrm{G}}$, and measured current $I$. Lower panel: Top-down schematic of the InAs nanowire (green) with epitaxial Al shell (light blue) showing the direction of applied magnetic fields, $B_\perp$ and $B_{\mathrm{tr}}$. (b) Charge state energies $E_{(N_{\mathrm{cp}},N_\Delta,N_0)}$ of the Majorana island as a function of gate induced charge $N_{\mathrm{G}} = C_{\mathrm{G}}V_{\mathrm{G}}/e$. For odd occupation the two lowest avaible energy states are a quasiparticle in the subgap state (red) or the BCS continuum (blue), respectively. For even occupation the two lowest energy states are the BCS condensate (black) and the occupation of both the subgap state and the BCS continuum (green). Transport can occur at degeneracies of charge states, with dominant transitions between ground states indicated by red circles and between excited states by green squares. Coulomb-peak spacings $S_{\mathrm{e}}$ and $S_{\mathrm{o}}$ are indicated by arrows. (c) Schematic of transport processes for degeneracies indicated in (b). Left panel: At values of $N_{\mathrm{G}}$ indicated by red circles, current can flow by successive filling and emptying of the subgap state. Right panel: At degeneracies indicated by green squares, current can flow by successive emptying and filling of the subgap state while another quasiparticle is occupying a continuum state.

regimes, and that it is bounded from below by $\sim 10$ µs in the less strongly coupled regimes investiged in Ref. [42]. Our results demonstrate transport signatures of quasiparticle poisoning in Majorana islands up to the topological phase transition and place constraints on a relevant timescale for topological quantum computation and Majorana braiding schemes.

The devices we investigate consist of an InAs nanowire with epitaxial Al half-shell [Figure 7.1(a)]. Upon deposition of the nanowire, the half-shell is removed on both ends using a chemical etch, leaving an Al island of length $L = 400$ nm in the center. The uncovered InAs segments on both sides are electrically contacted using normal-metal (Ti/Au) ohmic contacts and brought into the tunneling regime using electrostatic gates that were patterned in the same lithography step and control the carrier density in the exposed InAs junction of length $\sim$ 50 nm. Magnetic fields applied out of the chip plane, perpendicular to the nanowire, are denoted as $B_\perp$, and transversal to the nanowire, in the chip plane, are denoted $B_{\mathrm{tr}}$ [Figure 7.1(a) lower panel]. Due to the thin ($\sim$ 10 nm) Al shell on the side of the nanowire, superconductivity in the device is preserved up to high critical fields, $B_{\mathrm{c},\perp} \sim 0.7$ T, in the more favorable perpendicular direction and considerably lower critical fields, $B_{\mathrm{c,tr}} \sim 0.2$ T, in the transversal direction [42, 84]. The emergence of near-zero energy Majorana modes in these nanowires for high parallel and perpendicular fields was reported previously [42]. A bias voltage, $V_{\mathrm{SD}}$, is applied across the device and the chemical potential of the Majorana island can be controlled by applying a voltage to a plunger-gate, $V_{\mathrm{G}}$. The density of states of superconducting hybrid Coulomb islands conforms well to a model of a single subgap state at energy $E_0$ in addition to a Bardeen-Cooper-Schrieffer (BCS) continuum above energy $\Delta$ [42, 72], the hard superconducting gap that is induced in the nanowire due to the epitaxial interface between the superconductor and the semiconductor [79, 84].

## 7.3 ENERGETICS AND TRANSPORT

The total number of charges on the island is $N = 2N_{\mathrm{cp}} + N_\Delta + N_0$, where $N_{\mathrm{cp}}$ denotes the number of Cooper pairs, and $N_0$ and $N_\Delta$ denote the number of quasiparticles in the subgap state and in the BCS continuum, respectively. In the case of high charging energy $E_{\mathrm{C}}$, $N$ is a good quantum number, and the available charge states in the Majorana island can be parameterized by their associated charge occupation numbers $\left(N_{\mathrm{cp}}, N_\Delta, N_0\right)$, with corresponding zero-temperature energies

$$E_{\left(N_{\mathrm{cp}},N_\Delta,N_0\right)} = \frac{E_{\mathrm{C}}}{2}\left(N_{\mathrm{G}} - N\right)^2 + N_\Delta \Delta + N_0 E_0 \tag{7.1}$$

This is shown schematically in Figure 7.1(b) as a function of gate-induced charge, $N_{\mathrm{G}} = C_{\mathrm{G}} V_{\mathrm{G}}/\mathrm{e}$, where e is the electron charge and an even offset charge has been subtracted. For odd $N$, the lowest two available charge states are the occupation of the subgap state, its energy $E_{\left(N_{\mathrm{cp}},0,1\right)}$ shown in red in Figure 7.1(b), followed by the occupation of the BCS continuum [$E_{(N_{\mathrm{cp}},1,0)}$, blue]. For even $N$, the relevant states contributing to transport are the BCS condensate [$E_{(N_{\mathrm{cp}},0,0)}$, black], in addition to an occupation of both the subgap state and the BCS continuum [$E_{(N_{\mathrm{cp}},1,1)}$, green].

We discuss possible transport processes in the Majorana island. While current can flow at any degeneracies of charge states shown in Figure 7.1(b), only some contribute significantly to the total current. In the case of a strongly coupled subgap state, a strong conductance resonance is expected at degeneracies between the BCS condensate and the singly occupied subgap level, which constitute two ground states of the Majorana island. This occurs symmetric around half-integer values of gate-induced charge, $N_{\mathrm{G}}$ [red circles in Figure 1(b)], leading to a Coulomb peak pattern with even and odd peak spacings, $S_{\mathrm{e}} = \eta^{-1}(E_{\mathrm{C}} + 2E_0)$ and $S_{\mathrm{o}} = \eta^{-1}(E_{\mathrm{C}} - 2E_0)$, with gate lever arm $\eta$, that has been reported previously [42,72]. The transport cycle is

$$(N_{\mathrm{cp}},0,0) \rightleftarrows (N_{\mathrm{cp}},0,1)\,, \tag{7.2}$$

at the degeneracy point just below odd $N_{\mathrm{G}}$, where the subgap state is successively emptied and filled, and

$$(N_{\mathrm{cp}},0,1) \rightleftarrows (N_{\mathrm{cp}}+1,0,0)\,, \tag{7.3}$$

at the degeneracy point just above odd $N_{\mathrm{G}}$, where the state is emptied by recombination with another quasiparticle into a Cooper pair. In both cases this constitutes the sucessive emptying and filling of the sub gap state with the BCS continuum unoccupied [Figure 7.1(c), left panel].

Next, we turn our attention towards degeneracies between excited states of the Majorana island. A degeneracy between a charge state with one quasiparticle in the BCS continuum [$E_{(N_{\mathrm{cp}},1,0)}$, blue], and a charge state with one quasiparticle in the BCS continuum and one in the subgap state [$E_{(N_{\mathrm{cp}},1,1)}$, green], occurs symmetrically around even values of $N_{\mathrm{G}}$ [green squares in Figure 7.1(b)]. If these states are populated, for example by quasiparticle poisoning, and if relaxation times are long, this will lead to the transport cycle

$$(N_{\mathrm{cp}},1,0) \rightleftarrows (N_{\mathrm{cp}},1,1) \tag{7.4}$$

at the degeneracy point below even $N_{\mathrm{G}}$, and

$$(N_{\mathrm{cp}},1,1) \rightleftarrows (N_{\mathrm{cp}}+1,1,0)\,, \tag{7.5}$$

at the degeneracy point above even $N_G$. The excited-state transport processes in Equations (7.4) and (7.5) are similar to those between the ground states in Equations (7.2) and (7.3), but the excited states differ by the presence of one long-lived quasiparticle in the BCS continuum. This is schematically shown in the right panel of Figure 7.1(c). Occupation of the charge states $(N_{\text{cp}}, 1, 0)$ or $(N_{\text{cp}}, 1, 1)$ states can either occur by quasiparticle tunneling from the leads, leading to transitions $(N_{\text{cp}}, 0, 0) \rightarrow (N_{\text{cp}}, 1, 0)$, or by Cooper pair breaking, $(N_{\text{cp}} + 1, 0, 0) \rightarrow (N_{\text{cp}}, 1, 1)$.

The relaxation time from continuum to subgap state has been previously quantified as $\tau_{\text{qp}} \sim 0.1$ µs [72], implying that for sufficiently strong coupling of the subgap state to the left and right leads, $\Gamma_{\text{l,r}} \gg \tau_{\text{qp}}^{-1}, \tau_{\text{rec}}^{-1}$, where $\tau_{\text{rec}}$ is the Cooper pair recombination time, many transport cycles can take place before relaxation into the ground state occurs. Notably, Coulomb peaks for this transition are expected to occur at the same peak spacing as in the unpoisoned state, $S_{\text{e,o}}$, but now shifted by 1e in gate voltage [green squares in Figure 7.1(b,c)].

## 7.4 MEASUREMENTS

We investigate possible transport signatures between excited (poisoned) states in a Majorana island strongly coupled to normal metal leads. Measured differential conductance, $g = \mathrm{d}I/\mathrm{d}V_{\text{SD}}$, as a function of $V_{\text{SD}}$ and $V_G$ at zero magnetic field [Figure 7.2(a)], exhibits a high-conductance Coulomb diamond pattern with large even-occupancy diamonds, small odd-occupancy diamonds, and negative differential conductance (NDC) features at finite bias. This has been reported for Majorana islands previously [42, 72]. The nearly vanishing width of the odd diamond implies a subgap state energy $E_0 \lesssim E_C/2$, the energy below which single quasiparticle charging of the device is expected to set in [42, 72, 117, 118].

In addition to the “main"-diamonds with average peak zero-bias conductances of $g_m \sim 0.5$ e$^2$/h, a second much weaker set of “shadow"-diamonds with peak conductances $g_s \sim 0.03$ e$^2$/h is visible inside the center of the even diamond. NDC is also observed for the shadow-diamonds and they appear identical to the main diamonds, except significantly lower in conductance and shifted by a gate voltage corresponding to 1e gate-induced charge, similar to zero-bias signatures of quasiparticle poisoning that have been reported for

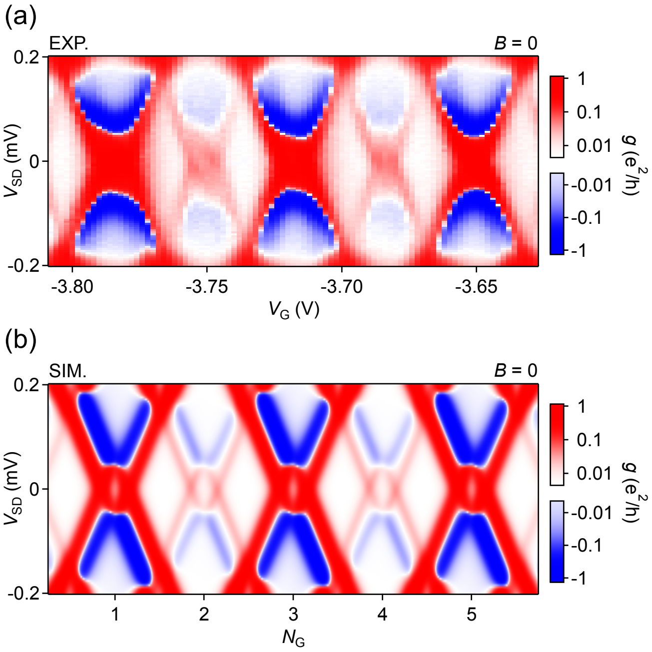

Figure 7.2: (a) Experimental differential conductance $g = \mathrm{d}I/\mathrm{d}V_{\mathrm{SD}}$, on a logarithmic scale as a function of bias voltage $V_{\mathrm{SD}}$ and gate voltage $V_{\mathrm{G}}$, showing a series of Coulomb diamonds at zero magnetic field. A second set of weaker "shadow"-diamonds is visible in the center of the even Coulomb diamond. (b) Transport model of (a) showing calculated differential conductance $g$ as a function of gate-induced charge $N_{\mathrm{G}}$ and source-drain bias. See main text for model parameters.

metallic superconductor islands [121]. The similarity between main and shadow-diamonds, their equal spacing, the 1e shift, and the absence of competing mechanisms that would produce this signature, strongly suggest that the weak shadow-transitions can be identified with the transport cycles in Equations (7.4) and (7.5) [Figure 7.1(b) right panel, Figure 7.1(b) green squares].

From the Coulomb blockade pattern we extract a charging energy $E_{\mathrm{C}} = 208$ µeV, gate lever arm $\eta = 2E_{\mathrm{C}}/\left(\langle S_e\rangle + \langle S_o\rangle\right) = 6.2 \times 10^{-3}$ eV/V, and subgap state energy $E_0 = 75$ µeV. The width and magnitude of the zero-bias conductance resonance taken at a finite field, where peak-overlap is minimal, suggest asymmetric coupling of the subgap state to the left and right leads which we fit as $\Gamma_{\mathrm{l}} \sim 1$ GHz and $\Gamma_{\mathrm{r}} \sim 6$ GHz, significantly stronger than couplings in previous treatments [72].

The relative magnitude of the shadow-peak is expected to be dependent on the rate, $\tau_{\mathrm{p}}^{-1}$, with which quasiparticle tunneling events into the poisoned state occur. In order to get a quantitative estimate of $\tau_\mathrm{p}$, we simulate transport using a rate equation model similar to previous treatments [72]. We base our simulation on the extracted values for $E_\mathrm{C}$, $\eta$, $E_0$, and $\Gamma_\mathrm{l,r}$. Additional required parameters are the lead-continuum conductance $g_\mathrm{Al} \sim 0.7\ \mathrm{e}^2/\mathrm{h}$, estimated from high-bias measurements, the induced superconducting gap, $\Delta = 140\ \mu\mathrm{eV}$, chosen to match the onset of NDC, and the relaxation rate of quasiparticles from the continuum to the subgap state $\tau_\mathrm{qp} = 0.1\ \mu\mathrm{s}$, quantified in previous measurements [72]. We include excitations for even and odd ground states that add a quasiparticle into the BCS continuum, $\left(N_\mathrm{cp}, 0, 0\right) \to \left(N_\mathrm{cp}, 1, 0\right)$ and $\left(N_\mathrm{cp}, 0, 1\right) \to \left(N_\mathrm{cp}, 1, 1\right)$, with rate $\tau_\mathrm{p}^{-1}$, but neglect excitations to the subgap state in our treatment, as they will tunnel out again on timescales set by the larger state-lead coupling, $\Gamma_\mathrm{r}^{-1} \ll \tau_\mathrm{p}$, and not contribute significantly to the current. We also neglect excitations that break a Cooper pair, as we only observe shadow-peaks in tunings where the Majorana island is strongly coupled to the normal metal leads. As Cooper pair breaking would give rise to transitions irrespective of Coupling to the leads, this suggests that quasiparticle tunneling is the dominant source of poisoning events.

The simulated conductance, $g$, as a function of $V_\mathrm{SD}$ and $N_\mathrm{G}$ captures all qualitative features of the observed conductance [Figure 7.2(b)]. The poisoning time $\tau_\mathrm{p} = 2.6\ \mu\mathrm{s}$ gives best agreement with the observed ratio of main and shadow-peak conductance (see below).

## 7.5 MAGNETIC FIELD DEPENDENCE

Experimental zero-bias differential conductance as a function of $V_\mathrm{G}$ and perpendicular magnetic field, $B_\perp$, is shown in Figure 7.3(a). Odd Coulomb valley spacings, $S_\mathrm{o}$, increase in splitting up to a field $B_\perp = 0.16$ T at which average peak spacings are equal, $\langle S_\mathrm{e}\rangle = \langle S_\mathrm{o}\rangle$, indicative of a zero-energy state, $E_0 = 0$. For higher fields, the peak spacings oscillate as a function of magnetic field, consistent with theoretically predicted [45,47,115] and experimentally reported [42,134] signatures of the topological phase transition towards strongly hybridized Majorana modes in Majorana islands. From the near-linear dependence of the peak spacings on $B_\perp$ at lower fields and the condition for evenly spaced peaks $E_0\left(B_\perp\right) = E_0(B_\perp = 0) - E_\mathrm{Z} = 0$, where $E_\mathrm{Z}$ is the Zeeman energy, we extract an effective g-factor of 16, large for InAs [70,123], but consistent with previous measurements on InAs nanowire Coulomb islands [42,134].

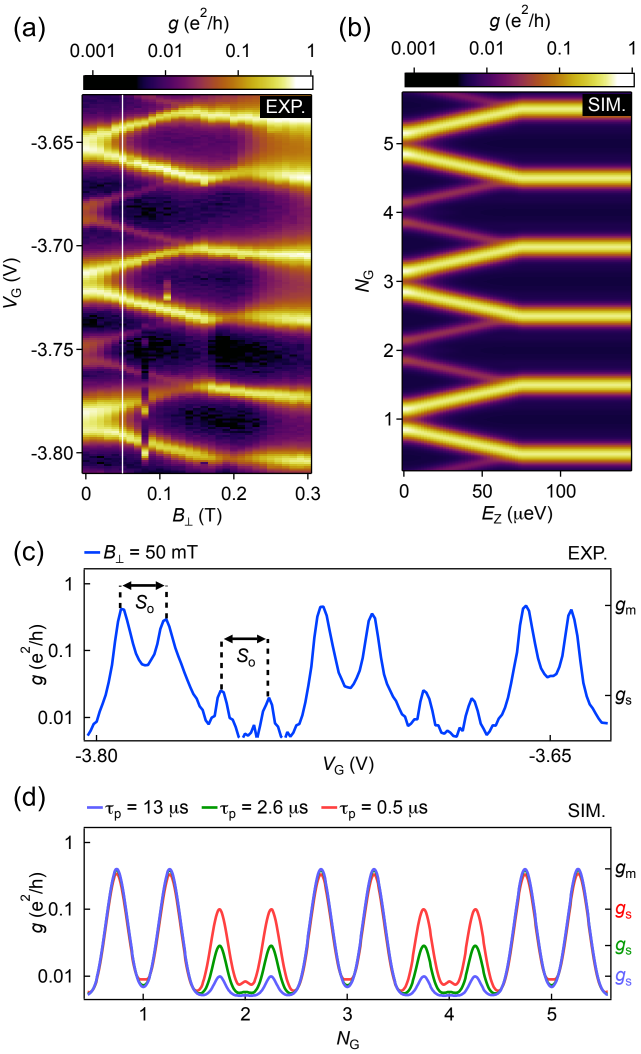

Figure 7.3: (a) Experimental zero-bias differential conductance $g$, as a function of perpendicular magnetic field $B_\perp$, and gate voltage $V_G$, showing a series of strong even-odd Coulomb peaks with fainter shadow peaks in the even Coulomb valley. Both sets of peaks split with increasing magnetic field and merge at $B_\perp \sim 0.16$ T. White line indicates cut in (c). (b) Simulated differential conductance $g$, as a function of Zeeman energy $E_Z$, and gate induced charge $N_G$. (c) Differential conductance $g$, versus gate voltage $V_G$ from measurement in (a) at $B_\perp = 50$ mT. Odd peak spacing, $S_o$, for main and shadow transitions indicated by arrows. Average height of the main and shadow peaks indicated by $g_m$ and $g_s$ respectively. (d) Simulated differential conductance $g$, as a function of gate-induced charge $N_G$ for poisoning times $\tau_p = (13\ \mu s, 2.6\ \mu s, 0.5\ \mu s)$. Simulations show an increase in $g_s$ and decrease in $g_m$ for decreasing $\tau_p$.

The magnetic field dependence of the weak shadow-peaks mirrors that of the main peaks, but shifted by a gate voltage corresponding to 1e gate-induced charge, up to the field $B_\perp = 0.16$ T at which both peaks merge. This field dependence of the shadow peaks is fully consistent with the zero-bias transport model, which predicts that for the special case of $S_\mathrm{e} = S_\mathrm{o}$, i.e. $E_0 = 0$, both poisoned and unpoisoned transitions are expected to occur at the same gate voltage [Figure 7.1(b), overlap of green squares and red circles]. At higher fields, $B_\perp > 0.16$ T, the two sets of peaks cannot be experimentally distinguished anymore.

We extend our model to include the effects of the Zeeman effect by assuming a subgap state energy linearly dependent on magnetic field, $E_0 = 75\ \mu\mathrm{eV} - E_Z$, for $E_Z \leq 75\ \mu\mathrm{eV}$. To take into account the topological phase transition towards a Majorana mode at $E_Z = E_0\ (E_Z = 0)$, which is not directly captured by the rate model, we set $E_0 = 0$ for $E_Z > 75\ \mu\mathrm{eV}$ and neglect Majorana mode hybridization [42, 45, 47].

The simulated zero-bias conductance, $g$, as a function of gate induced charge, $N_G$, and Zeeman energy, $E_Z$, is shown in Figure 7.3(b). Using the same poisoning time $\tau_\mathrm{p} = 2.6\ \mu\mathrm{s}$ as for the simulation in Figure 7.2(b), it captures the observed splitting of the main and shadow peaks for increasing $E_Z$, as well as their merging at $E_Z = 75\ \mu\mathrm{eV}$. A cut of measured $g$ versus $V_G$, taken at the field $B_\perp = 50$ mT, where overlap between adjacent peaks is minimal, is shown in Figure 7.3(c). We define $g_\mathrm{m}$ and $g_\mathrm{s}$ as the average main and shadow-peak conductance in the presented gate range and determine the ratio $g_\mathrm{m}/g_\mathrm{s} \sim 18$.

The simulated differential conductance as a function of $N_G$ at a Zeeman energy $E_Z = 25\ \mu\mathrm{eV}$, corresponding to $B_\perp = 50$ mT, is calculated for three poisoning times $\tau_\mathrm{p} = (13\ \mu\mathrm{s}, 2.6\ \mu\mathrm{s}, 0.5\ \mu\mathrm{s})$ [Figure 7.3(d)]. The simulations reveal a simultaneous increase in $g_\mathrm{s}$ and decrease in $g_\mathrm{m}$ for decreasing $\tau_\mathrm{p}$. The decrease in $g_\mathrm{m}$, de-emphasized by the logarithmic scale in Figure 7.3(d), matches the increase in $g_\mathrm{s}$, reflecting that the Majorana island is either in a poisoned or in an unpoisoned state. For our device-specific parameters, the simulations exhibit a near-linear dependence of poisoning times on peak ratios.

As the shadow peak is expected to grow with decreasing poisoning time, the presented data is not a best-case scenario for the long poisoning times desirable for Majorana qubits. By estimating the maximum ratio $g_\mathrm{m}/g_\mathrm{s}$ from the noise-floor in weakly coupled device tunings, where no shadow-diamonds are observed [42], we place a conservative estimate on the poisoning time of $\tau_\mathrm{p} > 10\ \mu\mathrm{s}$.

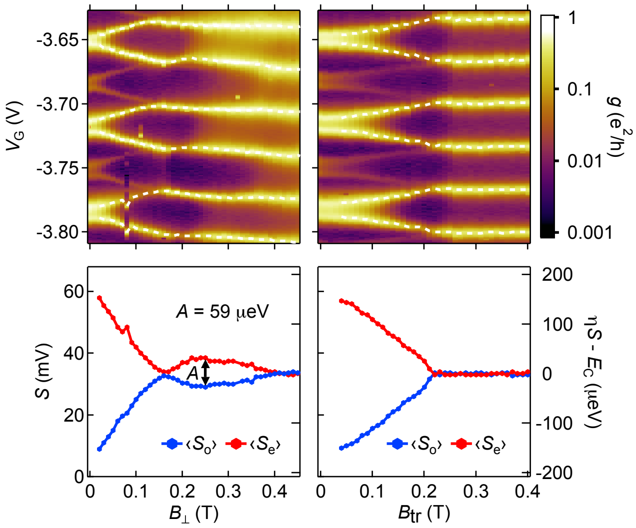

Figure 7.4: Upper panels: Differential conductance $g$, as a function of gate voltage $V_G$ and magnetic fields perpendicular ($B_\perp$, left) and transversal ($B_{tr}$, right) to the nanowire. The fit peak positions are overlaid by dashed white lines. Lower panels: Extracted average peak spacing for even and odd Coulomb valleys, $\langle S_{e,o} \rangle$, as a function of $B_\perp$ (left panel) and $B_{tr}$ (right panel). The left axis gives the peak spacing in units of gate voltage, the right axis shows the associated energy scale $\eta S - E_C \propto E_0$. For a perpendicular field of $B_\perp = 0.16$ T, peaks reach the even spacing $\langle S_e \rangle = \langle S_o \rangle$. For higher fields peak spacings oscillate with maximum energy amplitude $A = 59$ μeV. For transversal fields, $\langle S_e \rangle = \langle S_o \rangle$ at $B_{tr} = 0.22$ T, with no observed high field oscillations in the peak spacing.

Finally, we investigate the behavior of shadow-peaks and main-peaks in different magnetic field directions. The magnetic-field dependent splitting is compared for directions $B_\perp$ and $B_{tr}$ in Figure 7.4. In both cases, the estimated peak center, indicated by a dashed white line in the upper panels of Figure 7.4, is used to calculated average Coulomb peak spacings for the two even and the three odd valleys of the main set of Coulomb peaks, denoted $\langle S_e \rangle$ and $\langle S_o \rangle$. This is shown in the lower panels of Figure 7.4, where the right axis indicates the energy scale for the lowest subgap state $\eta S - E_C \propto E_0$. The shadow-peak is not used in this analysis as it cannot be distinguished from the main peak for higher fields.

For increasing perpendicular fields, $B_\perp$, even and odd valley spacings increase and become uniformly spaced $\langle S_e \rangle = \langle S_o \rangle$ at $B_\perp = 0.16$ T, indicating the emergence of a state at $E_0 = 0$, and subsequently oscillate in magnetic field. The energy oscillation amplitude of the peak spacing, $A = 59$ µeV, is close to the expected value for hybridized Majorana modes in a device with $L = 400$ nm, $A = A_0 e^{-L/\xi} = 64$ µeV, based on previous fits of constants $A_0 = 300$ µeV and $\xi = 260$ nm [42]. We stress that data from the same device showing $A = 60$ µeV, but measured in a different tuning without shadow-peaks, which were not fully understood at the time, was included in the original analysis to determine $A_0$ and $\xi$ [42].

For increasing transversal fields, $B_{\mathrm{tr}}$, shadow peaks split similar to the main peaks, and the spacing becomes 1e periodic at $B_{\mathrm{tr}} = 0.22$ T, with no oscillations visible for higher fields [Fig 7.4, right panels]. Independent measurements show a closing of the superconducting gap for this device at $B_{\mathrm{c,tr}} = 0.25$ T, suggesting that the transition towards 1e periodic peak spacings for transversal magnetic fields is dominated by a quenching of $E_0$ as superconductivity is destroyed. This interpretation is supported by the different curvatures of $\langle S_{\mathrm{e,o}} \rangle$ as they approach the field when $\langle S_{\mathrm{e}} \rangle = \langle S_{\mathrm{o}} \rangle$, with $\langle S_{\mathrm{e,o}} \rangle$ bending outwards for $B_\perp$ and inwards for $B_{\mathrm{tr}}$. Since $\eta \langle S_{\mathrm{e}} \rangle - E_{\mathrm{C}} \propto E_0$ and $\eta \langle S_{\mathrm{o}} \rangle - E_{\mathrm{C}} \propto -E_0$, the outwards bending behavior for $B_\perp$ is in line with theoretical models for subgap states approaching the topological phase transition towards a Majorana mode [45,47,49]. In contrast, the two curves bending inwards for increasing $B_{\mathrm{tr}}$ is consistent in a simple picture that approximates the lowest state energy as proportional to the quadratically closing induced superconducting gap.

## 7.6 CONCLUSION

In conclusion, we have measured and modeled transport signatures of quasiparticle poisoning in a Majorana island. Zero-field measurements reveal an even-odd Coulomb diamond pattern in addition to a second set of weaker shadow-diamonds, associated with quasiparticle poisoning of the Majorana island. The field-dependence exhibits a merging of main and shadow-peaks, an effect that to our best knowledge has so far not been reported in the scientific literature. The good agreement between experiment and model suggests poisoning times $\tau_{\mathrm{p}} = 2.6$ µs for the presented device and $\tau_{\mathrm{p}} > 10$ µs for devices in which this effect is absent. High field measurements indicate a transition to the topological phase, with extracted Majorana mode hybridization energies consistent with previous measurements.

Part V

# PEAK SKEWS

# 8

# ANALYSIS OF PEAK SKEWS IN A MAJORANA ISLAND

Published results based on measurements in Majorana islands [72], reported in Chapter 5, observed that Coulomb peak centroids were not identical with Coulomb peak maxima. Moreover, it was found that Coulomb peaks were systematically skewed towards the even Coulomb valley for an $L = 310$ nm device, as shown in Figure 5.3c.

Subsequent theoretical work proposed an explanation for this effect [133], based on elastic cotunneling via a virtual state in the Majorana island. This prompted a more thorough analysis of earlier datasets with respect to the presence of peak skews and their systematic dependence on magnetic field and subgap state energy, which is presented in this chapter. Although the results are still inconclusive, and in some cases opposite to the findings in Chapter 5, they might contribute to an understanding of this effect.

## 8.1 DEFINITION

Our treatment attempts to present a simple, intuitive, and model-blind analysis of peak skews. For the sake of simplicity, we will not be resorting to statistical measures of skewness, such as Pearson's moment coefficient. This could, however, be implemented in more elaborate investigations of peak skews in future work.

We define the integrated conductance on the right and left side of a Coulomb peak as

$$G_r = \int_{V_{\text{peak}}}^{V_{\text{peak}}+\delta} g\left(V_G\right) \mathrm{d}V_G, \qquad G_l = \int_{V_{\text{peak}}-\delta}^{V_{\text{peak}}} g\left(V_G\right) \mathrm{d}V_G \qquad (8.1)$$

where $V_{\text{peak}}$ is the peak position in gate voltage and $\delta$ is the gate interval on the left and right side of the peak that is integrated over. This is shown for a sample peak in Figure 8.1. For the following analysis we will pick $\delta = 2\langle\text{FWHM}\rangle$, where $\langle\text{FWHM}\rangle$ is the average full width at half maximum for all the peaks in a single measurement of $g$ as a function of $V_G$ at zero-bias and fixed magnetic field. We stress that this is an arbitrary, but useful, choice that captures most of the peak

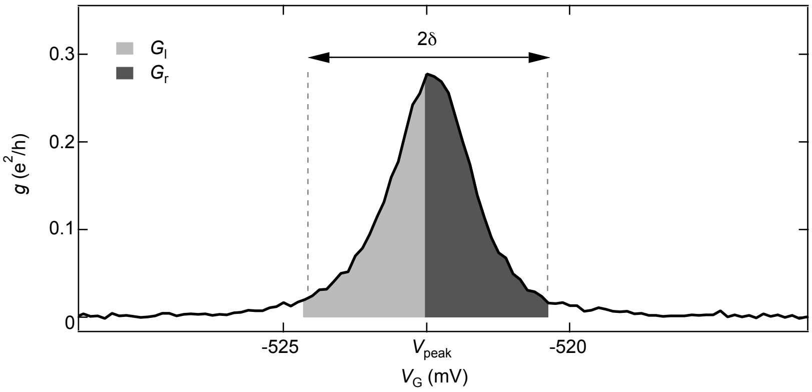

Figure 8.1: **Calculation of peak skews.** Schematic showing differential conductance $g$ as a function of gate voltage $V_\mathrm{G}$ for a single peak. The conductance is integrated over a region of $\pm\delta$ around the peak maximum to determine $G_\mathrm{l}$ (light gray) and $G_\mathrm{r}$ (dark gray). Skews are calculated according to $R = (G_\mathrm{r} - G_\mathrm{l}) \,/\, (G_\mathrm{r} + G_\mathrm{l})$. For the analysis, $\delta$ has been chosen as twice the average full width at half maximum of all the peaks in a single gate trace (not shown to scale in figure).

area, including its skew, and little of the conductance background in the adjacent Coulomb valley.

Next, we define the normalized peak skew, $R$, as

$$R = \frac{G_\mathrm{r} - G_\mathrm{l}}{G_\mathrm{r} + G_\mathrm{l}}. \tag{8.2}$$

It is a measure of how much a peak is skewed towards the right, higher gate voltage side, with positive $R$ indicating a skew to the right, and negative $R$ indicating a skew to the left. We further separate the set of Coulomb peaks into those on the left side of an odd valley, which we will refer to as e→o peaks, and those on the right side of an odd valley, which we denote o→e peaks (see below).

## 8.2 MAGNETIC FIELD DEPENDENCE

A measurement of Coulomb peaks taken at a magnetic field of $B_{||} = 140$ mT for an $L = 790$ nm Majorana island device is shown in Figure 8.2a. The measurement shows a clear alternation of low-conductance e→o and high-conductance o→e Coulomb peaks, an effect that is currently not understood. In addition to the alternating conductance intensities, the normalized peak skew $R$, shown in Figure 8.2b, alternates between more and less right-skewed peaks, with $R_{\mathrm{e}\to\mathrm{o},N} > R_{\mathrm{o}\to\mathrm{e},N}$ for nearly all $N$, where $N$ is the index of the odd valley that is framed by the e→o and the o→e peak. We note that

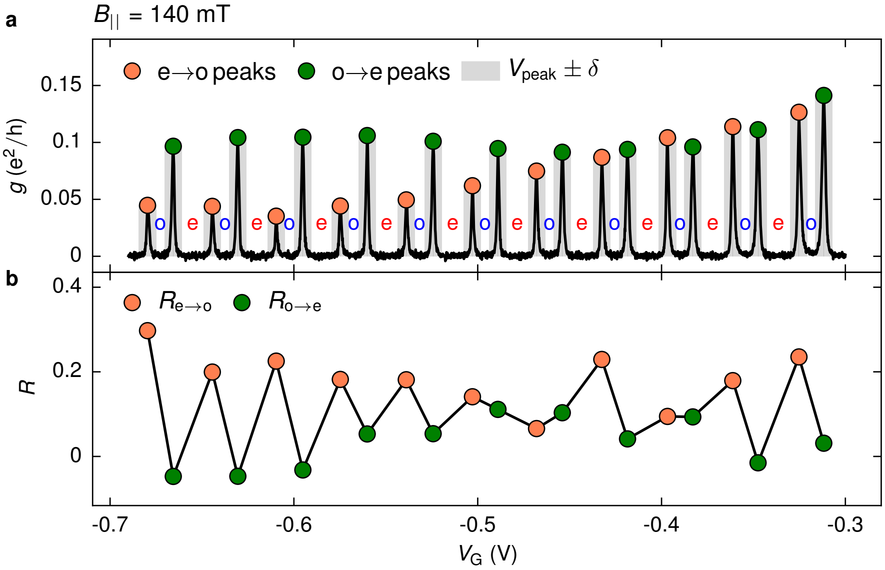

Figure 8.2: **Peak skews for $B_{||} = 140$ mT. a,** Differential conductance $g$, as a function of gate voltage $V_G$, for the $L = 790$ nm device. Even and odd valleys are indicated by red and blue labels, extracted peak positions for e→o and o→e peaks are indicated by orange and green circles, respectively. **b,** Calculated peak skew, $R$, for e→o and o→e peaks as a function of $V_G$, showing an alternating pattern of high $R_{e\to o}$ and low $R_{o\to e}$.

there is a single outlier at $V_G \sim -0.47$ mV, that does not change the parity of the whole measurement. We also observe that most $R > 0$, which implies that all Coulomb peaks are systematically skewed to the right side. We suspect that this is a measurement artifact, either caused by measuring too fast on our lockin amplifier, or because the applied bias voltage was not perfectly zero during the measurement. We will substantiate this interpretation below.

As at this particular magnetic field odd valleys are smaller than even valleys, owing to a state energy $0 < E_0 < E_C/2$, potential artifacts could be introduced in the extraction of the peak skew if the analysis would take into account a peak overlap in the center of the odd valley. We explicitly verify that this is not the case by plotting the $V_{peak} \pm \delta$ area used in the analysis as a gray box in Figure 8.2a and determine that none of the peaks overlap in the area of integration.

The individual Coulomb peaks, normalized to their respective maximum $g_{max}$, belonging to the e→o and o→e sets for $B_{||} = 140$ mT are shown in Figure 8.3. The average (black overlay) shows a tendency of the e→o peaks to bend towards the odd (right) valley, as expected from the consistently higher values of $R_{e\to o}$ in Figure 8.2b.

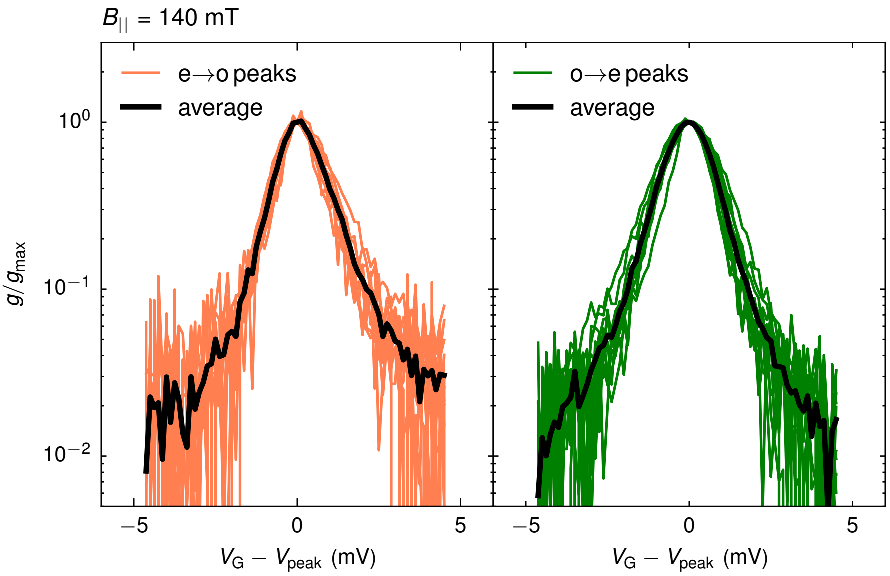

Figure 8.3: **Peak shapes for $B_{||} = 140$ mT.** Differential conductance $g$, for each individual peak as a function of gate voltage centered around the peak maximum $V_\mathrm{G} - V_\mathrm{peak}$, for the $L = 790$ nm device. Left panel shows individual e→o peaks (orange), right panel shows individual o→e peaks (green). The average is shown in black.

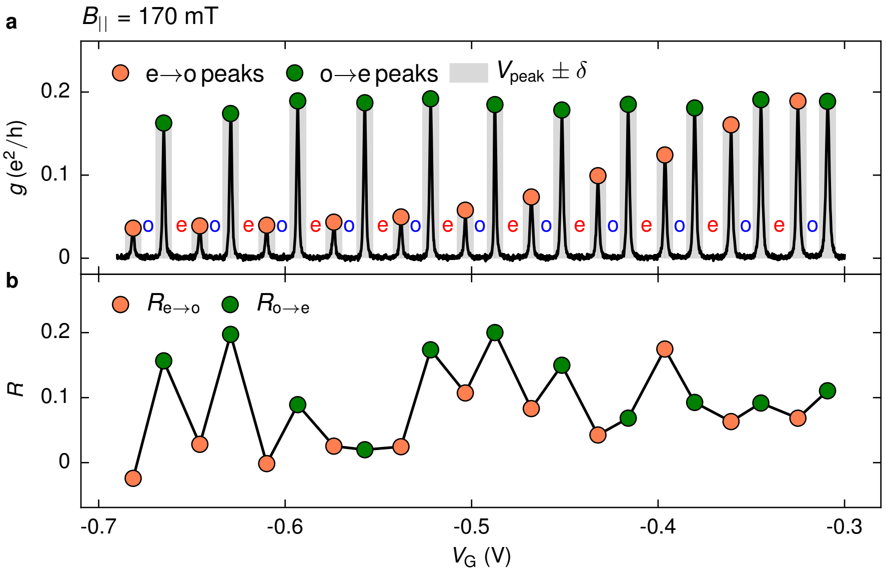

Figure 8.4: **Peak skews for $B_{||} = 170$ mT. a,** Coulomb peaks. **b,** Peak skew, $R$, featuring an alternating pattern of low $R_{\mathrm{e}\to\mathrm{o}}$ and high $R_{\mathrm{o}\to\mathrm{e}}$, opposite to the pattern observed for $B_{||} = 140$ mT.

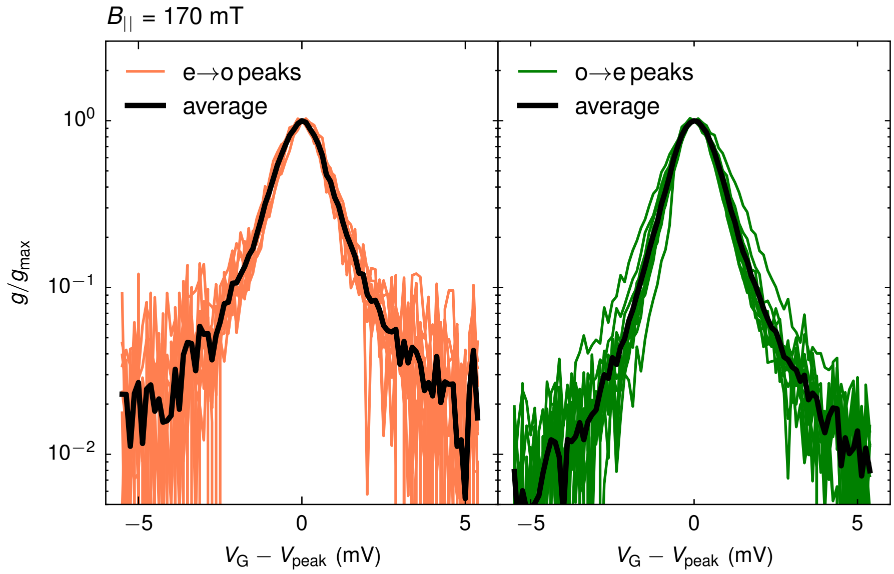

Figure 8.5: **Peak shapes for** $B_{||} = 170$ **mT.**

We compare this to the identical analysis for a cut at $B_{||} = 170$ mT, shown in Figure 8.4a, which was measured on the same set of Coulomb peaks. Coulomb peak intensities vary again, with low o→e peak conductance and high e→o peak conductance, as was the case for the $B_{||} = 140$ mT measurement. The calculated normalized peak skew, $R$, for $B_{||} = 170$ mT (Figure 8.4b) exhibits an alternating pattern that looks superficially similar to the $B_{||} = 140$ mT measurement. We note, however, that in this case e→o transitions have lower $R$ than their neighboring o→e transitions, $R_{\mathrm{e}\to\mathrm{o},N} < R_{\mathrm{o}\to\mathrm{e},N}$, with the exception of two outliers at $V_G = -0.55, -0.4$ V. This constitutes a phase slip, compared to $B_{||} = 140$ mT, where $R_{\mathrm{e}\to\mathrm{o},N} > R_{\mathrm{o}\to\mathrm{e},N}$. Individual and average peak shapes for $B_{||} = 170$ mT, shown in Figure 8.5 exhibit a clear tail of the o→e peaks towards the even (right) valley, as expected from Figure 8.4b. Moreover, we note that while the skew direction for e→o and o→e peaks changed as we increased the magnetic field, the relative height of conductance peaks did not (e→o peaks are lower for both fields). This suggests that these two effects are not related.

We find yet another phase slip at a higher field, $B_{||} = 235$ mT, shown in Figure 8.6b, where $R_{\mathrm{e}\to\mathrm{o},N} > R_{\mathrm{o}\to\mathrm{e},N}$ for all $N$, except for the last two Coulomb valleys. Both sets of peaks have a tendency to skew more towards the odd side, which is confirmed by the individual peak shapes shown in Figure 8.7.

We turn our attention to the full two-dimensional dataset of the $L = 790$ nm Majorana island from which the cuts in Figures 8.2a-

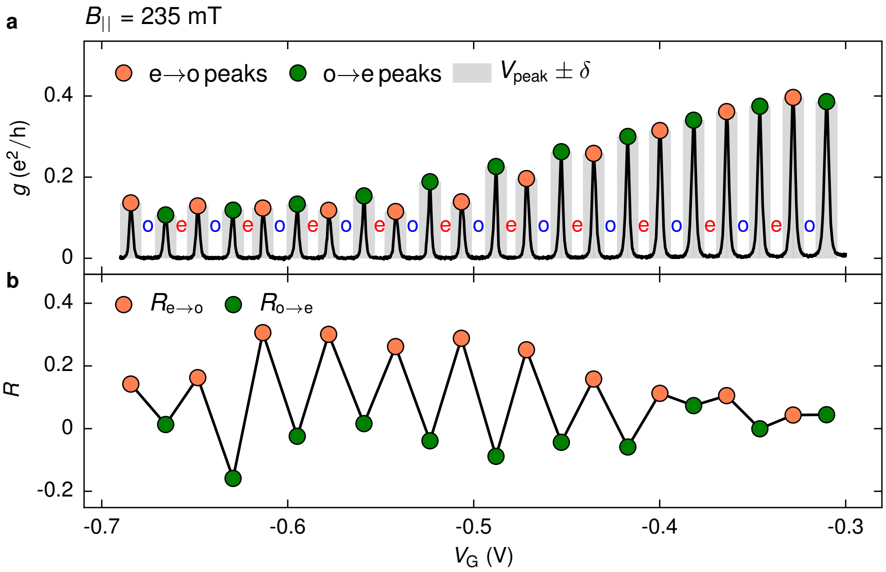

Figure 8.6: **Peak skews for $B_{||} = 235$ mT. a,** Coulomb peaks. **b,** Peak skew, $R$, featuring an alternating pattern of high $R_{e\to o}$ and low $R_{o\to e}$, opposite to the pattern observed for $B_{||} = 170$ mT.

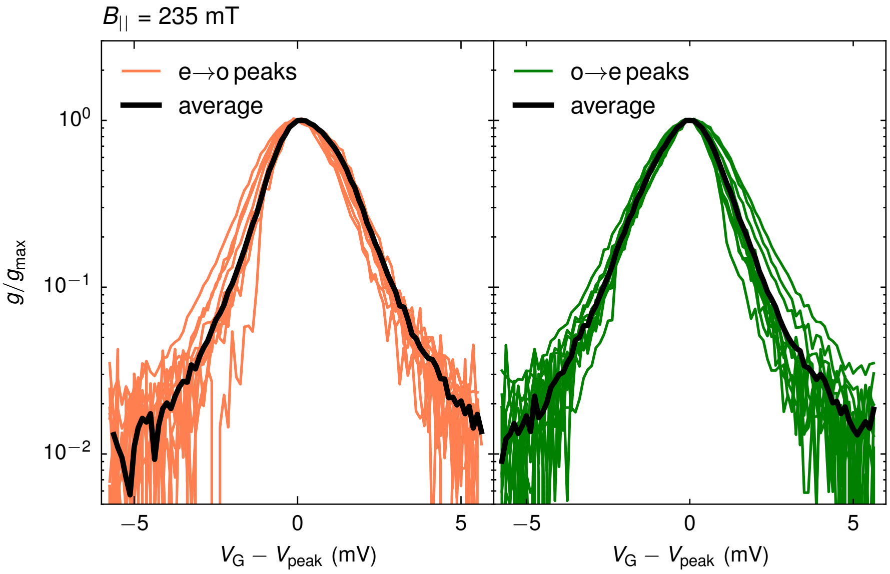

Figure 8.7: **Peak shapes for $B_{||} = 235$ mT.**

8.7a were extracted. The measured differential conductance at zero bias is shown as a function of $V_G$ and $B_{||}$ in Figure 8.8a. It shows 2e periodic Coulomb peaks at $B = 0$, that split in an applied magnetic field, as reported before for Majorana islands [42], see Chapter 6. The extracted average peak spacing for even and odd Coulomb diamonds, $\langle S_e \rangle$ and $\langle S_o \rangle$ shown in 8.8b, reveals oscillations around the value $\langle S_e \rangle = \langle S_o \rangle$, as expected for hybridized Majorana modes.

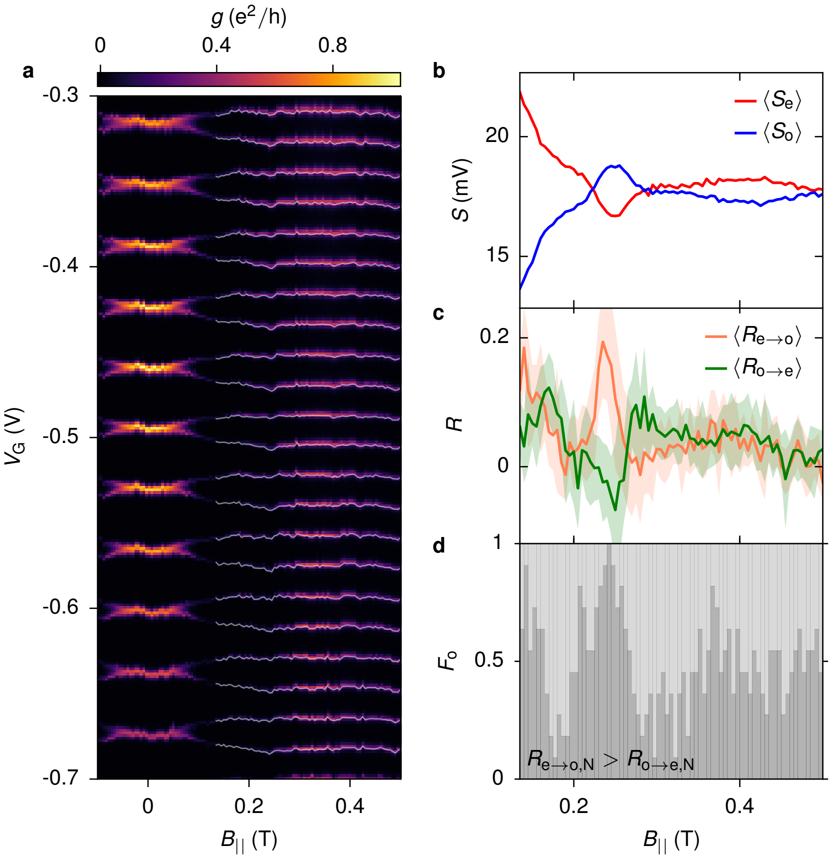

Figure 8.8: **Peak skews in parallel magnetic field. a**, Differential conductance $g$, as a function of gate voltage $V_G$, and parallel magnetic field $B_{||}$. White lines show fit peak positions. **b,** Calculated average peak spacings $\langle S_{e,o} \rangle$ for even and odd Coulomb valleys as a function of $B_{||}$. **c,** Calculated average normalized peak skew for e→o and o→e peaks, $\langle R_{e \to o} \rangle$ and $\langle R_{o \to e} \rangle$, showing oscillations as a function of $B_{||}$. Standard deviation is plotted as shaded area behind the data. **d,** Fraction of e→o peaks that have $R_{e \to o,N} > R_{o \to e,N}$, where $N$ is the Coulomb valley framed by both peaks.

Extending our skew analysis to the magnetic field range $140 - 500$ mT in Figure 8.8a, the average extracted peak skew for e→o and o→e peaks, $\langle R_{e \to o} \rangle$ and $\langle R_{o \to e} \rangle$, plotted against magnetic field $B_{||}$ in Figure 8.8c, shows three peak skew phase slips, where $\langle R_{e \to o} \rangle - \langle R_{o \to e} \rangle$ changes sign. Interestingly, a comparison with Figure 8.8b suggests that phase slips in skew are occurring at "kinks" in the peak spacings, i.e. at magnetic fields where $\frac{d^2 S}{d B_{||}^2} \neq 0$.

We plot the calculated statistical error on the mean as the shaded region behind the line in Figure 8.8c. Due to the large spread in $R_{e \to o}$

and $R_{\mathrm{o}\to\mathrm{e}}$ in a single measurement (see Figures 8.2b, 8.4b, 8.6b), this error is not a good estimate of how well $R$ preserves its alternating up-down or down-up pattern between e→o and o→e peaks. Even for a perfectly alternating pattern, a steady increase in individual $R$ values will significantly increase the error on the mean. To get a better estimate, we calculate the fraction $F_\mathrm{o}$ of odd Coulomb valleys for which the surrounding peaks feature a skew $R_{\mathrm{e}\to\mathrm{o},N} > R_{\mathrm{o}\to\mathrm{e},N}$. For a completely random distribution we would therefore expect $F_\mathrm{o} = 0.5$, whereas in the case of $R_{\mathrm{e}\to\mathrm{o},N} > R_{\mathrm{o}\to\mathrm{e},N}$ for all Coulomb valleys $F_\mathrm{o} = 1$. The quantity $F_\mathrm{o}$ is therefore a measure of how good $R$ preserves its up-down alternating parity. The calculated fraction, shown in Figure 8.8d, shows oscillations, with $F_\mathrm{o} \sim 1$ at $B_{||} = 140,\ 235$ mT and $F_\mathrm{o} \sim 0$ for $B_{||} = 170,\ 300$ mT.

We compare these results to an identical analysis for the same set of Coulomb peaks, but measured as a function of a magnetic field pointing in the low-critical field transversal direction $B_{\mathrm{tr}}$, which is shown in Figure 8.9a. Peak spacings (Figure 8.9b) approach their even spacing $\langle S_\mathrm{e} \rangle = \langle S_\mathrm{o} \rangle$ at $B_{\mathrm{tr,c}} \sim 120$ mT, with no further oscillations at higher magnetic fields. This is consistent with the closing of the energy gap as superconductivity is destroyed in the device. The calculated average peak skew, shown in Figure 8.9c, shows $\langle R_{\mathrm{e}\to\mathrm{o}} \rangle > \langle R_{\mathrm{o}\to\mathrm{e}} \rangle$ for fields below the superconducting-to-normal transition and $\langle R_{\mathrm{e}\to\mathrm{o}} \rangle = \langle R_{\mathrm{o}\to\mathrm{e}} \rangle$ for $B_{\mathrm{tr}} > B_{\mathrm{tr,c}}$ when the device is in the metallic state. Likewise, $F_\mathrm{o}$ is statistically distributed around the value $F_\mathrm{o} \sim 0.5$ for for $B_{\mathrm{tr}} > B_{\mathrm{tr,c}}$, as seen in Figure 8.9d.

## 8.3 CONCLUSION

The absence of peak skew differences between e→o and o→e peaks, i.e. $\langle R_{\mathrm{e}\to\mathrm{o}} \rangle = \langle R_{\mathrm{o}\to\mathrm{e}} \rangle$, as superconductivity is destroyed supports our assumption that $R$ values do not scatter symmetrically around $R = 0$, due to a systematic error resulting from the measurement. The absence of oscillations in the peak skew for the non-superconducting regime, whereas oscillations are clearly present for $B_{||}$, also implies that a causal relationship between peak skew and subgap state energetics exists. Moreover, in an applied parallel magnetic field phase slips in the skew direction correlate with changes in the subgap state energy. This effect is currently not understood, but will be the subject of future work.

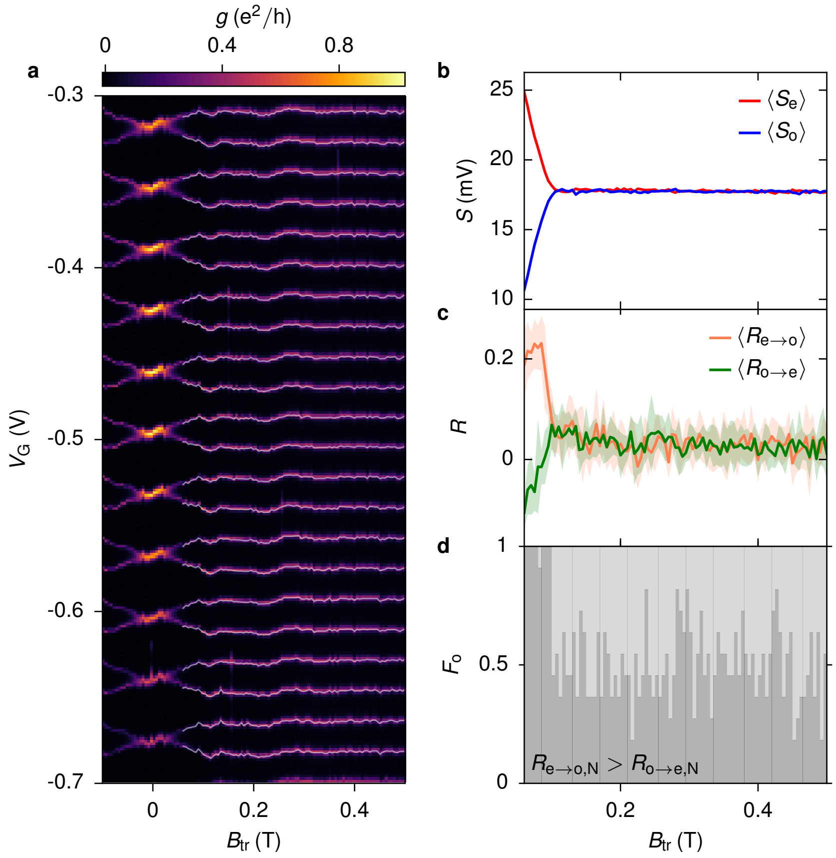

Figure 8.9: **Peak skews in transversal magnetic field.** **a**, Coulomb peaks split in a transversal magentic field. **b,** No oscillations in peak spacings $S$ are visible as the device is driven into the normal state at $B_{\text{tr,c}} \sim 120$ mT. **c,** Peaks feature an alternating skew pattern at low fields, but no oscillations in skew are distinguishable after the superconducting to normal transition. **d,** While the calculated peak skew is nearly perfectly alternating for most measurements below the transition to the normal state, it is statistically distributed around the value $F_o \sim 0.5$ after superconductivity is destroyed.

# BIBLIOGRAPHY

[1] R. P. Feynman, "Simulating Physics with Computers," *International Journal of Theoretical Physics*, vol. 21, no. 6, pp. 467–488, Jun. 1982.

[2] P. W. Shor, "Polynomial-Time Algorithms for Prime Factorization and Discrete Logarithms on a Quantum Computer." *SIAM J. Comput.*, vol. 26, no. 5, pp. 1484–1509, 1997.

[3] L. K. Grover, "A Fast Quantum Mechanical Algorithm for Database Search." *STOC*, pp. 212–219, 1996.

[4] I. M. Georgescu, S. Ashhab, and F. Nori, "Quantum simulation," *Reviews of Modern Physics*, vol. 86, no. 1, pp. 153–185, Jan. 2014.

[5] A. B. Finnila, M. A. Gomez, C. Sebenik, C. Stenson, and J. D. Doll, "Quantum annealing: A new method for minimizing multidimensional functions," *Chemical Physics Letters*, vol. 219, no. 5-6, pp. 343–348, Mar. 1994.

[6] E. Farhi, J. Goldstone, S. Gutmann, J. Lapan, A. Lundgren, and D. Preda, "A Quantum Adiabatic Evolution Algorithm Applied to Random Instances of an NP-Complete Problem," *Science*, vol. 292, no. 5516, pp. 472–475, Apr. 2001.

[7] B. Heim, T. F. Rønnow, S. V. Isakov, and M. Troyer, "Quantum versus classical annealing of Ising spin glasses," *Science*, vol. 348, no. 6231, pp. 215–217, Apr. 2015.

[8] D. Kielpinski, C. Monroe, and D. J. Wineland, "Architecture for a large-scale ion-trap quantum computer," *Nature*, vol. 417, no. 6, pp. 709–711, Jun. 2002.

[9] C. F. Roos, M. Riebe, H. Häffner, W. Hänsel, J. Benhelm, G. P. T. Lancaster, C. Becher, F. Schmidt-Kaler, and R. Blatt, "Control and Measurement of Three-Qubit Entangled States," *Science*, vol. 304, no. 5676, pp. 1478–1480, Jun. 2004.

[10] E. Knill, R. Laflamme, and G. J. Milburn, "A scheme for efficient quantum computation with linear optics," *Nature*, vol. 409, no. 6816, pp. 46–52, Jan. 2001.

[11] J. J. L. Morton, A. M. Tyryshkin, R. M. Brown, S. Shankar, B. W. Lovett, A. Ardavan, T. Schenkel, E. E. Haller, J. W. Ager, and S. A. Lyon, "Solid-state quantum memory using the 31P nuclear spin," *Nature*, vol. 455, no. 7216, pp. 1085–1088, Oct. 2008.

[12] Y. Nakamura, Y. A. Pashkin, and J. S. Tsai, "Coherent control of macroscopic quantum states in a single-Cooper-pair box," *Nature*, vol. 398, no. 6, pp. 786–788, Apr. 1999.

[13] M. H. Devoret, A. Wallraff, and J. M. Martinis, "Superconducting Qubits: A Short Review," *arXiv.org*, Nov. 2004.

[14] M. H. Devoret and R. J. Schoelkopf, "Superconducting circuits for quantum information: an outlook." *Science*, vol. 339, no. 6124, pp. 1169–1174, Mar. 2013.

[15] J. R. Petta, A. C. Johnson, J. M. Taylor, E. A. Laird, A. Yacoby, M. D. Lukin, C. M. Marcus, M. P. Hanson, and A. C. Gossard, "Coherent manipulation of coupled electron spins in semiconductor quantum dots," *Science*, vol. 309, no. 5744, pp. 2180–2184, 2005.

[16] A. Y. Kitaev, "Fault-tolerant quantum computation by anyons," *Annals of Physics*, vol. 303, no. 1, pp. 2–30, Jan. 2003.

[17] C. Nayak, S. H. Simon, A. Stern, M. Freedman, and S. Das Sarma, "Non-Abelian anyons and topological quantum computation," *Reviews of Modern Physics*, vol. 80, no. 3, pp. 1083–1159, Sep. 2008.

[18] W. K. Wootters and W. H. Zurek, "A single quantum cannot be cloned," *Nature*, vol. 299, no. 5886, p. 802, Oct. 1982.

[19] R. Barends, J. Kelly, A. Megrant, A. Veitia, D. Sank, E. Jeffrey, T. C. White, J. Mutus, A. G. Fowler, B. Campbell, Y. Chen, Z. Chen, B. Chiaro, A. Dunsworth, C. Neill, P. O'Malley, P. Roushan, A. Vainsencher, J. Wenner, A. N. Korotkov, A. N. Cleland, and J. M. Martinis, "Superconducting quantum circuits at the surface code threshold for fault tolerance," *Nature*, vol. 508, no. 7, pp. 500–503, Apr. 2014.

[20] P. W. Shor, "Scheme for reducing decoherence in quantum computer memory," *Physical Review A*, vol. 52, no. 4, pp. R2493–R2496, Oct. 1995.

[21] A. G. Fowler, M. Mariantoni, J. M. Martinis, and A. N. Cleland, "Surface codes: Towards practical large-scale quantum computation," *Physical Review A*, vol. 86, no. 3, p. 032324, Sep. 2012.

[22] A. Y. Kitaev, "Unpaired Majorana fermions in quantum wires," *Phys.Usp.*, vol. 44, no. 10S, pp. 131–136, 2001.

[23] N. Read and D. Green, "Paired states of fermions in two dimensions with breaking of parity and time-reversal symmetries and the fractional quantum Hall effect," *Physical Review B*, vol. 61, no. 15, pp. 10 267–10 297, 2000.

[24] D. Rainis and D. Loss, "Majorana qubit decoherence by quasiparticle poisoning," *Physical Review B*, vol. 85, no. 17, p. 174533, 2012.

[25] L. P. Kouwenhoven, C. M. Marcus, P. L. McEuen, S. Tarucha, R. M. Westervelt, and N. S. Wingreen, "Electron Transport in Quantum Dots," in *Mesoscopic Electron Transport*. Dordrecht: Springer Netherlands, 1997, pp. 105–214.

[26] S. De Franceschi, L. Kouwenhoven, C. Schoenenberger, and W. Wernsdorfer, "Hybrid superconductor-quantum dot devices," *Nature Nanotechnology*, vol. 5, no. 10, pp. 703–711, Oct. 2010.

[27] D. Aasen, M. Hell, R. V. Mishmash, A. Higginbotham, J. Danon, M. Leijnse, T. S. Jespersen, J. A. Folk, C. M. Marcus, K. Flensberg, and J. Alicea, "Milestones Toward Majorana-Based Quantum Computing," *Physical Review X*, vol. 6, no. 3, p. 031016, Aug. 2016.

[28] S. Vijay and L. Fu, "Braiding without Braiding: Teleportation-Based Quantum Information Processing with Majorana Zero Modes," *arXiv.org*, Sep. 2016.

[29] L. A. Landau, S. Plugge, E. Sela, A. Altland, S. M. Albrecht, and R. Egger, "Towards Realistic Implementations of a Majorana Surface Code," *Physical Review Letters*, vol. 116, no. 5, p. 050501, Feb. 2016.

[30] M. Leijnse and K. Flensberg, "Introduction to topological superconductivity and Majorana fermions," *Semiconductor Science and Technology*, vol. 27, no. 12, p. 124003, 2012.

[31] C. W. J. Beenakker, "Search for Majorana Fermions in Superconductors," *Annual Review of Condensed Matter Physics*, vol. 4, no. 1, pp. 113–136, Apr. 2013.

[32] E. Majorana, "Teoria simmetrica dell'elettrone e del positrone," *Il Nuovo Cimento*, vol. 14, no. 4, pp. 171–184, Apr. 1937.

[33] H. Weyl, "Elektron und Gravitation. I," *Zeitschrift für Physik*, vol. 56, no. 5-6, pp. 330–352, 1929.

[34] F. Wilczek, "Majorana returns," *Nature Physics*, vol. 5, no. 9, pp. 614–618, Sep. 2009.

[35] B. R. Holstein, "The mysterious disappearance of Ettore Majorana," *Journal of Physics: Conference Series*, vol. 173, no. 1, p. 012019, Jun. 2009.

[36] T. Senthil and M. P. A. Fisher, "Quasiparticle localization in superconductors with spin-orbit scattering," *Physical Review B*, vol. 61, no. 14, pp. 9690–9698, Apr. 2000.

[37] R. M. Lutchyn, J. D. Sau, and S. Das Sarma, "Majorana Fermions and a Topological Phase Transition in Semiconductor-Superconductor Heterostructures," *Physical Review Letters*, vol. 105, no. 7, p. 077001, Aug. 2010.

[38] Y. Oreg, G. Refael, and F. von Oppen, "Helical Liquids and Majorana Bound States in Quantum Wires," *Physical Review Letters*, vol. 105, no. 17, p. 177002, Oct. 2010.

[39] V. Mourik, K. Zuo, S. M. Frolov, S. R. Plissard, E. Bakkers, and L. P. Kouwenhoven, "Signatures of Majorana fermions in hybrid superconductor-semiconductor nanowire devices," *Science*, vol. 336, no. 6084, pp. 1003–1007, 2012.

[40] A. Das, Y. Ronen, Y. Most, Y. Oreg, M. Heiblum, and H. Shtrikman, "Zero-bias peaks and splitting in an Al-InAs nanowire topological superconductor as a signature of Majorana fermions," *Nature Physics*, vol. 8, no. 12, pp. 887–895, Dec. 2012.

[41] M. T. Deng, C. L. Yu, G. Y. Huang, M. Larsson, P. Caroff, and H. Q. Xu, "Anomalous Zero-Bias Conductance Peak in a Nb–InSb Nanowire–Nb Hybrid Device," *Nano Letters*, vol. 12, no. 12, pp. 6414–6419, Nov. 2012.

[42] S. M. Albrecht, A. P. Higginbotham, M. Madsen, F. Kuemmeth, T. S. Jespersen, J. Nygård, P. Krogstrup, and C. M. Marcus, "Exponential protection of zero modes in Majorana islands," *Nature*, vol. 531, no. 7593, pp. 206–209, Mar. 2016.

[43] S. Nadj-Perge, I. K. Drozdov, J. Li, H. Chen, S. Jeon, J. Seo, A. H. MacDonald, B. A. Bernevig, and A. Yazdani, "Observation of Majorana fermions in ferromagnetic atomic chains on a superconductor," *Science*, vol. 346, no. 6209, pp. 602–607, Oct. 2014.

[44] H. Zhang, Ö. Gül, S. Conesa-Boj, K. Zuo, V. Mourik, F. K. de Vries, J. van Veen, D. J. van Woerkom, M. Wimmer, D. Car, S. Plissard, E. P. A. M. Bakkers, M. Quintero-Pérez, S. Goswami, K. Watanabe, T. Taniguchi, and L. P. Kouwenhoven, "Ballistic Majorana nanowire devices," *arXiv.org*, Mar. 2016.

[45] S. Das Sarma, J. D. Sau, and T. D. Stanescu, "Splitting of the zero-bias conductance peak as smoking gun evidence for the existence of the Majorana mode in a superconductor-semiconductor nanowire," *Physical Review B*, vol. 86, no. 22, p. 220506, Dec. 2012.

[46] M. Tinkham, *Introduction to Superconductivity, 2nd ed.* Dover Publications, Jun. 2004.

[47] T. D. Stanescu, R. M. Lutchyn, and S. Das Sarma, "Dimensional crossover in spin-orbit-coupled semiconductor nanowires with induced superconducting pairing," *Physical Review B*, vol. 87, no. 9, p. 094518, Mar. 2013.

[48] T. D. Stanescu, S. Tewari, J. D. Sau, and S. Das Sarma, "To Close or Not to Close: The Fate of the Superconducting Gap Across the Topological Quantum Phase Transition in Majorana-Carrying Semiconductor Nanowires," *Physical Review Letters*, vol. 109, no. 26, p. 266402, Dec. 2012.

[49] D. Rainis, L. Trifunovic, J. Klinovaja, and D. Loss, "Towards a realistic transport modeling in a superconducting nanowire with Majorana fermions," *Physical Review B*, vol. 87, no. 2, p. 024515, Jan. 2013.

[50] D. Chevallier, P. Simon, and C. Bena, "From Andreev bound states to Majorana fermions in topological wires on superconducting substrates: A story of mutation," *Physical Review B*, vol. 88, no. 1, p. 165401, Oct. 2013.

[51] D. J. Griffiths, *Introduction to Quantum Mechanics*, 2nd ed. Upper Saddle River, NJ: Pearson, 2005.

[52] S. Coe, W.-K. Woo, M. Bawendi, and V. Bulović, "Electroluminescence from single monolayers of nanocrystals in molecular organic devices," *Nature*, vol. 420, no. 6917, pp. 800–803, Dec. 2002.

[53] Y. Shirasaki, G. J. Supran, M. G. Bawendi, and V. Bulović, "Emergence of colloidal quantum-dot light-emitting technologies," *Nature Photonics*, vol. 7, no. 1, pp. 13–23, Jan. 2013.

[54] Y. Yang, Y. Zheng, W. Cao, A. Titov, J. Hyvonen, J. R. Manders, J. Xue, P. H. Holloway, and L. Qian, "High-efficiency light-emitting devices based on quantum dots with tailored nanostructures," *Nature Photonics*, vol. 9, no. 4, pp. 259–266, Mar. 2015.

[55] X. Xu, B. Sun, P. R. Berman, D. G. Steel, A. S. Bracker, D. Gammon, and L. J. Sham, "Coherent Optical Spectroscopy of a Strongly Driven Quantum Dot," *Science*, vol. 317, no. 5, pp. 929–932, Aug. 2007.

[56] S. Chen, W. Li, J. Wu, Q. Jiang, M. Tang, S. Shutts, S. N. Elliott, A. Sobiesierski, A. J. Seeds, I. Ross, P. M. Smowton, and H. Liu, "Electrically pumped continuous-wave III–V quantum dot lasers on silicon," *Nature Photonics*, vol. 10, no. 5, pp. 307–311, Mar. 2016.

[57] C.-Y. Zhang, H.-C. Yeh, M. T. Kuroki, and T.-H. Wang, "Single-quantum-dot-based DNA nanosensor," *Nature Materials*, vol. 4, no. 11, pp. 826–831, Nov. 2005.

[58] Z. Yue, F. Lisdat, W. J. Parak, S. G. Hickey, L. Tu, N. Sabir, D. Dorfs, and N. C. Bigall, "Quantum-Dot-Based Photoelectrochemical Sensors for Chemical and Biological Detection," *ACS Applied Materials & Interfaces*, vol. 5, no. 8, pp. 2800–2814, Apr. 2013.

[59] H. Sun, L. Wu, W. Wei, and X. Qu, "Recent advances in graphene quantum dots for sensing," *Materials Today*, vol. 16, no. 11, pp. 433–442, Nov. 2013.

[60] K. W. Johnston, A. G. Pattantyus-Abraham, J. P. Clifford, S. H. Myrskog, D. D. MacNeil, L. Levina, and E. H. Sargent, "Schottky-quantum dot photovoltaics for efficient in-

frared power conversion," *Applied Physics Letters*, vol. 92, no. 1, p. 151115, Apr. 2008.

[61] E. H. Sargent, "Colloidal quantum dot solar cells," *Nature Photonics*, vol. 6, no. 3, pp. 133–135, Mar. 2012.

[62] D. K. Kim, Y. Lai, B. T. Diroll, C. B. Murray, and C. R. Kagan, "Flexible and low-voltage integrated circuits constructed from high-performance nanocrystal transistors." *Nature Communications*, vol. 3, pp. 1216–1216, Dec. 2011.

[63] F. Hetsch, N. Zhao, S. V. Kershaw, and A. L. Rogach, "Quantum dot field effect transistors," *Materials Today*, vol. 16, no. 9, pp. 312–325, Sep. 2013.

[64] D. Loss and D. P. Divincenzo, "Quantum computation with quantum dots," *Physical Review A*, vol. 57, no. 1, pp. 120–126, Jan. 1998.

[65] A. Imamog lu, D. D. Awschalom, G. Burkard, D. P. Divincenzo, D. Loss, M. Sherwin, and A. Small, "Quantum Information Processing Using Quantum Dot Spins and Cavity QED," *Physical Review Letters*, vol. 83, no. 2, pp. 4204–4207, Nov. 1999.

[66] R. C. Ashoori, "Electrons in artificial atoms," *Nature*, vol. 379, no. 6564, pp. 413–419, 1996.

[67] L. P. Kouwenhoven, N. C. Van der Vaart, A. T. Johnson, W. Kool, C. J. P. M. Harmans, J. G. Williamson, A. A. M. Staring, and C. T. Foxon, "Single electron charging effects in semiconductor quantum dots," *Zeitschrift für Physik B Condensed Matter*, vol. 85, no. 3, pp. 367–373, 1991.

[68] A. C. Johnson, J. R. Petta, C. M. Marcus, M. P. Hanson, and A. C. Gossard, "Singlet-triplet spin blockade and charge sensing in a few-electron double quantum dot," *Physical Review B*, vol. 72, no. 1, p. 165308, Oct. 2005.

[69] D. H. Cobden and J. Nygård, "Shell Filling in Closed Single-Wall Carbon Nanotube Quantum Dots," *Physical Review Letters*, vol. 89, no. 4, p. 046803, Jul. 2002.

[70] S. Csonka, L. Hofstetter, F. Freitag, S. Oberholzer, C. Schoenenberger, T. S. Jespersen, M. Aagesen, and J. Nygård, "Giant Fluctuations and Gate Control of the g-Factor in InAs Nanowire

Quantum Dots," *Nano letters*, vol. 8, no. 11, pp. 3932–3935, Nov. 2008.

[71] E. J. H. Lee, X. Jiang, R. Aguado, G. Katsaros, C. M. Lieber, and S. De Franceschi, "Zero-Bias Anomaly in a Nanowire Quantum Dot Coupled to Superconductors," *Physical Review Letters*, vol. 109, no. 1, p. 186802, Nov. 2012.

[72] A. P. Higginbotham, S. M. Albrecht, G. Kirsanskas, W. Chang, F. Kuemmeth, P. Krogstrup, T. S. Jespersen, J. Nygård, K. Flensberg, and C. M. Marcus, "Parity lifetime of bound states in a proximitized semiconductor nanowire," *Nature Physics*, vol. 11, no. 12, pp. 1017–1021, Sep. 2015.

[73] S. Tarucha, D. G. Austing, T. Honda, R. J. van der Hage, and L. P. Kouwenhoven, "Shell Filling and Spin Effects in a Few Electron Quantum Dot," *Physical Review Letters*, vol. 77, no. 17, p. 3613, Oct. 1996.

[74] T. Ihn, *Semiconductor Nanostructures*, ser. Quantum States and Electronic Transport. Oxford University Press, 2010.

[75] G. E. Blonder, M. Tinkham, and T. M. Klapwijk, "Transition from metallic to tunneling regimes in superconducting microconstrictions: Excess current, charge imbalance, and supercurrent conversion," *Physical Review B*, vol. 25, no. 7, p. 4515, 1982.

[76] W. Chang, "Superconducting proximity effect in InAs nanowires," Ph.D. dissertation, Harvard University, 2014.

[77] T. D. Stanescu, R. M. Lutchyn, and S. Das Sarma, "Majorana fermions in semiconductor nanowires," *Physical Review B*, vol. 84, no. 14, p. 144522, Oct. 2011.

[78] W. S. Cole, S. Das Sarma, and T. D. Stanescu, "Effects of large induced superconducting gap on semiconductor Majorana nanowires," *Physical Review B*, vol. 92, no. 17, p. 174511, Nov. 2015.

[79] W. Chang, S. M. Albrecht, T. S. Jespersen, F. Kuemmeth, P. Krogstrup, J. Nygård, and C. M. Marcus, "Hard gap in epitaxial semiconductor–superconductor nanowires," *Nature Nanotechnology*, vol. 10, no. 3, pp. 232–236, Mar. 2015.

[80] Y. V. Nazarov and Y. M. Blanter, *Quantum Transport: Introduction to Nanoscience*. Cambridge University Press, 2009.

[81] R. C. Ashoori, H. L. Stormer, J. S. Weiner, L. N. Pfeiffer, S. J. Pearton, K. W. Baldwin, and K. W. West, "Single-electron capacitance spectroscopy of discrete quantum levels," *Physical Review Letters*, vol. 68, no. 20, pp. 3088–3091, May 1992.

[82] R. Ashoori, H. Stormer, J. Weiner, L. Pfeiffer, K. Baldwin, and K. West, "N-electron ground state energies of a quantum dot in magnetic field," *Physical Review Letters*, vol. 71, no. 4, pp. 613–616, Jul. 1993.

[83] P. Hawrylak, "Single-electron capacitance spectroscopy of few-electron artificial atoms in a magnetic field: Theory and experiment," *Physical Review Letters*, vol. 71, no. 20, pp. 3347–3350, Nov. 1993.

[84] P. Krogstrup, N. L. B. Ziino, W. Chang, S. M. Albrecht, M. H. Madsen, E. Johnson, J. Nygård, C. M. Marcus, and T. S. Jespersen, "Epitaxy of semiconductor–superconductor nanowires," *Nature Materials*, vol. 14, no. 4, pp. 400–406, Apr. 2015.

[85] T. D. Stanescu, R. M. Lutchyn, and S. Das Sarma, "Soft superconducting gap in semiconductor-based Majorana nanowires," *Physical Review B*, vol. 90, no. 8, p. 085302, Aug. 2014.

[86] C. V. Kraus, P. Zoller, and M. A. Baranov, "Braiding of Atomic Majorana Fermions in Wire Networks and Implementation of the Deutsch-Jozsa Algorithm," *Physical Review Letters*, vol. 111, no. 20, p. 203001, Nov. 2013.

[87] B. van Heck, A. R. Akhmerov, F. Hassler, M. Burrello, and C. W. J. Beenakker, "Coulomb-assisted braiding of Majorana fermions in a Josephson junction array," *New Journal of Physics*, vol. 14, no. 3, p. 035019, Mar. 2012.

[88] D. B. Suyatin, C. Thelander, M. T. Björk, I. Maximov, and L. Samuelson, "Sulfur passivation for ohmic contact formation to InAs nanowires," *Nanotechnology*, vol. 18, no. 10, p. 105307, Mar. 2007.

[89] K. M. Lang, S. Nam, J. Aumentado, C. Urbina, and J. M. Martinis, "Banishing quasiparticles from Josephson-junction qubits: Why and how to do it," *IEEE Transactions on Appiled Superconductivity*, vol. 13, no. 2, pp. 989–993, Jun. 2003.

[90] J. Aumentado, M. W. Keller, J. M. Martinis, and M. H. Devoret, "Nonequilibrium Quasiparticles and 2 e Periodicity in Single-Cooper-Pair Transistors," *Physical Review Letters*, vol. 92, no. 6, p. 066802, Feb. 2004.

[91] J. M. Martinis, M. Ansmann, and J. Aumentado, "Energy Decay in Superconducting Josephson-Junction Qubits from Nonequilibrium Quasiparticle Excitations," *Physical Review Letters*, vol. 103, no. 9, p. 097002, Aug. 2009.

[92] J. T. Miller, A. Lazarus, B. Audoly, and P. M. Reis, "Shapes of a Suspended Curly Hair," *Physical Review Letters*, vol. 112, no. 6, p. 068103, Feb. 2014.

[93] O. P. Saira, A. Kemppinen, V. F. Maisi, and J. P. Pekola, "Vanishing quasiparticle density in a hybrid Al/Cu/Al single-electron transistor," *Physical Review B*, vol. 85, no. 1, p. 012504, Jan. 2012.

[94] I. M. Pop, K. Geerlings, G. Catelani, R. J. Schoelkopf, L. I. Glazman, and M. H. Devoret, "Coherent suppression of electromagnetic dissipation due to superconducting quasiparticles," *Nature*, vol. 508, no. 7496, pp. 369–372, Apr. 2014.

[95] M. Leijnse and K. Flensberg, "Scheme to measure Majorana fermion lifetimes using a quantum dot," *Physical Review B*, vol. 84, no. 14, p. 140501, Oct. 2011.

[96] M. Cheng, R. M. Lutchyn, and S. Das Sarma, "Topological protection of Majorana qubits," *Physical Review B*, vol. 85, no. 1, p. 165124, Apr. 2012.

[97] A. Ferguson, N. Court, F. Hudson, and R. Clark, "Microsecond Resolution of Quasiparticle Tunneling in the Single-Cooper-Pair Transistor," *Physical Review Letters*, vol. 97, no. 10, p. 106603, Sep. 2006.

[98] M. Zgirski, L. Bretheau, Q. Le Masne, H. Pothier, D. Esteve, and C. Urbina, "Evidence for Long-Lived Quasiparticles Trapped in Superconducting Point Contacts," *Physical Review Letters*, vol. 106, no. 25, p. 257003, Jun. 2011.

[99] L. Sun, L. DiCarlo, M. D. Reed, G. Catelani, L. S. Bishop, D. I. Schuster, B. R. Johnson, G. A. Yang, L. Frunzio, L. Glazman,

M. H. Devoret, and R. J. Schoelkopf, "Measurements of Quasiparticle Tunneling Dynamics in a Band-Gap-Engineered Transmon Qubit," *Physical Review Letters*, vol. 108, no. 23, p. 230509, Jun. 2012.

[100] D. Ristè, C. C. Bultink, M. J. Tiggelman, R. N. Schouten, K. W. Lehnert, and L. DiCarlo, "Millisecond charge-parity fluctuations and induced decoherence in a superconducting transmon qubit," *Nature Communications*, vol. 4, p. 1913, May 2013.

[101] V. F. Maisi, S. V. Lotkhov, A. Kemppinen, A. Heimes, J. T. Muhonen, and J. P. Pekola, "Excitation of Single Quasiparticles in a Small Superconducting Al Island Connected to Normal-Metal Leads by Tunnel Junctions," *Physical Review Letters*, vol. 111, no. 14, p. 147001, Oct. 2013.

[102] Y. J. Doh, "Tunable Supercurrent Through Semiconductor Nanowires," *Science*, vol. 309, no. 5732, pp. 272–275, Jul. 2005.

[103] L. Hofstetter, S. Csonka, J. Nygård, and C. Schönenberger, "Cooper pair splitter realized in a two-quantum-dot Y-junction," *Nature*, vol. 461, no. 7266, pp. 960–963, Oct. 2009.

[104] J. D. Pillet, C. H. L. Quay, P. Morfin, C. Bena, A. L. Yeyati, and P. Joyez, "Andreev bound states in supercurrent-carrying carbon nanotubes revealed," *Nature Physics*, vol. 6, no. 12, pp. 965–969, Nov. 2010.

[105] F. Giazotto, P. Spathis, S. Roddaro, S. Biswas, F. Taddei, M. Governale, and L. Sorba, "A Josephson quantum electron pump," *Nature Physics*, vol. 7, no. 11, pp. 857–861, Jul. 2011.

[106] J. D. Sau, R. M. Lutchyn, S. Tewari, and S. Das Sarma, "Generic New Platform for Topological Quantum Computation Using Semiconductor Heterostructures," *Physical Review Letters*, vol. 104, no. 4, p. 040502, Jan. 2010.

[107] C. Padurariu and Y. V. Nazarov, "Theoretical proposal for superconducting spin qubits," *Physical Review B*, vol. 81, no. 14, p. 144519, Apr. 2010.

[108] M. Leijnse and K. Flensberg, "Coupling Spin Qubits via Superconductors," *Physical Review Letters*, vol. 111, no. 6, p. 060501, Aug. 2013.

[109] R. S. Deacon, Y. Tanaka, A. Oiwa, R. Sakano, K. Yoshida, K. Shibata, K. Hirakawa, and S. Tarucha, "Tunneling spectroscopy of Andreev energy levels in a quantum dot coupled to a superconductor," *Physical Review Letters*, vol. 104, no. 7, p. 076805, 2010.

[110] E. J. H. Lee, X. Jiang, M. Houzet, R. Aguado, C. M. Lieber, and S. De Franceschi, "Spin-resolved Andreev levels and parity crossings in hybrid superconductor–semiconductor nanostructures," *Nature Nanotechnology*, vol. 9, no. 1, pp. 79–84, Dec. 2013.

[111] W. Chang, V. E. Manucharyan, T. S. Jespersen, J. Nygård, and C. M. Marcus, "Tunneling Spectroscopy of Quasiparticle Bound States in a Spinful Josephson Junction," *Physical Review Letters*, vol. 110, no. 21, p. 217005, May 2013.

[112] J. D. Sau and S. Das Sarma, "Realizing a robust practical Majorana chain in a quantum-dot-superconductor linear array," *Nature Communications*, vol. 3, p. 964, Jul. 2012.

[113] M. Leijnse and K. Flensberg, "Parity qubits and poor man's Majorana bound states in double quantum dots," *Physical Review B*, vol. 86, no. 13, p. 134528, Oct. 2012.

[114] I. C. Fulga, A. Haim, A. R. Akhmerov, and Y. Oreg, "Adaptive tuning of Majorana fermions in a quantum dot chain," *New Journal of Physics*, vol. 15, no. 4, p. 045020, Apr. 2013.

[115] L. Fu, "Electron Teleportation via Majorana Bound States in a Mesoscopic Superconductor," *Physical Review Letters*, vol. 104, no. 5, p. 056402, Feb. 2010.

[116] R. Hützen, A. Zazunov, B. Braunecker, A. L. Yeyati, and R. Egger, "Majorana Single-Charge Transistor," *Physical Review Letters*, vol. 109, no. 16, p. 166403, Oct. 2012.

[117] M. T. Tuominen, J. M. Hergenrother, T. S. Tighe, and M. Tinkham, "Experimental evidence for parity-based 2e periodicity in a superconducting single-electron tunneling transistor," *Physical Review Letters*, vol. 69, no. 13, p. 1997, 1992.

[118] P. Lafarge, P. Joyez, D. Esteve, C. Urbina, and M. H. Devoret, "Measurement of the even-odd free-energy difference of an isolated superconductor," *Physical Review Letters*, vol. 70, pp. 994–997, 1993.

[119] D. Averin and Y. Nazarov, "Single-electron charging of a superconducting island," *Physical Review Letters*, vol. 69, no. 13, pp. 1993–1996, Sep. 1992.

[120] F. Hekking, L. Glazman, K. Matveev, and R. Shekhter, "Coulomb blockade of two-electron tunneling," *Physical Review Letters*, vol. 70, no. 26, pp. 4138–4141, Jun. 1993.

[121] J. Hergenrother, M. Tuominen, and M. Tinkham, "Charge transport by Andreev reflection through a mesoscopic superconducting island," *Physical Review Letters*, vol. 72, no. 11, pp. 1742–1745, Mar. 1994.

[122] I. L. Aleiner, P. W. Brouwer, and L. I. Glazman, "Quantum effects in Coulomb blockade," *Physics Reports*, vol. 358, no. 5-6, pp. 309–440, Mar. 2002.

[123] M. Björk, A. Fuhrer, A. Hansen, M. Larsson, L. Fröberg, and L. Samuelson, "Tunable effective g factor in InAs nanowire quantum dots," *Physical Review B*, vol. 72, no. 20, p. 201307, Nov. 2005.

[124] K. A. Matveev, L. I. Glazman, and R. I. Shekhter, "Effects of Charge Parity in Tunneling Through a Superconducting Grain," *Modern Physics Letters B*, vol. 8, no. 1, pp. 1007–1026, 1994.

[125] D. G. Olivares, A. L. Yeyati, L. Bretheau, C. O. Girit, H. Pothier, and C. Urbina, "Dynamics of quasiparticle trapping in Andreev levels," *Physical Review B*, vol. 89, no. 1, p. 104504, Mar. 2014.

[126] A. Zazunov, A. Brunetti, A. L. Yeyati, and R. Egger, "Quasiparticle trapping, Andreev level population dynamics, and charge imbalance in superconducting weak links," *Physical Review B*, vol. 90, no. 10, p. 104508, Sep. 2014.

[127] L. P. Rokhinson, X. Liu, and J. K. Furdyna, "The fractional a.c. Josephson effect in a semiconductor-superconductor nanowire as a signature of Majorana particles," *Nature Physics*, vol. 8, no. 11, pp. 795–799, Nov. 2012.

[128] H. O. H. Churchill, V. Fatemi, K. Grove-Rasmussen, M. T. Deng, P. Caroff, H. Q. Xu, and C. M. Marcus, "Superconductor-nanowire devices from tunneling to the multichannel regime: Zero-bias oscillations and magnetoconductance crossover," *Physical Review B*, vol. 87, no. 24, p. 241401, Jun. 2013.

[129] T. M. Eiles, J. M. Martinis, and M. H. Devoret, "Even-odd asymmetry of a superconductor revealed by the Coulomb blockade of Andreev reflection," *Physical Review Letters*, vol. 70, no. 12, p. 1862, 1993.

[130] M. D. Schroer, K. D. Petersson personal communication, M. Jung, and J. R. Petta, "Field Tuning the g Factor in InAs Nanowire Double Quantum Dots," *Physical Review Letters*, vol. 107, no. 17, p. 176811, Oct. 2011.

[131] C. Fasth, A. Fuhrer, L. Samuelson, V. N. Golovach, and D. Loss, "Direct Measurement of the Spin-Orbit Interaction in a Two-Electron InAs Nanowire Quantum Dot," *Physical Review Letters*, vol. 98, no. 26, p. 266801, Jun. 2007.

[132] J. D. Sau, B. Swingle, and S. Tewari, "Proposal to probe quantum nonlocality of Majorana fermions in tunneling experiments," *Physical Review B*, vol. 92, no. 2, p. 020511, Jul. 2015.

[133] B. van Heck, R. M. Lutchyn, and L. I. Glazman, "Conductance of a proximitized nanowire in the Coulomb blockade regime," *Physical Review B*, vol. 93, no. 23, p. 235431, 2016.

[134] D. Sherman, J. S. Yodh, S. M. Albrecht, J. Nygård, P. Krogstrup, and C. M. Marcus, "Hybrid Double Quantum Dots: Normal, Superconducting, and Topological Regimes," *arXiv.org*, May 2016.

[135] P. J. De Visser, J. J. A. Baselmans, P. Diener, S. J. C. Yates, A. Endo, and T. M. Klapwijk, "Number Fluctuations of Sparse Quasiparticles in a Superconductor," *Physical Review Letters*, vol. 106, no. 1, p. 167004, Apr. 2011.

[136] D. J. van Woerkom, A. Geresdi, and L. P. Kouwenhoven, "One minute parity lifetime of a NbTiN Cooper-pair transistor," *Nature Physics*, vol. 11, no. 7, pp. 547–550, Jul. 2015.